MULTI POROSITY MODELS IN SHALES: FLOW BEHAVIOR AND IMPROVED RECOVERY

A Dissertation

by

MASOUD ALFI

Submitted to the Office of Graduate and Professional Studies of
Texas A&M University
in partial fulfillment of the requirements for the degree of

DOCTOR OF PHILOSOPHY

Chair of Committee,	John E. Killough
Co-Chair of Committee,	Maria A. Barrufet
Committee Members,	I. Yucel Akkutlu
	M. Sam Mannan
Head of Department,	Duane McVay

May 2018

Major Subject: Petroleum Engineering

ABSTRACT

The first part of this work proposes a partitioning scheme to divide porous media in shale into three different sub–media (porosity systems) with distinctive characteristics: inorganic matter and kerogen (in the shale matrix), along with fracture network (natural or hydraulic). This partitioning scheme is then deployed on a micro–scale model, which gives us the capability of analyzing the complex nature of mass transfer in shale. Current model can also handle various flow and storage mechanisms related with hydrocarbon production in shale such as molecule/wall interactions and slippage of the gas phase, multicomponent desorption, and capillarities. Although kerogen is considered to be a rich source of hydrocarbon, a relatively high capillary pressure and very low rock permeability hinder oil production in organic–rich shale. Such problems may be alleviated by employing appropriate production enhancement techniques, e.g. CO_2 EOR, compatible with the ultra–tight nature of such reservoirs.

In the second part of this dissertation, we propose a model to account for different pore sizes in shale and its influence on hydrocarbon distribution. Such a partitioning scheme provides a multiporosity–like approach where the fluid composition in different pore sizes varies due to size filtration and sieving effect. The proposed approach opens up new ways to interpret anomalous gas–oil ratios in shale. Recent advances in high precision analytical tools have revealed that pore size distribution in shale reservoirs spans a wide range. Molecules in pores with different sizes may exhibit significantly different thermodynamics behavior. Rock fluid interactions and space hindrance effects play an important role when pore sizes become close to species' molecular diameters. The tight porous media in such situations can act as a semi–permeable membrane that selectively filters molecules based on their

sizes. This effect can result in a composition difference between pores with large and small diameters in shale reservoirs (size filtration or sieving effect), with small pores mostly filled with smaller hydrocarbon molecules and large molecules residing in larger pores. To account for such a diverse behavior, this study proposes a pore partitioning approach, which divides shale media into two different porosity systems: large and small pores. Our thermodynamics calculations show that as pore diameter decreases, the concentration of larger hydrocarbon molecules in those pores decreases because of size filtration. The so–called sieving effect is believed to be responsible for the anomalous production behavior (lower–than–expected or constant gas–oil ratios for extended production periods). Considering the small pore size in shale and rock–fluid interactions, our current model was used to analyze the potential of different injection gases as improve recovery agents. Our results show that a higher pore wall affinity for CO_2 (compared to CH_4 and N_2) helps it reach deeper in small shale pores, making it a perfect fit to improve oil recovery from extremely tight media. Results show that our model provides a powerful tool to evaluate the complicated rock–fluid dynamics in liquid shales.

Inspired by the promising performance of CO_2 as an enhanced recovery agent, the multiple porosity model developed in this work is tested against simulating CO_2 EOR in shale. Core simulations show that light component striping, in addition to the regularly known swelling, is a dominant mechanism during CO_2 cyclic injection. Field–scale simulations have proven CO_2 EOR as a viable technique of improving recovery from shale. In addition to that, our results show that an effective fracturing design and a complex fracture network can increase reservoir exposure to CO_2 and boost up the ultimate process output.

DEDICATION

To my lovely grandmothers, whom I could not see one last time.

ACKNOWLEDGMENTS

First and foremost, I would like to express my sincere gratitude to my advisers Dr. Maria Barrufet and Dr. John Killough for the continuous support of my doctorate study and related research, for their patience, motivation, challenge, and immense knowledge. Their guidance helped me in all the time of research and writing of this dissertation. I could not have imagined having a better help and mentors for my PhD study.

Besides, I would like to thank Dr. I. Yucel Akkutlu and Dr. M. Sam Mannan for serving in my committee and providing me with their insightful comments.

My warmest thanks go to my friends and colleagues who helped me during my projects: Dr. Bicheng Yan, Dr. Seyyed A. Hosseini, Dr. Mohammad Lotfollahi, Yang Cao, Cheng An, and Zhi Chai.

Doing research has its ups and downs but something that kept me motivated and going was Sundays and Fantasy Football. I would like to thank Carson Wentz for his pinpoint accuracy on passes, DeAndre Hopkins for his spectacular catches, and Leonard Fournette and LeSean McCoy for their explosive runs. An honorary mention goes to Baltimore Ravens defense for their sacks, interceptions, and defensive touchdowns.

Last but not the least, I would like to thank my family: my parents, my brother, my sister–in–law, and my lovely sister Mahshid for supporting me spiritually throughout my PhD study and my life in general.

CONTRIBUTORS AND FUNDING SOURCES

This work is supervised by a dissertation committee consisting of Dr. John E. Killough (chair) of the Department of Petroleum Engineering, Dr. Maria A. Barrufet (co-chair) of the Department of Petroleum Engineering, Dr. I. Yucel Akkutlu of the Department of Petroleum Engineering, and Dr. M. Sam Mannan of the Department of Chemical Engineering at Texas A&M University.

All work for the dissertation was completed by the student, in collaboration with Dr. Bicheng Yan.

Parts of this project is funded by the Crisman Institute for Petroleum Research and the Berg–Hughes Center for Petroleum and Sedimentary Systems at Texas A&M University. Steve A. Holditch serves as the associate director of the Crisman Institute for Petroleum Research and Mukul R. Bhatia is the director of the Berg–Hughes Center for Petroleum and Sedimentary Systems. The author thanks Landmark Software and Services for providing the academic license for the Nexus Desktop suit.

NOMENCLATURE

The units are all in SI.

a_{p}	Peng–Robinson a modified for pore effects, Pa $\mathrm{m}^6/\mathrm{mol}^2$
b	Slip coefficient
b_{p}	Peng–Robinson b modified for pore effects, $\mathrm{m}^3/\mathrm{mol}$
$\hat{f}$	Fogacity, Pa
F_{pr}	Geometric function for the confined fluid
g	Earth gravity coefficient, 9.81 $\mathrm{m/s}^2$
K	Intrinsic permeability, m^2
K_{n}	Knudsen number
K_{rA}	Aqueous phase relative permeability
K_{rG}	Gas phase relative permeability
K_{rO}	Oil phase relative permeability
$K_{\mathrm{r,inrwet}}$	Intermediate wetting phase relative permeability
$K_{\mathrm{r,nonwet}}$	Non–wetting phase relative permeability
$K_{\mathrm{r,wet}}$	Wetting phase relative permeability
M	Gas molecular weight, kg/kmole
N_{av}	Avogadro number, 1/mol
N_{krg}	Total number of kerogen grids
N_{total}	Total number of grids
n_{w}	Wetting phase drainage/imbibition exponent
n_{nwd}	Non–wetting phase drainage exponent

n_{nwi}	Non–wetting phase imbibition exponent
P	Pressure, Pa
P_{A}	Aqueous phase pressure, Pa
P_{G}	Gas phase pressure, Pa
P_{L}	Pressure in large pores, Pa
P_{O}	Oil phase pressure, Pa
P_{S}	Pressure in small pores, Pa
P_i	Partial pressure of component i in the gas phase, Pa
r	Pore radius, m
R	Universal gas constant, 8314.46 J/kmol/K
S_{inrwet}	Intermediate wetting phase saturation
S_{inrwr}	Intermediate wetting phase residual saturation
S_{nonwet}	Non–wetting phase saturation
S_{nwt}	Non–wetting phase trapped saturation
S_{nwc}	Non–wetting phase critical saturation
S_{wc}	Wetting phase critical saturation
S_{wcw}	Wetting phase critical saturation with respect to the wetting phase
S_{wcnw}	Wetting phase critical saturation with respect to the non–wetting phase
S_{wet}	Wetting phase saturation
S_{wetr}	Wetting phase residual saturation
S_{wi}	Initial wetting phase saturation
T	Temperature, K
TOC	Total organic carbon, wt%

v	Fluid velocity, m/s –or– molar volume, m^3/mol
v_{G}	Gas phase velocity, m/s
V_{g}	Adsorption capacity, m^3/kg
$V_{\mathrm{L}i}$	Langmuir volume of component i, m^3/kg
X_{β}^{v}	Mass fraction of component v in phase β
z	Elevation, m –or– gas compressibility factor
δ_{p}	Energy parameter for confined EOS calculations
ϵ_{p}	Energy parameter for confined EOS calculations, J
λ	Mean free path, m
λ_{P}	Pore size distribution factor
μ	Viscosity, Pa.s
ω	Relative permeability normalization factor
ϕ	Porosity
$\hat{\phi}_i$	Fogacity coefficient of component i
ϕ_{inorg}	Inorganic matter porosity
ϕ_{krg}	Kerogen porosity
ρ	Fluid or rock density, kg/m^3
ρ_{inorg}	Inorganic matter density, kg/m^3
ρ_{krg}	Kerogen density, kg/m^3
σ_i	Molecular diameter of component i
τ	Tortuosity
θ	Geometric function for the confined fluid

TABLE OF CONTENTS

Page

ABSTRACT ii

DEDICATION iv

ACKNOWLEDGMENTS v

CONTRIBUTORS AND FUNDING SOURCES vi

NOMENCLATURE vii

TABLE OF CONTENTS x

LIST OF FIGURES xii

LIST OF TABLES xix

1. INTRODUCTION 1

    1.1 Problem statement 1
    1.2 Eagle Ford play 1
    1.3 Included in this dissertation 3

2. MICRO–SCALE MODELS 5

    2.1 Introduction 5
    2.2 Review of the current multiple porosity approach 7
    2.3 Fundamental equations of flow and storage 12
        2.3.1 Flow mechanisms and formulation 12
        2.3.2 Multi-component adsorption 19
        2.3.3 Mass balance equation 20
    2.4 Model specifications and system properties 22
    2.5 Results and discussion 30
        2.5.1 Shale matrix depletion–different mechanisms 30
        2.5.2 Alteration of producing gas–oil ratio in the near fracture regions 42
        2.5.3 Effect of TOC on hydrocarbon production 45
    2.6 Conclusions 48

3. SIEVING EFFECT AND SIZE FILTRATION 50

3.1 Introduction . . . 50
3.2 Pore size distribution . . . 52
3.3 What is size filtration or sieving? . . . 55
3.4 Thermodynamics of sieving . . . 58
3.5 Single– and multi–component sieving . . . 66
3.6 Impact of sieving on production behavior . . . 73
3.6.1 Multiple porosity model . . . 73
3.6.2 Base case model . . . 76
3.6.3 Sensitivity analysis . . . 82
3.6.4 Eagle Ford case study . . . 86
3.6.4.1 Reservoir dimensions and well completion . . . 86
3.6.4.2 Fluid properties . . . 87
3.6.4.3 Microseismic events . . . 91
3.6.4.4 Numerical model . . . 94
3.7 Using the fluid–rock affinity in our favor . . . 99
3.8 Conclusion . . . 105

4. MULTIPLE POROSITY AND IMPROVE RECOVERY FROM SHALE . 106

4.1 Introduction . . . 106
4.2 Core experiments simulation . . . 107
4.2.1 Numerical model dimensions . . . 108
4.2.2 Production mechanism . . . 111
4.3 Full field simulation . . . 116
4.4 Conclusions . . . 120

5. SUMMARY AND CONCLUSIONS . . . 121

REFERENCES . . . 123

APPENDIX A. APPARENT PERMEABILITY CALCULATION . . . 141

APPENDIX B. MULTI-COMPONENT OIL AND GAS DESORPTION CALCULATION . . . 146

APPENDIX C. EAGLE FORD MULTIPLE POROSITY MODEL . . . 151

LIST OF FIGURES

FIGURE Page

1.1 Eagle Ford shale production region subdivisions (reprinted from Tian [3]). 2

2.1 Cross sections of a single shale matrix show kerogen grid blocks (red squares) are randomly distributed in the inorganic frame (yellow). Kerogen grid blocks can sit directly adjacent to other kerogen, inorganic, or fracture grids with no limitation. This shale matrix is surrounded by fracture grid blocks (not shown in the picture). Shown in the right side, each grid block system (kerogen and inorganic) has its own porosity, permeability, density, wettability, etc. 9

2.2 Schematic of the current model and the way different porosity systems are connected to each other. According to the figure, kerogen or inorganic grids can be connected to each other with no limitations and the grids at the faces of the matrix are connected to the fracture network. Hydrocarbon production and water imbibition happens only though fracture grids. 12

2.3 Classification of different flow regimes and corresponding flow equations based on dimensionless Knudsen number (K_{n}) (reprinted after Schaaf and Chambre [26], Roy et al. [27], and Mahulikar et al. [28]) shows that continuum flow does not hold true when pore diameter becomes comparable to that of the molecule mean free path. 14

2.4 Different capillary pressure curves are used for the inorganic and kerogen grid blocks in this model where the capillary pressure value in inorganic matter (blue solid line) is assumed to be larger than that of kerogen (red dashed line). 24

2.5 Two–phase relative permeability curves used to calculate three–phase relative permeability in shale. While both imbibition and drainage processes follow the same wetting phase relative permeability curve, the non–wetting phase has two different curves for drainage and imbibition relative permeabilities. 26

2.6 As production starts in the water imbibition scenario, pressure decreases in both kerogen and inorganic due to the hydrocarbon depletion process. At late production times, pressure in the inorganic matter increases because of water imbibition. 31

2.7 Water saturation in the inorganic matter increases (water imbibition scenario) as a result of water imbibition into the matrix later in the course of simulation. Fluid movement in kerogen is somehow limited to two–phase gas and oil flow and water phase saturation stays at low values without considerable changes. 32

2.8 After production starts in the water imbibition scenario, oil saturation in inorganic decreases and water will replace oil in inorganic. Mass transfer in kerogen is limited to two-phase oil and gas flow where oil saturation stays almost constant in kerogen. 33

2.9 Gas saturation in the inorganic decreases as production continues and water from fracture replaces the gas phase there. In kerogen, however, gas saturation does not change substantially. 34

2.10 Although kerogen is a rich source of liquid hydrocarbons, very low permeability in shale hinders oil production from such reservoirs. Gas recovery, on the other hand, is higher due to its improved permeability (slip effect) and lower viscosity. Water imbibition from fracture into the inorganic mater helps to produce more hydrocarbon. 35

2.11 This figure shows the pressure distribution in the matrix with time. As evident, pressure starts decreasing as production starts from the fracture network. The red blocks in the first picture show kerogen and the rest are inorganic grid blocks. 37

2.12 Water saturation distribution in the shale matrix is depicted at different times in this picture (water imbibition scenario). Despite pressure depletion, water imbibition into the system starts well after hydrocarbon production has begun (in the first two plots red grid blocks represent the kerogen and the remaining blocks are inorganic). . . . 38

2.13 Matrix pressure (kerogen and inorganic matter) decreases steadily with time as we continue producing from the shale matrix for the cases where no water is in the fracture. The main drive mechanism in this scenario is oil and gas expansion. 39

2.14 Water saturation in the inorganic and kerogen stays constant for cases where fracture is filled with hydrocarbon. 40

2.15 Oil saturation in kerogen stays almost constant, while its saturation in inorganic decreases and gas will replace oil in that media. 41

2.16 With further pressure depletion, gas comes out of solution and expands in the inorganic to compensate for oil production. 42

2.17 Gas recovery is slightly lower when no water imbibes into the matrix (compare it to Figure 2.10). Oil recovery is very low in such tight reservoirs. 43

2.18 Pressure and gas saturation maps in the shale matrix (dimensionless time = 5×10^4) show that gas saturation increases in the vicinity of fracture where pressure decreases considerably. Localized large gas–to–oil mobility ratio can considerably impact oil production in liquid–rich shale. 43

2.19 Producing gas–oil ratio increases as pressure in the near fracture region drops (starting at dimensionless time of 10^3) and gas comes out of solution. 44

2.20 As production continues, pressure decreases in the matrix and dissolved gas starts coming out of solution. This excessive gas is responsible for the increased producing gas–oil ratio in the matrix. 45

2.21 Average pressure in shale matrix follows a similar trend for higher and lower TOC values. 46

2.22 Higher TOC values increase total gas production from the shale matrix. 47

2.23 Total oil production from the shale matrix does not increase with higher TOC values due to the restricted oil flow in low permeability shale. 48

3.1 Pore size distribution in two different shale samples show that a broad range of pore sizes can be found in shale reservoirs. The sample from Muskwa and Besa Rive formations have pores with diameters as low as 1 nm, up to 100 µm which is five orders of magnitude larger (reprinted from Chalmers et al. [63] and Ross and Bustin [67]). 54

3.2 Schematic of the proposed size filtration effect in which larger hydrocarbon molecules are excluded from small pores. As a result, the fluid composition in the larger pores exhibits a heavier nature, compared to that of smaller pores. 56

3.3 Hydrocarbon distribution in large and small pores for binary mixtures of heptane–decane and heptane–tetradecane. The dashed line shows situations where no sieving takes place and the composition of small and large pores are the same. 5A molecular sieve (pore opening is equal to 0.5 nm) was used for these experiments (reprinted from Sundstorm and Krautz [70]). The results show a clear filtration effect for larger–size molecules. 58

3.4 Large and small pores are considered to be in thermodynamic equilibrium, which means equality of fugacities of individual components through the system. Pressure and composition of the large pores are given in our calculations and those of the small pores will be calculated accordingly. $\hat{f}_i$ in this picture represents the fugacity of component i. 61

3.5 Density of hexane and octane in small pores versus hydrocarbon concentration in large pores from the experimental data (reprinted from Gupta et al. [96]) are used to calibrate the equation of state model. Adsorption experiments were performed for each hydrocarbon individually (no mixture) and benzene was used to dilute the samples and achieve different mole fractions in the large pores. The model–predicted density values show a good agreement with the experimental data. Data reported at 42 °C (107 °F) and atmospheric pressure. . . 65

3.6 Comparison of the molar density of octane in small pores with various diameters. Pores with smaller diameters will impose a more pronounced steric hindrance, preventing the hydrocarbon molecules to enter small pores and resulting in a lower molar density for the same given bulk phase pressure. The dashed line shows the molar density of bulk octane in large pores. 3102K and 0.46 are used for $\frac{\epsilon_{\mathrm{p},i}}{\mathrm{k}}$ and $\frac{\delta_{\mathrm{p},i}}{\sigma_i}$ respectively (see Table 3.1). 67

3.7 Molar density of octane (at 6000 psi and 212°F) in small pores for different pore sizes at various fluid–wall affinities. The $\frac{\epsilon_{\mathrm{p},i}}{\mathrm{k}}$ values for low, moderate, and high rock–fluid affinities are 1200, 3102, and 5300 K, respectively. 69

3.8 The composition distribution of binary mixtures of C_6–C_8 and C_6–C_{12} in a 5 nm wide pore shows larger species (C_8 and C_{12}) will face a steric hindrance when competing with a smaller hydrocarbon (C_6) to enter small pores. The larger the hydrocarbon molecules, the more pronounced the size sieving effect is. 71

3.9 Hydrocarbon distribution in small pores shows an apparent sieving effect due to size hindrance and pore–fluid interactions. Heavier hydrocarbons exhibit a lower mole fraction in pores of smaller diameters. 72

3.10 The triple permeability model used in this study to account for sieving and size filtration effects in liquid rich shales. 75

3.11 Reservoir dimensions along with the fracture distribution for the synthetic reservoir model. The blue blocks show the hydraulic fracture plane, the green region shows the micro fracture distribution (blue and green blocks constitute the stimulated reservoir volume) and the red blocks show the unfractured reservoir volume. 77

3.12 (a,b) Gas saturation maps in the small pores and large pores (5 years after production) show a higher gas saturation in small pores due to a lighter composition in such pores, (c) gas saturation for the no–sieving case where the composition is considered to be uniformly distributed in the reservoir. 80

3.13 Producing gas–oil ratio for the cases with and without sieving and comparison to the global fluid solution gas–oil ratio shows that sieving can alter the production stream (compared to the no–sieving fluid) towards producing more of the heavy components. Gas–oil ratio decreases when sieving happens in the reservoir. 81

3.14 Producing well stream shows that sieving causes the produced fluid to be heavier than the in–situ reservoir fluid. 83

3.15 Producing gas–oil ratio in the reservoir decreases by increasing the permeability contrast ($\frac{K_L}{K_S}$ shows the ratio of permeability in large pores to that of small pores). 84

3.16 Producing gas oil ratio in the reservoir decreases as sieving becomes more pronounced. 85

3.17 Constant composition expansion experiments on the Eagle Ford sample of interest. 89

3.18 Differential liberation experiments on the Eagle Ford sample of interest. 90

3.19 Map view of the microseismic events from the well of interest. 92

3.20 Event count by the stage for the modeled well in our simulation case. 93

3.21 In the workflow of generating the numerical model, seismic events are spatially bounded and overlaid on a frame of structured gridblocks and fracture gridblocks are activated in cells with one or more seismic events located inside. 94

3.22 Fracture network model generated by the microseismic data. Using the microseismic data to model the stimulated reservoir volume has provided a realistic picture of the induced fracture network. 95

3.23 Water–oil and gas–oil two–phase relative permeabilities are used in our model to model the three phase relative permeability. 96

3.24 Oil production rates from that of field data and simulation closely resemble, increasing our confidence on the reliability of the proposed sieving model. 97

3.25 Similar to the oil rates, our model closely matches the gas production rates from the Eagle Ford case. 98

3.26 Despite oil and gas production, the GOR match of the field and simulation data looks to be poor. Parts of it is attributed to the discrepancy in reading the data as GOR's show a considerable fluctuation. 99

3.27 Pressure and gas saturation distribution in small and large pores (middle layer of the reservoir) 2.5 years after production starts. 100

3.28 Comparison of the density of gases in small pores from the experimental data (reprinted from Dreisbach [106]) and the equation of state model. Experiments are performed at 298K (77 °F). 102

3.29 This graph shows the composition distribution of the injected gas into the shale, along with the composition in the pores. CO_2 exhibits a better capability of entering small pores and extracting the oil trapped in such a tight media. 104

4.1 Schematic of the numerical model for the multiple–porosity core–scale CO_2 EOR simulation case. 108

4.2 Porosity and permeability histogram of the small pores for the core experiment simulation. 110

4.3 Porosity distribution in small pores of the top layer of the core simulation. 110

4.4 Molar–based hydrocarbon recovery shows CO_2 injection can double the initial recovery within the 5th cycle. Such a high recovery has been also reported in some experiments but it is hardly achievable in field scales. Despite core experiments, CO_2's access to oil in field cases is just limited to the fracture network. 112

4.5 Oil saturation at the end of each cycle. Blue and red are the ends of the color bar, representing 0 and 1 for oil saturation, respectively. . . 113

4.6 CO_2 mole fraction in the oil phase at the end of the 15th cycle shows CO_2 concentrations as high as 50% in the oil phase, meaning that CO_2 takes hydrocarbons out of the oil phase and substitutes them. 114

4.7 The production stream shows that after initial recovery (cycle 0), the produced hydrocarbon becomes very light and it slowly becomes heavier at the later cycles. 114

4.8 Lighter components are extracted by CO_2 sooner than the heavier species. 115

4.9 The blue line in this graph shows the total hydrocarbon recovery (molar basis) and the red dashed line shows oil recovery. According to the graph, although CO_2 increases the ultimate recovery, it also strips some of oil components out of the oil phase and produces them as separator gas. 116

4.10 As we can see from the graph, CO_2 injection increases ultimate recovery by a factor of 50% after 72 months. 117

4.11 CO_2 concentration map after injection shows CO_2 barely goes far into the reservoir rock and will be mostly concentrated in the vicinity of the fracture network. 118

4.12 Although ultimate recovery increases for longer soaking periods, the increment is not that significant. 119

LIST OF TABLES

TABLE Page

2.1 Micro–scale model description and media/fluid properties 29

3.1 The regressed $\frac{\epsilon_{p,i}}{k}$ and $\frac{\delta_{p,i}}{\sigma_i}$ parameters (for C_6 and C_8 on zeolite molecular sieve) that generate the best match with the experimental data. . 65

3.2 The following experimental and extrapolated $\frac{\epsilon_{p,i}}{k}$ and $\frac{\delta_{p,i}}{\sigma_i}$ parameters for different hydrocarbon species were used in the current paper. . . . 70

3.3 In–situ reservoir fluid composition for cases with and without sieving. 79

3.4 In–situ reservoir fluid composition for low sieving and moderate sieving cases. 85

3.5 Treatment well data 87

3.6 Molar composition of the Eagle Ford fluid sample with hydrocarbons up to C_{30}. 88

3.7 Rock/fluid interaction parameters to match CH_4, N_2, and CO_2 adsorption data on activated carbon. 103

1. INTRODUCTION

1.1 Problem statement

Associated with particles of micro meter size, the abundant contents of shale are clays and organics. Mineralogy wise, it is suggested that shales are dominated by quartz and clays, however, other minerals can be found depending on the depositional environments. Drilling and completion activities indicate that only a small portion of shale acreage is "core." Even in those core areas, rock qualities are seen to be quite diverse. Such a heterogeneity occurs at all scales: field wide, seismic, wellbore, cores, and even small scale high resolution microscopy. It is also manifested in natural–fracture network, matrix, petrophysical properties, and hydrocarbon volumes. Heterogeneity presents challenges in its assessment and quantification, drilling and completion strategies, production scenarios, and reservoir simulation. These challenges are exacerbated by the need to reduce costs, reluctance to retrieve core, and the limited logging executed in horizontal boreholes. In this dissertation, we will present a multiple porosity model, in an effort to address the challenges related to numerical simulation of fluid flow in highly heterogeneous shale reservoirs.

1.2 Eagle Ford play

Eagle Ford play is located in South Texas and produces from depths as shallow as 2500 ft and as deep as 14000 ft [1]. This shale play is known as the source rock for the Austin Chalk and the East Texas Field [1]. The geological era of Eagle Ford back dates to upper Cretaceous. Edman and Janet [2] divided the formation into Upper and Lower Eagle Ford. The upper Eagle Ford has a higher carbonate content while the lower Eagle Ford is a richer source of organic matter, with the majority being type II kerogen [1, 2]. According to Tian [3], Eagle Ford fluid evolves from oil, to gas

condensate, and dry gas. Oil gravity increases from 43 to 60 API when going from northwest to southeast with gas specific gravities of 0.6 to 0.85 and pressure gradients of 0.68 to 0.85 psi/ft respectively. Tian [3] divided Eagle Ford into five production zones based on production and regional trends of depth, thickness, average TOC, gamma ray, and bulk density. Figure 1.1 shows those production regions. Regions 1 and 2 are the most productive oil and gas regions, and coincide with the regional, strike–elongate trends of geological parameters, recommending that these parameters significantly impact Eagle Ford production [3]. In this study, an example from Eagle Ford is used to deploy our proposed multiple porosity model on real field data.

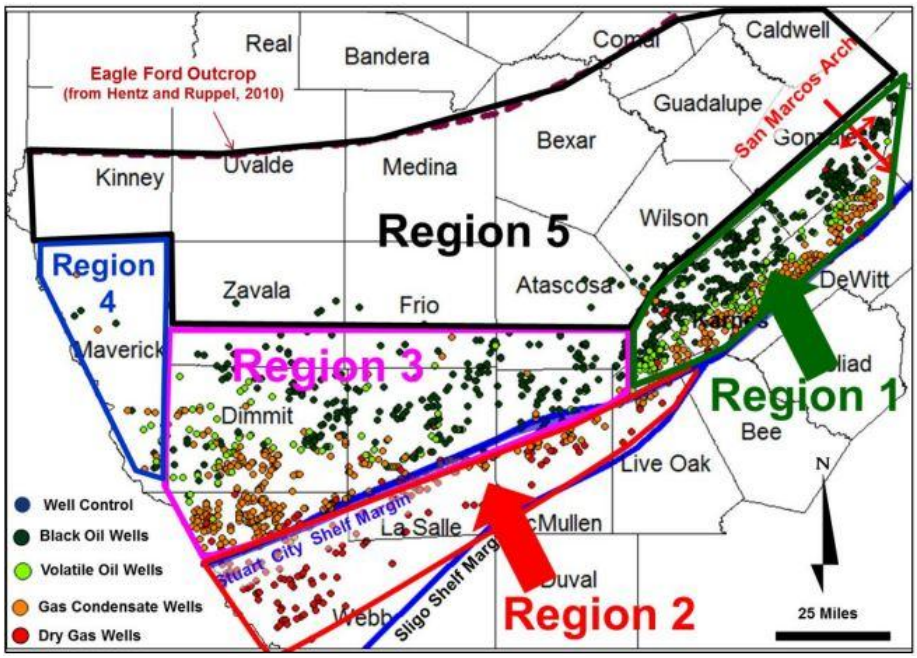

Figure 1.1: Eagle Ford shale production region subdivisions (reprinted from Tian [3]).

1.3 Included in this dissertation

This study revolves around a unique idea of using multiple porosity methods to simulate fluid flow in shale reservoirs. The whole subject is broken into three chapters that discuss different aspects of multiple porosity modeling:

- **micro–scale models**: in this chapter, we have presented a micro–scale model to analyze the dynamics of multi phase flow in shale while dividing the matrix into two sub–media of inorganic and kerogen. The presented model evaluates different production mechanisms (e.g. water imbibition and hydrocarbon expansion) while taking into account phenomenon such as diffusion and desorption.

- **sieving effect and size filtration**: inspired by the heterogeneous nature of the shale and the fact that pore sizes in shale span a wide range, we have proposed a model to account for what is called "size filtration or sieving effect." Our model takes into account the rock–fluid interactions in small pores in which, the large molecules are not able to enter small pores due to steric restriction effects. We then used a commercial simulator (Nexus from Halliburton) to see how such a behavior affects the production behavior from the reservoir.

- **multiple porosity and improve recovery from shale**: this dissertation concludes by a discussion on improve recovery methods in shale. Our multiple porosity model is tested against cyclic CO_2 injection to enhance oil recovery from low permeability reservoirs. A core–scale simulation is performed to understand the dominant mechanism during CO_2 injection. That is followed by a full field simulation to see how the model performs and what are the effective

factors in CO_2 injection design.

2. MICRO–SCALE MODELS[†]

2.1 Introduction

Recently, considerable advances in shale related operations have introduced these resources as a secure and stable source to meet the growing demand for energy. A significant portion of these advances is attributed to the development of brilliant new technologies that make possible the discovery and production of new hydrocarbon resources. What makes shale reservoirs somehow distinctive, or better said challenging, compared to conventional hydrocarbon resources, is complicated geological and petrophysical properties of these reservoirs. Shale reservoirs are usually known by their extremely low permeability. This low permeability, by itself, has created a great deal of difficulties when working on shale. In addition to that, new explorations of liquid–rich shale plays with complicated multiphase flow physics have made the subject even more exciting. Having a solid understanding of the microstructural controls on permeability, porosity systems, hydraulic properties, wettability, etc. will certainly expand our capability to utilize shale resources more efficiently. Nowadays, high precision analytical tools are employed to examine the microstructure of shale formations. Curtis et al. [4, 5] investigated samples from different shale plays and reported significant variations in mineral content, micro texture, fabric, pore type, etc. depending on age, mineralogy, and kerogen type and content in those samples. Despite distinctive characteristics of different shale samples, there has been a certain common point observed specifically among hydrocarbon bearing organic shales and that was the presence of kerogen (organic matter with a high carbon content

[†]Reprinted with permission from "How to Improve our Understanding of Gas and Oil Production Mechanisms in Liquid–rich Shale" by M. Alfi, B. Yan, Y. Cao, C. An, Y. Wang, J. He, J. Killough. Paper presented at SPE Annual Technical Conference and Exhibition (ATCE2014). Copyright 2014 by SPE. Further reproduction prohibited without permission.

present in sedimentary rocks), scattered in an inorganic frame of minerals like quartz, clay, carbonate, and pyrite. Presence of kerogen in shale increases porosity, changes grain density, provides hydrocarbon source, imparts anisotropy, alters wettability, and introduces different flow and storage mechanisms [6, 7, 8]. Additionally, several studies show that kerogen pores in a continuous organic framework can form an effective pore system to dominate flow pathway [5, 7, 9]. All these evidences demonstrate the importance of considering a designated porosity system to model flow behavior in kerogen. To better characterize this subtle pore system Yan et al. [10, 11] and Alfi et al. [12, 13] proposed a micro–scale model with a shale subdivision scheme. SEM studies show porosity in shale is found in kerogen, between grains, in pyrite framboid, fossils, within minerals, and in the form of microcracks [6]. Loucks et al. [14, 15] have classified pores in mudrocks into three major matrix–related types of interparticle and intraparticle pores, found between or within particles, in mineral matrix and intraparticle pores located in kerogen. Pores in kerogen can have irregular shapes with an elliptical cross section ranging from 5 to 750 nm. Relatively similar pore classification schemes in mudstone and shale are presented based on mineralogy, connectivity, and texture [16, 17]. Understanding the abundance, distribution, and spatial interrelationships of each pore type is important because each type may contribute differently to permeability, leading to a need to understand the distribution of pores and establish their connectivity. In this chapter, we introduce a micro–scale model that divides shale systems into different sub–media and account for the variability in mineralogy, pore size and structure, and flow behavior of each sub–medium. The current model is furnished with the capability of handling three phase oil, gas, and water flow in liquid–rich shale considering the appropriate multiphase flow related functions. In addition to that, multicomponent hydrocarbon adsorption and molecule/wall interactions of the gas phase are incorporated into the

model. Simulations in this chapter is performed by an in–house simulator developed by the author. The source code is in Fortran 90.

2.2 Review of the current multiple porosity approach

Inspired by what has been mentioned so far, we propose a state-of-the-art approach to model multiphase flow of hydrocarbons in unconventional liquid–rich shale reservoirs. Understanding storage and flow mechanisms from such reservoirs, as in the Eagle Ford, Woodford, and Bakken, is crucial in the overall effort to increase the ultimate hydrocarbon production. Based on geological evidence from high resolution analytical tools, three different porosity/permeability systems with distinctive hydraulic, wettability, transport, and storage characteristics, have been recognized in shale reservoirs, named as kerogen, inorganic matter, and natural or hydraulic fractures. In this work, we have developed a robust model to investigate three–phase (water, liquid and gas phase hydrocarbon) flow in ultra–low permeability liquid–rich shale reservoirs. This is achieved by an innovative technique of subdividing shale into three porosity/permeability systems and using appropriate flow mechanisms (convective and/or diffusive) in each sub–medium. Geological images show that the distribution of kerogen within inorganic minerals and the size of natural fractures are all at the micrometer scale, thus it is reasonable to control the simulation model within micrometer size if subdivision of shale matrix is required. One advantage of the current micrometer scale model is that with the diverse distribution of different porosity systems in the model, different physics can be assumed in various porosity types we have considered in shale (inorganic matter, kerogen, or fracture). By noticing the fact that each of these media can respond differently in similar situations, our model captures the complex dynamics in shale. The current multiple permeability model is built upon a unique tool for simulating general multiple permeability

systems in which several porosity/permeability systems may be tied to each other through arbitrary transfer functions and connectivities. Kerogen grid blocks in our model are mainly made of carbon–rich material, which is the main source of hydrocarbon generation during diagenesis. Looking at the shale structure, one can see that kerogen units are dispersed in an inorganic frame [7]. This is achieved in our model through a rigorous Monte Carlo algorithm, where kerogen grids are randomly distributed in the shale matrix [18, 19]. Abundance of kerogen grids is calculated using the Total Organic Carbon (TOC) value, kerogen and inorganic matter density and porosity:

$$\frac{N_{\text{krg}}}{N_{\text{total}}} = \frac{\text{TOC} \times \rho_{\text{inorg}}(1-\phi_{\text{inorg}})}{\rho_{\text{krg}}(1-\phi_{\text{krg}}) + \text{TOC} \times (\rho_{\text{inorg}}(1-\phi_{\text{inorg}}) - \rho_{\text{krg}}(1-\phi_{\text{krg}}))} \tag{2.1}$$

where N_{krg} and N_{total} are the number of kerogen and total grid blocks respectively, ρ_{inorg} and ϕ_{inorg} represent the inorganic matter density and porosity, ρ_{krg} and ϕ_{krg} specify the density and porosity of kerogen (all in consistent units). Total Organic Carbon (TOC) is a measure of the current quantity of kerogen or organic richness and is defined as the mass percent of organic matter in the shale matrix. The current model considers no limits in connectivity of different porosity systems (inorganic, kerogen, and fracture) where kerogen grid blocks can be neighbor to other kerogen and inorganic grids, or directly sit adjacent to the fracture grids (Figure 2.1 shows kerogen blocks dispersed in the inorganic frame).

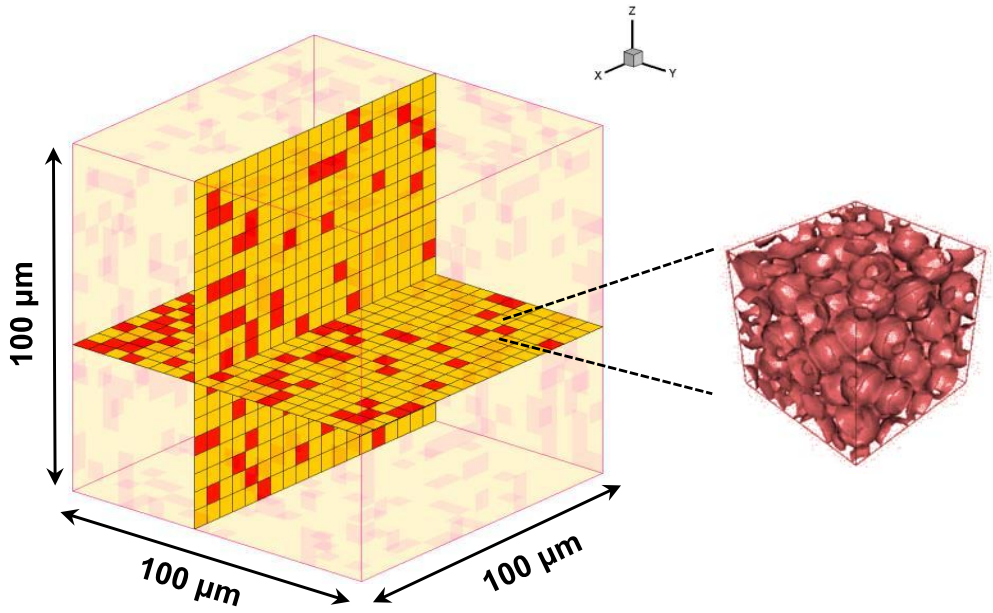

Figure 2.1: Cross sections of a single shale matrix show kerogen grid blocks (red squares) are randomly distributed in the inorganic frame (yellow). Kerogen grid blocks can sit directly adjacent to other kerogen, inorganic, or fracture grids with no limitation. This shale matrix is surrounded by fracture grid blocks (not shown in the picture). Shown in the right side, each grid block system (kerogen and inorganic) has its own porosity, permeability, density, wettability, etc.

As also predictable by its organic nature, kerogen is considered to be oil–wet [4, 20, 21]. This is important because it can directly affect capillary pressure and relative permeability. Our results show the indispensable role of such properties in simulating hydrocarbon transport process in shale, which stresses out the necessity of better characterizing kerogen in shale matrix to come up with more realistic models. Although different shale samples may show significant variations in microstructure, kerogen with reported pore sizes ranging from a few nanometers up to micrometer, is thought to play an important role in hydrocarbon transport processes and permeability pattern in shale as it is considered by the majority of researches to have a fairly

high porosity [4, 6, 9, 20]. On one hand, high capillary pressure in oil–wet kerogen, due to small pore throat sizes in shale, could cause this media to pull hydrocarbon (mainly oil) and store it into itself; on the other hand, large connected network of highly porous kerogen could reach a percolation threshold and produce a pathway for movement of hydrocarbons (mainly gas) within the shale. Being mostly made of carbon–rich material, with a high surface ratio, kerogen is considered to adsorb hydrocarbon molecules onto its surface. As pressure drops in the reservoir, adsorbed hydrocarbons will desorb into the gas phase and can be produced at a later time.

Kerogen grid blocks in the shale matrix are distributed within an inorganic frame. Inorganic matter is mainly composed of quartz, clay minerals, carbonate, pyrite, etc. Porosity of the inorganic matter appears to be a place of debate as different authors have reported somehow contradictory results, which may somehow be attributed to considerable variations in microstructure of different shale plays [4, 5, 14]. In this paper, however, we will assume the inorganic matter has slightly lower porosity compared to the kerogen. Researches suggested that the wettability of inorganic matter differs from that of kerogen where inorganic matter is considered to be water–wet [21, 22] or mixed–wet [23]. Having a designated inorganic sub–medium with water–wet characteristics mainly contributes to the ability to better model dynamic water behavior. Despite kerogen, hydrocarbon adsorption in the inorganic matter might be so weak as to be neglected under moisture conditions. In fact, inorganic matter can store hydrocarbons only through compressed fluid accumulated in its pores. Geological evidences show that pore sizes in the shale matrix (kerogen and inorganic matter) are very small. Although the continuum flow assumption and Darcy equation can still be used to model liquid (water or oil) flow in shale; such models fail to accurately predict gas flow behavior because of the significance of molecule/wall collisions and the consequent rarefaction effects. Our current model

will account for such a deviation from conventional gas flow behavior by incorporating a second-order slip boundary condition and a correction term expressed as rarefaction coefficient. This mechanism is considered to occur for the gas phase flow in both kerogen and inorganic matter but the coefficients vary based on the mean pore sizes in those media. More information about hydrocarbon desorption and flow mechanisms will follow. Note that there are some other types of complexities related with shale reservoirs like variation of phase behavior and fluid properties as a result of pore proximity effects and these effects [24, 25], which will be discussed later in this dissertation. Inorganic and kerogen grid blocks in the model are surrounded by high permeability natural or hydraulic fracture grids. This grid network of natural fracture serves as a pathway to connect the shale matrix to the hydraulic fracture system and wellbore. During the production period, hydrocarbon flows from matrix into the natural fracture network and the pressure within the fracture network can be immediately depleted to the level of the bottomhole pressure. Numerous kerogen flakes can be crossed by high permeability fractures and act as hydrocarbon sources for those pathways. Figure 2.2 shows a schematic of the mass transfer between different porosity systems in our model.

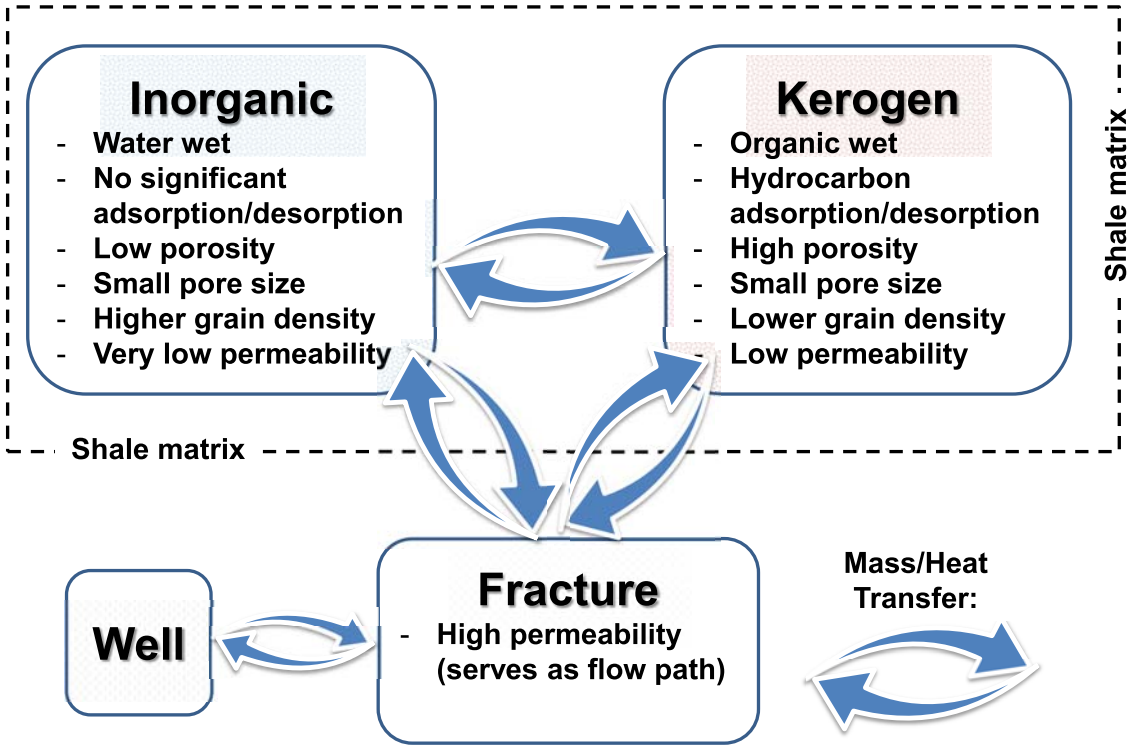

Figure 2.2: Schematic of the current model and the way different porosity systems are connected to each other. According to the figure, kerogen or inorganic grids can be connected to each other with no limitations and the grids at the faces of the matrix are connected to the fracture network. Hydrocarbon production and water imbibition happens only though fracture grids.

2.3 Fundamental equations of flow and storage

2.3.1 Flow mechanisms and formulation

When considering fluid flow mechanisms in conventional reservoirs (with relatively larger pore throat sizes), classical flow equations and continuum theory (momentum transfer by means of bulk phase viscosity; fluid velocity matches solid velocity at walls) holds true and Darcy equation can be used to calculate the mass transfer rate:

$$v = \frac{K}{\mu} \nabla P \tag{2.2}$$

where v is the fluid velocity, K is intrinsic permeability of reservoir, μ is fluid viscosity and ∇P is pressure gradient (all in consistent units). This equation, and the assumption of zero slip velocity, are true generally when the pore throat size is not less than 1 µm. On the other hand, in shale we have different pore sizes that might be as small as 5 nm or larger than a few micrometers. Although continuum assumption is still applicable for the liquid phase flow behavior; for such small pore radii, pore size becomes comparable to the mean free path of the molecules (defined as the mean length of a path covered by a molecule between subsequent collisions) in the gas phase. This means molecule/pore wall collisions become important as gas molecules strike the pore walls and tend to slip at walls instead of having zero velocity. Consequently, rarefaction effects become more important and thus pressure drop, shear stress, heat flux, and related mass transfer rate in the gas phase cannot be calculated using standard flow and heat transfer formulas based on the continuum assumption. To use the appropriate flow equation in such situations we should first identify the gas flow regime in porous media. Employing dimensionless Knudsen number as the ratio of mean free path of molecules to the hydraulic radius of pores in porous media, we can identify the corresponding flow regime.

$$K_{\mathrm{n}} = \frac{\lambda}{r_{\mathrm{h}}} \tag{2.3}$$

in which K_{n} is Knudsen number (dimensionless), λ is the mean free path of gas molecules and r_{h} is the mean hydraulic radius of pores in porous media (both in consistent units). Knudsen number is in fact, a measure of the degree of rarefaction of gases encountered in flow through narrow pores. Schaaf and Chambre [26], Roy et al. [27], and Mahulikar et al. [28] classified different regimes of gas flow and appropriate flow equations depending on Knudsen number (Figure 2.3).

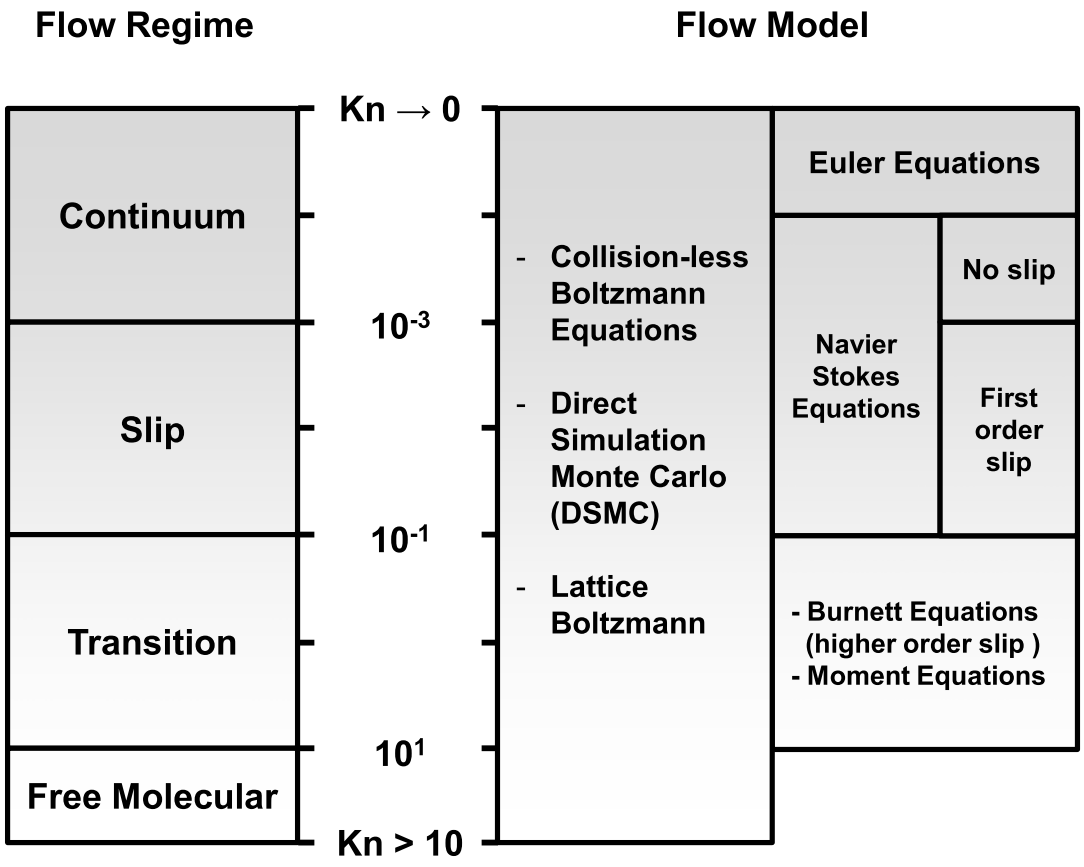

Figure 2.3: Classification of different flow regimes and corresponding flow equations based on dimensionless Knudsen number (K_{n}) (reprinted after Schaaf and Chambre [26], Roy et al. [27], and Mahulikar et al. [28]) shows that continuum flow does not hold true when pore diameter becomes comparable to that of the molecule mean free path.

For K_{n} less than 0.001, the hydraulic radius of pores is fairly larger than the mean free path of molecules, meaning that the molecule/wall interactions become negligible and Navier–Stokes equations with no–slip boundary condition can be applied. For Knudsen numbers being in the range of 0.001 to 0.1 (slip flow), mean free path of molecules becomes comparable to the pore radius and molecule/wall interactions start becoming significant. Based on Figure 2.3, for this region, Navier–Stokes

equations with a first–order slip boundary condition can be used to account for the slippage occurring as a result of molecules colliding the walls of pores. As Knudsen number further increases (0.1 to 10), there will be a "transition" region between slip type flow and free molecular type flow. The dual nature of this specific region, called transition flow regime, makes flow modeling such a challenging problem as continuum assumptions break down while approaches like molecular dynamics (MD) or probabilistic models like direct simulation Monte Carlo (DSMC) are prohibitively expensive in terms of computational cost. Being able to find an accurate and computationally efficient mass transfer model in this region is of a considerable importance for us as our calculations show that gas flow in shale reservoirs will be characterized as either slip or transition regime (Knudsen number will be between 0.05 to 3). Knudsen numbers of 10 and more are categorized as the free molecular regime and are not the subject of discussion in this research.

Beskok and Karniadakis [29] proposed a unified physics-based model, using a second-order slip boundary condition and a correction term expressed as rarefaction coefficient to predict volumetric and mass flow rates as well as pressure distribution in pores, which is appropriate for all rarefaction regimes and different pore geometries. Our mass transfer calculation in this chapter is based on the Beskok and Karniadakis [29] formulation with some modifications to account for the non–tube irregular shape of pores in hydrocarbon reservoirs with a tortuous flow path [30]. Alternative ways of addressing gas flow mechanisms in shale are also addressed in a number of other works [31, 32, 33]. Formulas are presented compatible with the conventional petroleum engineering nomenclature so it can be conveniently incorporated into the simulators. To find the gas phase mass flow rate in tight pores of shale reservoirs, we should first find Knudsen number based on Equation 2.3. The real gas mean free path in

Equation 2.3 is calculated using Roy et al. [27] formulation:

$$\lambda = \frac{16\mu}{5\rho\sqrt{\frac{2\pi \mathrm{R}T}{M}}} \tag{2.4}$$

Replacing density based on the compressibility factor, Equation 2.4 becomes

$$\lambda = \frac{16z\mu}{5P}\sqrt{\frac{\mathrm{R}T}{2\pi M}} \tag{2.5}$$

In these equations, λ is the mean free path (m), μ is gas viscosity (Pa.s), ρ is gas density (kg/m^3), R is the universal gas constant (8314.46 J/kmol/K), T is absolute temperature (K), P is pressure (Pa), z is the gas compressibility factor (z-factor), and M is the gas molecular weight (kg/kmol or gr/mol). There are numerous equations in literatures correlating hydraulic pore radius of the porous media (r_h) to different reservoir rock properties. In this paper, we will use the equation presented by Civan [30]. The reader is referred to the related articles for detailed information about these correlations. The value of hydraulic radius to be used in Equation 2.3 is calculated by

$$r_\mathrm{h} = 2\sqrt{2\tau}\sqrt{\frac{K}{\phi}} \tag{2.6}$$

where τ is the tortuosity (unitless), K is the intrinsic permeability (m^2), and ϕ is porosity (unitless, fraction). Inserting Equations 2.5 and 2.6 into Equation 2.3, one can calculate dimensionless Knudsen number. Based on the value of Knudsen number, Beskok and Karniadakis [29] (and later adopted into the conventional petroleum engineering nomenclature by Civan [30]), presented the following formula, which is valid in the entire Knudsen number range and second–order accurate in the slip flow

regime, to characterize rarefied gases flow in small pores:

$$\frac{K_{\text{apparent}}}{K} = (1 + \alpha K_{\text{n}})(1 + \frac{4K_{\text{n}}}{1 - bK_{\text{n}}}) \tag{2.7}$$

where, K is the intrinsic permeability, K_{apparent} is the apparent permeability (both in consistent units), and K_{n} is Knudsen number. Coefficients b and α will be explained in the following discussion. In this research, we have used the concept of apparent permeability as a way to incorporate the effect of gas slippage into our simulator. In fact, for the gas phase flow, the apparent permeability, which is somehow larger than the intrinsic permeability, will replace K in Equation 2.2. This new gas phase flow calculation formula will account for the improved mass transfer mechanism due to molecule/wall interactions in tight media. Equation 2.8 represents a generalized form of gas phase velocity in a water–gas–oil three–phase system.

$$v_{\text{G}} = \frac{K_{\text{apparent}} K_{\text{rG}}}{\mu_{\text{G}}} \nabla P_{\text{G}} \tag{2.8}$$

Here, v_{G} is the gas phase velocity, K_{apparent} is gas phase apparent permeability, K_{rG} represents the gas relative permeability, μ_{G} is the gas viscosity, and ∇P_{G} is the gas pressure gradient (all in consistent units). In Equation 2.7, the term $1 + \alpha K_{\text{n}}$ is considered to be the rarefaction coefficient correction that is introduced to the model to account for the increased rarefaction effects for higher Knudsen numbers with α defined as a function of Knudsen number. The term b in Equation 2.7, defined as the slip coefficient, is an empirical parameter to be determined experimentally or from linearized Boltzmann or direct simulation Monte Carlo (DSMC). The physical meaning of b is the vorticity flux into the surface divided by the vorticity of flow field on the surface [29]. The value of $b = 0$ corresponds to the Maxwell's first–order

boundary condition and generates erroneous results for Knudsen numbers in the interest range of this research, as a consequence of breakdown of the slip flow theory based on the first–order slip boundary conditions. Instead, $b = -1$ (corresponding to the general second–order boundary condition) has been reported to predict the flow more accurately (this value is used in work as it generates more reliable data for the flow regime of interest). Being computationally efficient to be implemented into reservoir simulators, the current model will provide fairly accurate predictions in certain Knudsen ranges. However, it should not keep us from mentioning the fact that this model ignores the effect of "Knudsen layer" (a local thermodynamically nonequilibrium region, due to molecule/wall interactions, extending proportional to the mean free path of molecules [34]). For small values of K_{n}, the Knudsen layer is thin and does not affect the slip velocity calculations considerably. As K_{n} increases to an intermediate range, both fully developed viscous flow (boundary layer) and Knudsen layer appear in the pore. Beskok and Karniadakis [29] have reported an error of 10% in slip velocity at $b = -1$ as a result of this ignorance. The coefficient α in Equation 2.7 is a function of Knudsen number and varies from zero in the slip flow regime to an appropriate constant value (α_0) in the free molecular flow regime ($K_{\mathrm{n}} \to \infty$). Equation 2.9 represents the relation between α and Knudsen number [29]:

$$\alpha = \alpha_0 \frac{2}{\pi} \tan^{-1}(\alpha_1 K_{\mathrm{n}}^{\beta}) \tag{2.9}$$

where $\alpha_1 = 4.0$ and $\beta = 0.4$ are correlation constants. The value of α_0 is calculated by equalizing the theoretical mass flow rate in the free molecular flow regime and the asymptotic mass flow rate calculated using the general second–order boundary condition when $K_{\mathrm{n}} \to \infty$

$$\alpha_0 = \frac{64}{3\pi(1 - \frac{4}{b})} \tag{2.10}$$

in which the slip coefficient (b) is equal to -1 for the general second–order boundary condition. Some alternative regression–based formulas for calculating α have been discussed by Civan [30]. Appendix A includes the F90 source code to calculate apparent permeability to the gas phase.

2.3.2 Multi-component adsorption

The process in which a solid surface binds molecules of other types to itself is called adsorption. In fact, it is a surface phenomenon caused by intermolecular attractive forces between the solid surface and fluid. Adsorption depends on different factors like the molecular structure of the solid surface, the polarization and size of molecules, and their interaction with the solid. The relation between amount of fluid adsorbed on the solid surface (here we consider that to be our porous media) and pressure/temperature is referred to as "adsorption model." Although not extensively evaluated for the case of unconventional organic shales, the authors believe the commonly used empirical models like the Langmuir isotherm are practically accurate to be used in such reservoirs. Butler and Ockrent [35] were the first to "extend" the Langmuir model (originally presented by Langmuir [36]) for competitive adsorption. This model assumes a homogeneous surface of energy adsorption, no interaction between adsorbed species, and that all adsorption sites are equally available for all adsorbed species. In this work, the extended Langmuir model is used in the following form:

$$V_{\mathrm{g}i} = \frac{V_{\mathrm{L}i}\frac{P_i}{P_{\mathrm{L}i}}}{1 + \sum_{j=1}^{\mathrm{n}} \frac{P_j}{P_{\mathrm{L}j}}} \tag{2.11}$$

in which $V_{\mathrm{g}i}$ is the adsorption capacity (m^3 (of adsorbed gas at standard condition) /kg (of rock)) of component i, $V_{\mathrm{L}i}$ is the Langmuir volume for component i (m^3/kg), P_i and P_j are partial pressures of components i and j in the gas phase (Pa), and

finally $P_{\mathrm{L}i}$ and $P_{\mathrm{L}j}$ represent the Langmuir pressure for individual components i and j (pressures at which half of the gas capacity V_{L} remains adsorbed, Pa). Appendix B includes the F90 source code to calculate multi–component desorption.

2.3.3 Mass balance equation

In this paper three–phase aqueous, organic (the term "oil phase" might be used interchangeably), and gas flow is considered in the shale reservoir where three different components (water, light oil, and gas) are distributed between those phases. We assume that the mutual solubility of water and hydrocarbon components (organic and gas phase) is negligible, but the light oil and gas component can be transformed between the organic and gas phase using appropriate dissolution functions. The governing mass balance equation for the gas component is written as

$$\nabla.\left(X_{\mathrm{G}}^{\mathrm{g}}\rho_{\mathrm{G}}\frac{K_{\mathrm{apparent}}K_{\mathrm{rG}}}{\mu_{\mathrm{G}}}(\nabla P_{\mathrm{G}}+\rho_{\mathrm{G}}\mathrm{g}\nabla z)+X_{\mathrm{O}}^{\mathrm{g}}\rho_{\mathrm{O}}\frac{KK_{\mathrm{rO}}}{\mu_{\mathrm{O}}}(\nabla P_{\mathrm{O}}+\rho_{\mathrm{O}}\mathrm{g}\nabla z)\right) = -\frac{\partial(X_{\mathrm{G}}^{\mathrm{g}}\rho_{\mathrm{G}}S_{\mathrm{G}}\phi+X_{\mathrm{O}}^{\mathrm{g}}\rho_{\mathrm{O}}S_{\mathrm{O}}\phi)}{\partial t}-\frac{\partial(q_{\mathrm{g,adsorbed}}(1-\phi))}{\partial t} \quad (2.12)$$

and for the oil component as

$$\nabla.\left(X_{\mathrm{G}}^{\mathrm{o}}\rho_{\mathrm{G}}\frac{K_{\mathrm{apparent}}K_{\mathrm{rG}}}{\mu_{\mathrm{G}}}(\nabla P_{\mathrm{G}}+\rho_{\mathrm{G}}\mathrm{g}\nabla z)+X_{\mathrm{O}}^{\mathrm{o}}\rho_{\mathrm{O}}\frac{KK_{\mathrm{rO}}}{\mu_{\mathrm{O}}}(\nabla P_{\mathrm{O}}+\rho_{\mathrm{O}}\mathrm{g}\nabla z)\right) = -\frac{\partial(X_{\mathrm{G}}^{\mathrm{o}}\rho_{\mathrm{G}}S_{\mathrm{G}}\phi+X_{\mathrm{O}}^{\mathrm{o}}\rho_{\mathrm{O}}S_{\mathrm{O}}\phi)}{\partial t}-\frac{\partial(q_{\mathrm{o,adsorbed}}(1-\phi))}{\partial t} \quad (2.13)$$

in which $X_{\mathrm{G}}^{\mathrm{g}}$ and $X_{\mathrm{G}}^{\mathrm{o}}$ are mass fractions of the gas and oil component in the gas phase, $X_{\mathrm{O}}^{\mathrm{g}}$ and $X_{\mathrm{O}}^{\mathrm{o}}$ are mass fractions of the gas and oil component in the organic phase, P_{G}, ρ_{G}, μ_{G}, S_{G} and K_{rG} are gas phase pressure, density, viscosity, saturation, and relative permeability, P_{O}, ρ_{O}, μ_{O}, S_{O} and K_{rO} represent organic phase pressure, density, viscosity, saturation, and relative permeability with ϕ, z, and g accounting

for porosity, elevation, and gravity constant. As mentioned in previous sections, K is the intrinsic permeability and K_{apparent} is the apparent permeability to the gas phase (slippage effect is considered here). $q_{\text{g,adsorb}}$ is mass of the gas component adsorbed in the unit volume of media and $q_{\text{o,adsorb}}$ is that of the oil component. Note that all these variables should be used in consistent units. Mass balance equation for the water component is as follows

$$\nabla.\left(\rho_{\text{A}}\frac{KK_{\text{rA}}}{\mu_{\text{A}}}(\nabla P_{\text{A}}+\rho_{\text{A}}\text{g}\nabla z)\right)=-\frac{\partial(\rho_{\text{A}}S_{\text{A}}\phi)}{\partial t} \tag{2.14}$$

where P_{A}, ρ_{A}, μ_{A}, S_{A} and K_{rA} represent aqueous phase pressure, density, viscosity, saturation, and relative permeability. In these equations, t represents time. The summation of aqueous, organic, and gas phase saturation values is equal to unit. Depending on the wettability of each medium, phase pressures (P_{A} ,P_{G} ,and P_{O}) are related to each other through capillary pressure. In Equations 2.12 through 2.14, the left hand side refers to the component mass flux and the right hand side represents the accumulation term. Since gas and light oil components exist in both organic (or oil) and gaseous phase (hydrocarbon dissolution in the aqueous phase is neglected), their flux term includes both of these phases, and in analogy, their accumulation term covers the compressed storage of both organic and gaseous phases and desorption of the gaseous phase. For the water component, it becomes easier since we assume water component exists only in the aqueous phase, which means that the dynamics of water component transport goes through Darcy flow and compressed storage of the aqueous phase. Gas and liquid phase thermodynamic properties are calculated using Peng–Robinson Equation of State (Peng and Robinson [37]). Mass balance equations are discretized in space using the integrated finite difference concept [38]. This approach provides a general discretization scheme to handle up to three dimensional

domains with a set of discrete meshes. Each mesh has a certain control volume for a proper averaging or interpolation of transport properties or thermodynamic variables. Time discretization in our simulator is performed using a backward, first order, fully implicit finite difference scheme.

2.4 Model specifications and system properties

As mentioned earlier, based on numerous geological data, the distribution of kerogen in inorganic minerals and the size of natural fractures are reported to be on the order of a micrometer. Hence, it looks reasonable to develop a model with similar dimensions if subdivision of shale matrix is necessary. In this case, a single shale matrix cuboid is simulated using a 100 µm 100 µm 100 µm model (Cartesian 3D) where the surrounding fracture network has a fracture aperture of 1 µm (total of 10648 grid blocks). The number of organic and inorganic grid blocks in the matrix is determined using Equation 2.1. The TOC value for this reference model is 9.5 wt%. Before starting the simulation, the model is initialized with the current capillary pressure functions and the resulting equilibrium values are found. A constant pressure boundary condition (pressure in the fracture network) is applied at outer boundaries of the model where pressure of the fracture is kept constant at 10 MPa (1450 psi). Depending on the drive mechanism, we will consider fracture to be fully saturated with water, from which water can imbibe into the shale matrix at later production times, or containing just hydrocarbons with no water. Initial pressure in the inorganic matter is set at 32.3 MPa (4680 psi) while that of kerogen is 37.8 (5475 psi). Kerogen and inorganic grids have different water and hydrocarbon initial saturations as well. Mainly composed of carbon containing material, kerogen is believed to be the sole source of hydrocarbon generation during diagenesis and thermal maturation process. This generated hydrocarbon will later migrate to the adjacent

zones and partially saturate those media. That being said, kerogen is considered to be mostly filled with hydrocarbon with a low initial water saturation (5%). On the other hand, water–wet inorganic media contains higher amounts of initial water (30%) and the rest of media is occupied by either oil and/or gas.

Due to the fact that our current model decomposes liquid–rich shale matrix into two different sub–domains (kerogen and inorganic) in a mixed–wet system with three–phase gas–oil–water flow occurring in the pore system, assigning appropriate multi–phase related properties (relative permeability and capillary pressure) to each medium is extremely important. Water dynamics in shale reservoirs is important during the hydraulic fracturing and hydrocarbon production period. Because of its affinity to the inorganic matter and high capillary pressure in such tight medium, water is likely to be imbibed into the shale matrix. Although a large quantity of research has studied different aspects of capillary pressure in shale reservoirs, this phenomenon still stays ambiguous due to the complex interactions of water molecules with extremely small scale pores in organic shale. In this paper, the original formulation of Brooks and Corey is employed to model capillarities [39]. The Brooks and Corey capillary pressure function was not originally derived for shale with such small pore sizes; however, because of the similarities in mineralogy and petrophysical properties of the shale and sand type reservoirs, the authors believe this formula is still applicable for shale by using the appropriate rock characterization parameters (pore size distribution and capillary entry pressure). Equations 2.15 and 2.16 are used for capillary pressure calculations:

$$P_{\mathrm{c}} = P_{\mathrm{e}}(S)^{-\frac{1}{\lambda_{\mathrm{p}}}} \tag{2.15}$$

$$S_{\mathrm{e}} = \frac{S_{\mathrm{wet}} - S_{\mathrm{wetr}}}{1 - S_{\mathrm{wetr}}} \tag{2.16}$$

in which P_c is the capillary pressure at a wetting phase saturation of S_{wet}, λ_p is the pore size distribution factor, and P_e is the capillary entry pressure (in consistent units). Residual wetting phase saturation is depicted by S_{wetr} in the formula. Higher porosity of the kerogen compared to the inorganic matter (see section 2.2) and the fact that some authors have demonstrated kerogen pores to form the major connected or effective pore network in some shale plays like Barnett [5, 7, 9] have led us to consider a higher permeability and lower capillary pressure in kerogen. Figure 2.4 shows the capillary pressure graphs used in our micro–scale model.

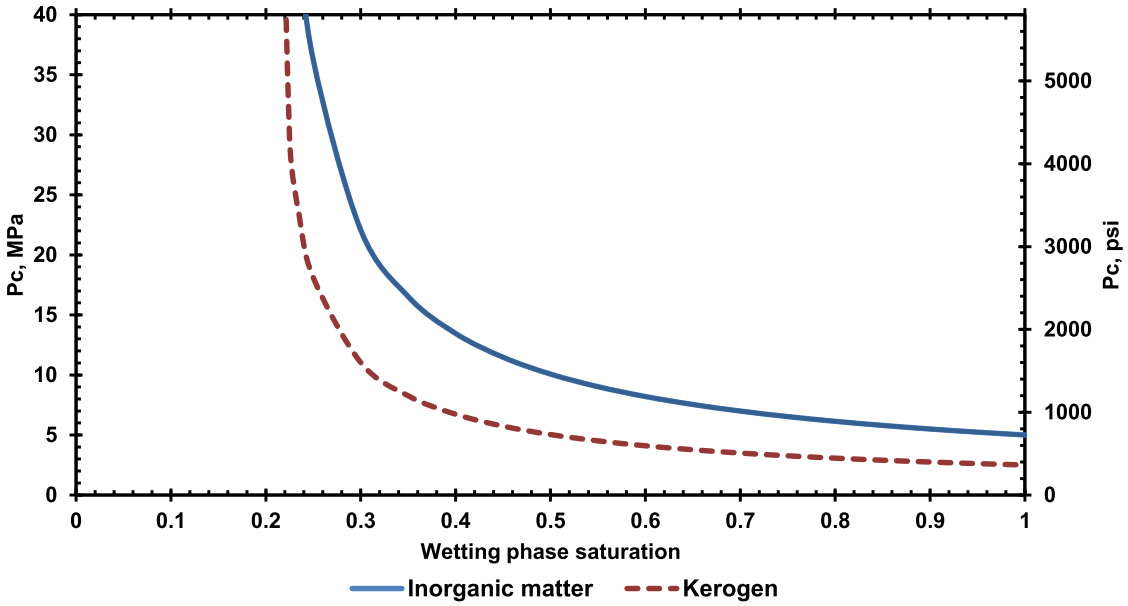

Figure 2.4: Different capillary pressure curves are used for the inorganic and kerogen grid blocks in this model where the capillary pressure value in inorganic matter (blue solid line) is assumed to be larger than that of kerogen (red dashed line).

Three–phase relative permeability in our model is calculated using the modified Stone I model [40]. Before starting the discussion, it is helpful to mention that in all the following calculations S_{wet} stands for the wetting phase saturation, S_{inrwet}

represents the intermediate wetting phase saturation, and S_{nonwet} is the non–wetting phase saturation in porous media occupied by oil, gas, and water where $S_{\text{wet}}+S_{\text{inrwet}}+S_{\text{nonwet}}=1$. Three–phase relative permeabilities of the wetting, intermediate wetting, and non–wetting phases are denoted by $K_{\text{r,wet}}$, $K_{\text{r,inrwet}}$, and $K_{\text{r,nonwet}}$ respectively. In the modified Stone I approach, the wetting phase relative permeability (water is the wetting phase in inorganic matter while oil is the wetting phase in kerogen) depends only on the wetting phase saturation ($K_{\text{r,wet}} = f(S_{\text{wet}})$) and non–wetting phase relative permeability (gas in the inorganic matter and water in kerogen) is calculated solely based on the non–wetting phase saturation ($K_{\text{r,nonwet}} = g(S_{\text{nonwet}})$). In other words, functions f and g in these formulas can be any appropriate two–phase relative permeability relations (Figure 2.5) where the wetting phase saturation used in f is S_{wet} and assuming the rest of media is occupied by a fictitious non–wetting fluid that has a saturation of $1-S_{\text{wet}}$. On the other hand, g is calculated considering a non–wetting phase saturation of S_{nonwet} where the remainder of the pore space is occupied by a fictitious wetting phase with a saturation of $1-S_{\text{nonwet}}$. Wetting phase *two–phase* relative permeability function (f) is considered to be the same for both drainage and imbibition and is calculated using relative permeability functions specifically derived for shale reservoirs [41]:

$$K_{\text{r,wet}} = f(S_{\text{wet}}) = \left(\frac{S_{\text{wet}} - S_{\text{wcw}}}{1 - S_{\text{wcw}}}\right)^{n_{\text{w}}} \tag{2.17}$$

where S_{wcw} is the critical wetting phase saturation with respect to the wetting phase and n_{w} is the wetting phase drainage/imbibition exponent.

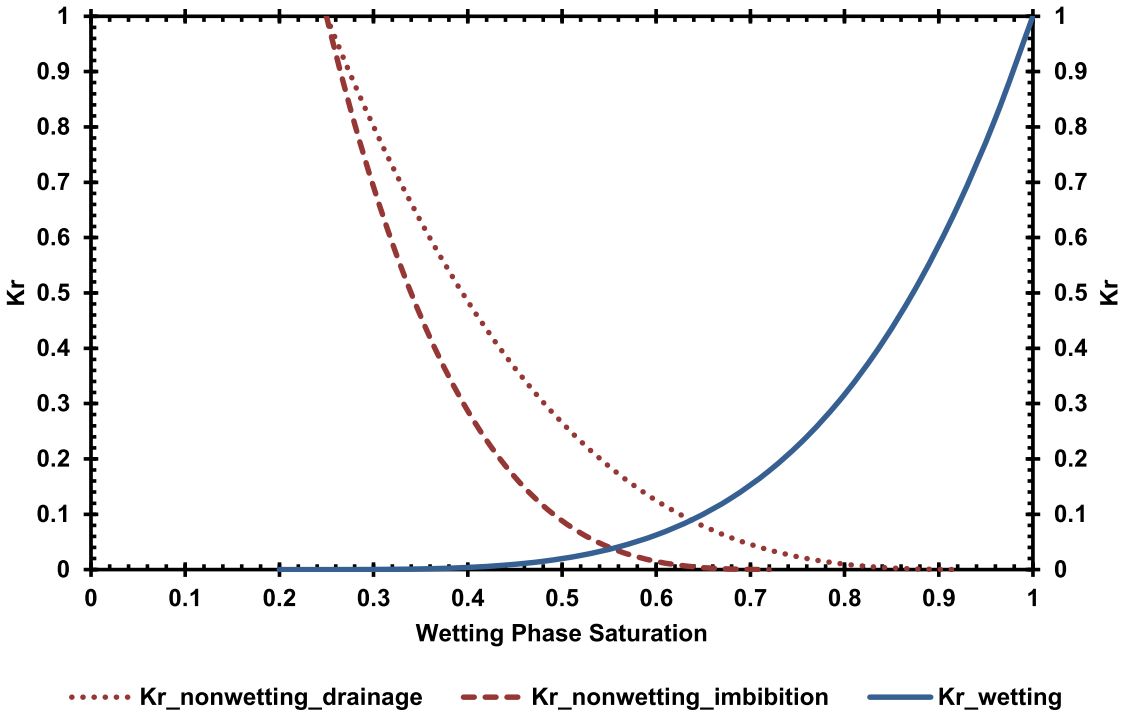

Figure 2.5: Two–phase relative permeability curves used to calculate three–phase relative permeability in shale. While both imbibition and drainage processes follow the same wetting phase relative permeability curve, the non–wetting phase has two different curves for drainage and imbibition relative permeabilities.

Non–wetting phase *two–phase* relative permeability function (g), however, is different for the drainage and imbibition case. For drainage, the following formulation is employed for *shale reservoirs* [41]:

$$K_{\mathrm{r,nonwet}} = g(S_{\mathrm{nonwet}}) = \left(1 - \frac{(1 - S_{\mathrm{nonwet}}) - S_{\mathrm{wcnw}}}{1 - S_{\mathrm{nwc}} - S_{\mathrm{wcnw}}}\right)^{n_{\mathrm{nwd}}} \tag{2.18}$$

in which S_{wcnw} is the critical wetting phase saturation with respect to the non–wetting phase, S_{nwc} is the critical non–wetting phase saturation, and n_{nwd} is the non–wetting phase drainage exponent. The function for the imbibition case in shale is written as

[41]

$$K_{\mathrm{r,nonwet}} = g(S_{\mathrm{nonwet}}) = \left(1 - \frac{(1 - S_{\mathrm{nonwet}}) - S_{\mathrm{wi}}}{1 - S_{\mathrm{wi}} - S_{\mathrm{nwt}}}\right)^{n_{\mathrm{nwi}}} \tag{2.19}$$

where S_{wi} is the initial wetting saturation, S_{nwt} is the non–wetting trapped saturation, and n_{nwi} is the non–wetting phase imbibition exponent.

To calculate the intermediate wetting phase (gas phase in kerogen and oil phase in inorganic) three–phase relative permeability ($K_{\mathrm{r,inrwet}}$), we first define the following auxiliary functions

$$S^*_{\mathrm{inrwet}} = \frac{S_{\mathrm{inrwet}} - S_{\mathrm{inrwr}}}{1 - S_{\mathrm{wc}} - S_{\mathrm{inrwr}}} \tag{2.20}$$

$$S^*_{\mathrm{wet}} = \frac{S_{\mathrm{wet}} - S_{\mathrm{wc}}}{1 - S_{\mathrm{wc}} - S_{\mathrm{inrwr}}} \tag{2.21}$$

$$S^*_{\mathrm{nonwet}} = \frac{S_{\mathrm{nonwet}}}{1 - S_{\mathrm{wc}} - S_{\mathrm{inrwr}}} \tag{2.22}$$

Here, S_{inrwr} is the intermediate wetting phase residual saturation and S_{wc} represents the wetting phase critical saturation. We then define $h(S_{\mathrm{wet}})$ for the drainage case as

$$h(S_{\mathrm{wet}}) = \left(1 - \frac{S_{\mathrm{wet}} - S_{\mathrm{wcnw}}}{1 - S_{\mathrm{nwc}} - S_{\mathrm{wcnw}}}\right)^{n_{\mathrm{nwd}}} \tag{2.23}$$

and for the imbibition one as

$$h(S_{\mathrm{wet}}) = \left(1 - \frac{S_{\mathrm{wet}} - S_{\mathrm{wi}}}{1 - S_{\mathrm{wi}} - S_{\mathrm{nwt}}}\right)^{n_{\mathrm{nwi}}} \tag{2.24}$$

Although the definition of parameters used in Equations 2.23 and 2.24 are the same as those in Equations 2.18 and 2.19, the values of those parameters are not necessarily identical in both cases (Equations 2.18 and 2.19 correspond to the non–wetting/intermediate wetting two–phase relative permeability case while Equations 2.23 and 2.24 refer to the wetting/intermediate wetting case). To avoid overcompli-

cating the situation, we will use the same nomenclature for these cases here. Next step is to consider $l(S_{\text{nonwet}})$ as

$$l(S_{\text{nonwet}}) = \left(\frac{(1 - S_{\text{nonwet}}) - S_{\text{wcw}}}{1 - S_{\text{wcw}}} \right)^{n_{\text{w}}} \tag{2.25}$$

The previous statement about the definition of the parameters and their values holds true in case of comparing Equations 2.17 and 2.25. Introducing a relative permeability normalization factor (ω) equivalent to the effective relative permeability of the intermediate wetting phase when the non–wetting phase saturation is equal to zero and the wetting phase saturation is equal to its critical saturation (S_{wc}), we have

$$\beta_{\text{wet}} = \frac{h(S_{\text{wet}})}{(1 - S^*_{\text{wet}}) \times \omega} \tag{2.26}$$

$$\beta_{\text{nonwet}} = \frac{l(S_{\text{nonwet}})}{(1 - S^*_{\text{nonwet}}) \times \omega} \tag{2.27}$$

Finally, combining Equations 2.20, 2.26, and 2.27 with the relative permeability normalization factor (ω), the intermediate wetting phase three–phase relative permeability ($K_{\text{r,inrwet}}$) is written as Equation 2.28. Table 2.1 depicts the main dimensions of our micro–scale model.

$$K_{\text{r,inrwet}} = \omega S^*_{\text{inrwet}} \beta_{\text{wet}} \beta_{\text{nonwet}} \tag{2.28}$$

Table 2.1: Micro–scale model description and media/fluid properties

Model characteristic		**Value**	
		Field units	**SI units**
Permeability			
	Kerogen	700 nD	$6.9 \times 10^{-19}\text{m}^2$
	Inorganic	50 nD	$4.93 \times 10^{-20}\text{m}^2$
Capillary pressure			
Kerogen	P_e (Capillary entry pressure)	507.5 psi	$3.5 \times 10^6\text{Pa}$
	λ_n (Pore size distribution)	1.5	1.5
Inorganic	P_e (Capillary entry pressure)	725 psi	$5 \times 10^6\text{Pa}$
	λ_n (Pore size distribution)	1.4	1.4
Initial pressure			
	Kerogen	5475 psi	$3.78 \times 10^7\text{Pa}$
	Inorganic	4680 psi	$3.23 \times 10^7\text{Pa}$
	Fracture	1450 psi	$1.0 \times 10^7\text{Pa}$
Model density			
	Kerogen	84.24 lb/ft^3	1350 kg/m^3
	Inorganic	162.24 lb/ft^3	2600 kg/m^3
Multi-component desorption			
Oil component	V_L (Langmuir volume)	507.5 psi	$3.5 \times 10^6\text{Pa}$
	P_L (Langmuir pressure)	1.5	1.5
Gas component	V_L (Langmuir volume)	725 psi	$5 \times 10^6\text{Pa}$
	P_L (Langmuir pressure)	1.4	1.4
Porosity			
	Kerogen	0.2	
	Inorganic	0.04	
Relative permeability			
	S_wr	0.2	
	S_inrwr	0.15	
	S_wcnw	0.25	
	S_wcw	0.2	
	S_nwc	0.1	
	S_wi	0.25	
	S_nwt	0.25	
	n_nwd	3	
	n_nwi	3.5	
	n_w	4	
TOC		9.5 wt%	
Tortuosity		3	

2.5 Results and discussion

2.5.1 Shale matrix depletion–different mechanisms

In this section, we will discuss two different production scenarios. In the first case, fracture is considered to be fully saturated with water (constant water saturation in fracture during simulation time) where water is able to imbibe into the matrix and replace hydrocarbon. Fracture medium in the second case, however, is saturated with produced oil and gas with no water accessible for water imbibition. The main driving force for the second case is hydrocarbon expansion. Due to the small dimensions of the current simulation case, the abscissa in our graphs is plotted using a dimensionless time function, which is calculated by normalizing the actual time by the minimum simulation time step size. This will in fact represent a better picture of the simulation progress in a more readable time scale. Let us start with the water imbibition scenario (first case). Figure 2.6 shows the average pressure in the shale matrix and fracture. According to the graph, pressure in the inorganic matter decreases when hydrocarbon production starts. This is because oil and gas will leave water–wet inorganic matter (with a higher gas and organic phase pressure) towards low pressure fracture network. At later times, when pressure depletes in the matrix, aqueous phase pressure in the water–wet inorganic matter falls below the fracture pressure, resulting in a counter current water imbibition from fracture into the matrix, which has additional benefits of displacing hydrocarbon from the matrix, as mentioned by some researchers [42]. Water movement into the inorganic matrix will not be very effective during the early imbibition stages due to its low relative permeability at initial water saturations. As hydrocarbon production continues, water starts invading the shale matrix from the edges. Water saturation increases gradually and water establishes its way deep into the shale matrix to replace the depleted gas and oil (Figure 2.7). This will build up

the pressure in the inorganic matter at later production periods (solid line in Figure 2.6).

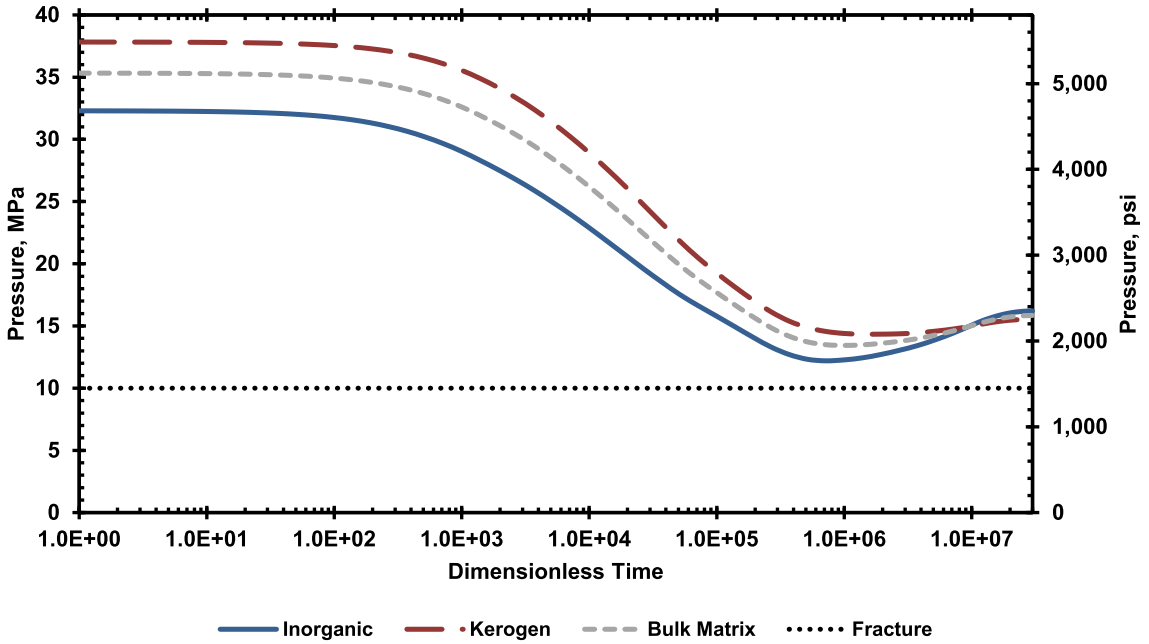

Figure 2.6: As production starts in the water imbibition scenario, pressure decreases in both kerogen and inorganic due to the hydrocarbon depletion process. At late production times, pressure in the inorganic matter increases because of water imbibition.

Average pressure in kerogen follows a trend similar to that of the inorganic matter in the early times of the simulation. In the middle stages of simulation, pressure decrease in kerogen will be slightly steeper than that of inorganic indicating a more efficient depletion process in kerogen as a result of higher permeability in kerogen and hydrocarbon movement from kerogen into the fracture. Oil movement in kerogen follows two different flow paths. One path relates to the kerogen grid blocks that are directly connected to the fracture blocks (with a lower pressure). In these con-

nections, hydrocarbon will always move from high pressure kerogen to low pressure fracture. The other flow path correlates to the connections where oil–wet kerogen grid blocks sit adjacent to the water–wet inorganic grids. In these cases, capillary pressure in shale matrix with a fairly small mean pore size plays an important role. This dual nature of oil transport in kerogen along with the gas phase movement into and out of kerogen specify pressure dynamics in this medium. Contrary to inorganic, mass transfer in kerogen is mostly limited to hydrocarbon flow (oil and gas phase) where aqueous phase saturation stays at low values without considerable changes (Figure 2.7).

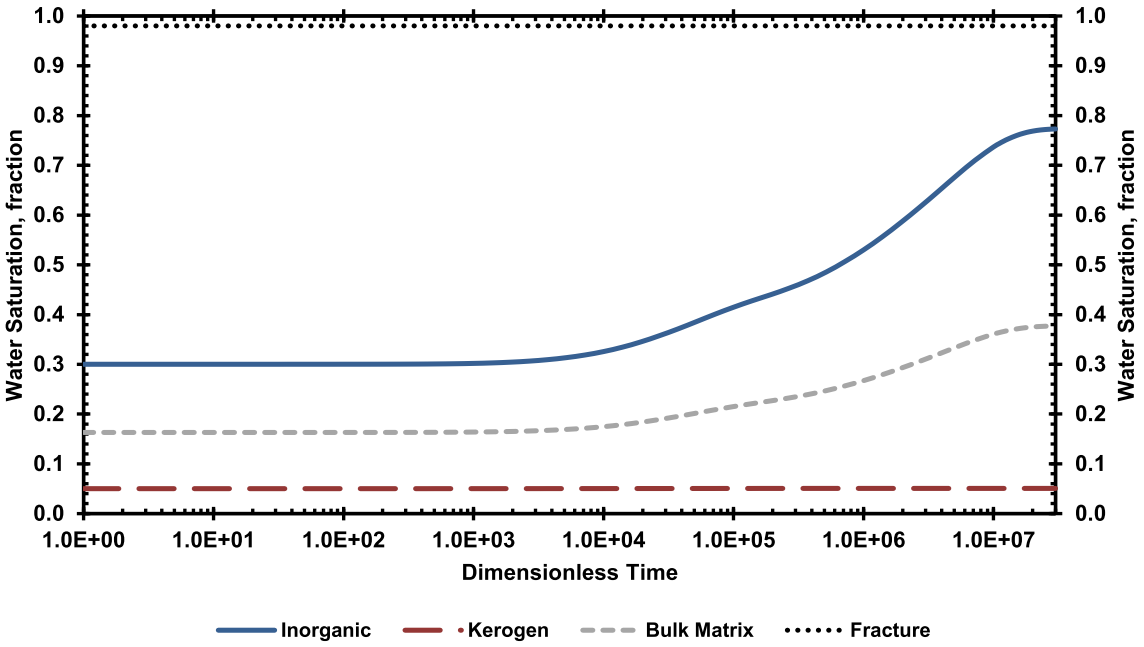

Figure 2.7: Water saturation in the inorganic matter increases (water imbibition scenario) as a result of water imbibition into the matrix later in the course of simulation. Fluid movement in kerogen is somehow limited to two–phase gas and oil flow and water phase saturation stays at low values without considerable changes.

Figure 2.8 and Figure 2.9 show oil and gas saturation in the shale matrix. As discussed before, oil and gas saturations in inorganic matter decrease as a result of hydrocarbon production and water imbibition into the inorganic matter. Mass transfer in kerogen, however, is mostly limited to two–phase flow with a very low immobile water saturation that is trapped in the small pores of kerogen. According to Figure 2.8, oil saturation in kerogen does not change considerably during the course of simulation. Looking more precisely, one can detect slight increase in oil saturation at late production periods. This is because of the oil flux from water–wet inorganic into oil–wet kerogen as a consequence of high capillary pressure in low permeability shale reservoirs and is, in fact, compensating for oil flow from kerogen to low pressure fracture.

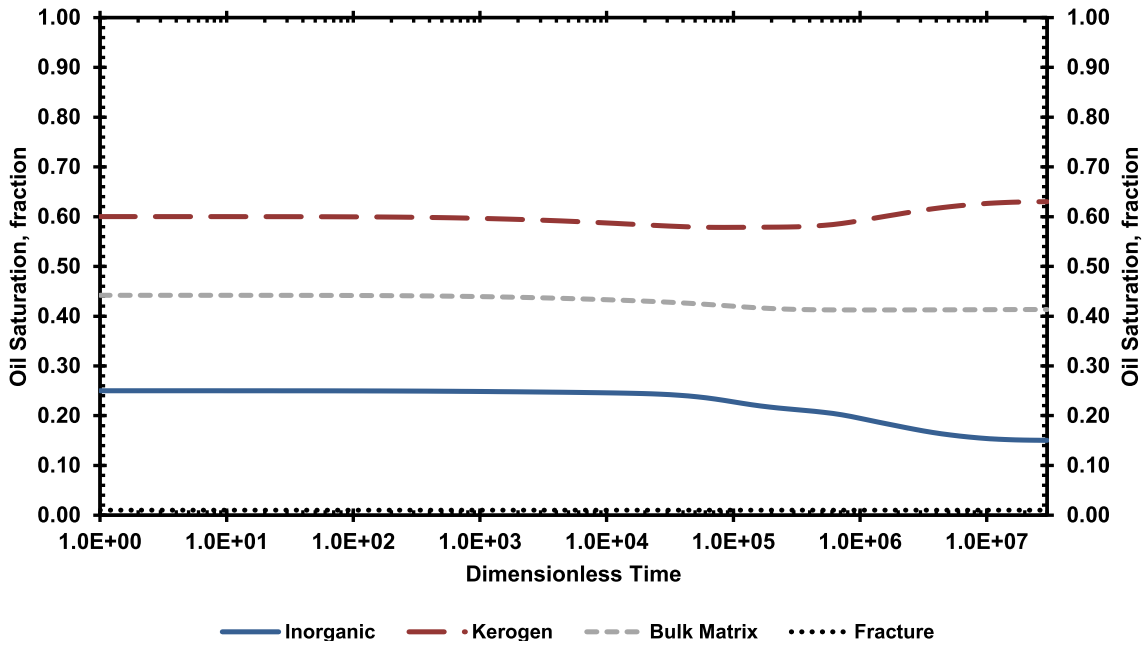

Figure 2.8: After production starts in the water imbibition scenario, oil saturation in inorganic decreases and water will replace oil in inorganic. Mass transfer in kerogen is limited to two-phase oil and gas flow where oil saturation stays almost constant in kerogen.

Similar to oil, gas saturation in kerogen does not change too much (Figure 2.9). Although the results so far show considerable changes in fluids' pressure and saturation in shale matrix during the simulation time, the conclusion should not be made that the same order of magnitude change can be expected in real shale reservoirs in a short production period. Instead, it should be noticed that changes discussed in this paper occur in a very small scale model (100 µm × 100 µm × 100 µm) and observing the same order of changes in a real field scale model of shale may require tens to hundreds of years.

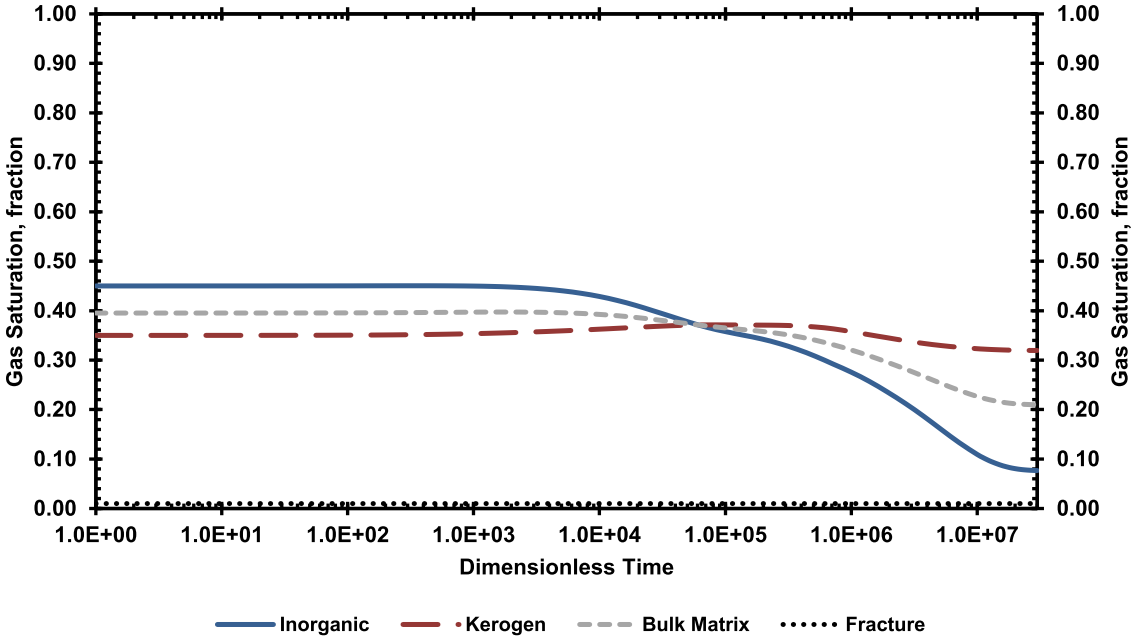

Figure 2.9: Gas saturation in the inorganic decreases as production continues and water from fracture replaces the gas phase there. In kerogen, however, gas saturation does not change substantially.

Figure 2.10 depicts the amount of gas and oil produced from matrix. Compared to the oil phase, gas shows a higher ultimate recovery. Higher gas recovery is predictable

as gas phase has a lower viscosity and at the same time, molecule/wall interactions and slip phenomenon at pore walls (discussed in section 2.3.1) will improve permeability to the gas phase. Despite the fact that the shale reservoirs discussed in this paper have considerable liquid hydrocarbon saturations (liquid–rich shale), extremely low permeability of shale matrix (in the order of nanodarcy) and high capillary pressures in such reservoirs hinder oil phase flow (modeled using regular continuum flow approach) in porous media. This problem sometimes can be severe enough to shut down the entire production process in liquid–rich shales, as the operation would not be profitable.

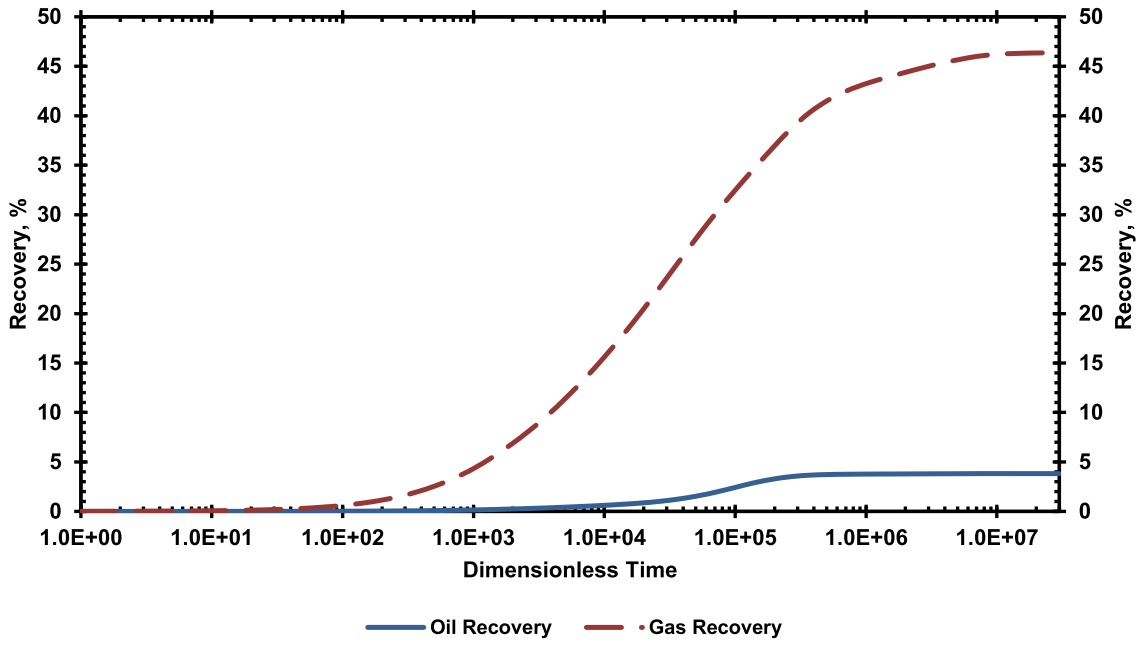

Figure 2.10: Although kerogen is a rich source of liquid hydrocarbons, very low permeability in shale hinders oil production from such reservoirs. Gas recovery, on the other hand, is higher due to its improved permeability (slip effect) and lower viscosity. Water imbibition from fracture into the inorganic mater helps to produce more hydrocarbon.

Water transfer dynamics will better be understood using 3D maps of pressure and water saturation distribution in the shale matrix at different production times (Figures 2.11 and 2.12). The red blocks in the saturation and pressure map at the early production time represent kerogen. Kerogen blocks are randomly distributed in the inorganic frame. As expected, pressure in the matrix begins to decrease as hydrocarbon production starts through the surrounding low pressure fracture network (Figure 2.11). While pressure in the matrix depletes, water saturation does not change considerably during the early stages of production (Figure 2.12). This is because water relative permeability in water–wet inorganic matter is low and water is not able to establish its way from fracture to matrix. As production continues, pressure further decreases in the matrix and water starts invading the system from the sides, making its way deeper into the matrix. As water saturation increases at the matrix faces, its relative permeability increases and water movement into the matrix becomes easier. Water imbibition into the shale matrix is responsible for the pressure increase observed at later times of simulation (dimensionless time = 10^7) as also observed in Figure 2.6.

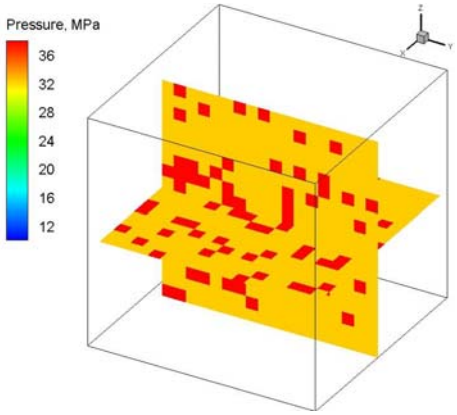

(a) dimensionless t = 1

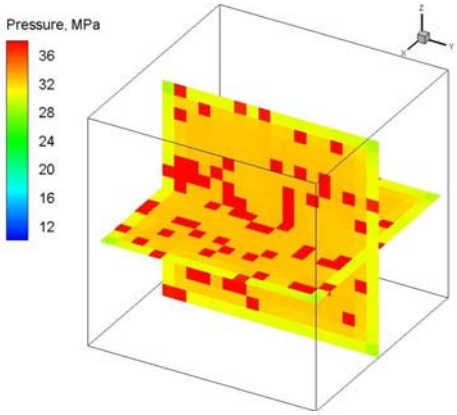

(b) dimensionless t = 10^2

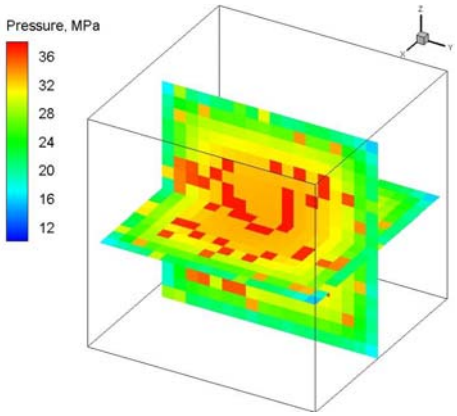

(c) dimensionless t = 10^3

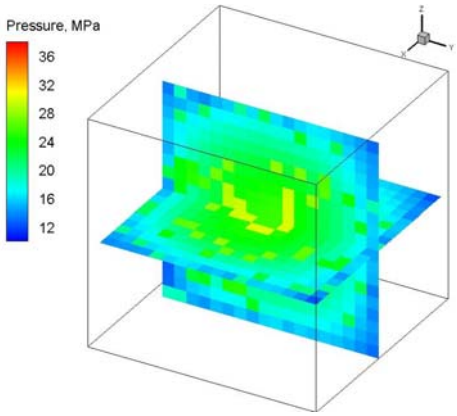

(d) dimensionless t = 10^5

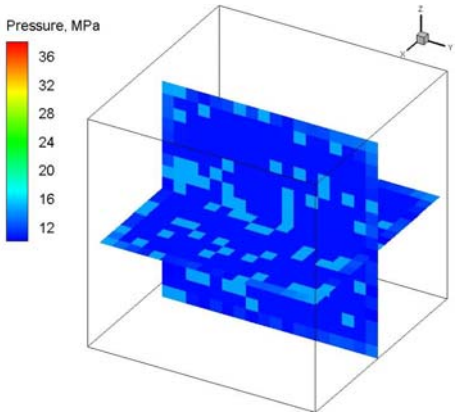

(e) dimensionless t = 10^6

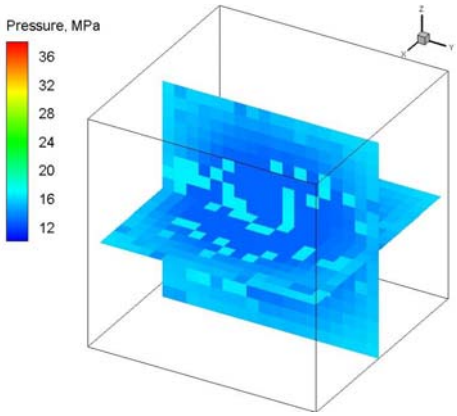

(f) dimensionless t = 10^7

Figure 2.11: This figure shows the pressure distribution in the matrix with time. As evident, pressure starts decreasing as production starts from the fracture network. The red blocks in the first picture show kerogen and the rest are inorganic grid blocks.

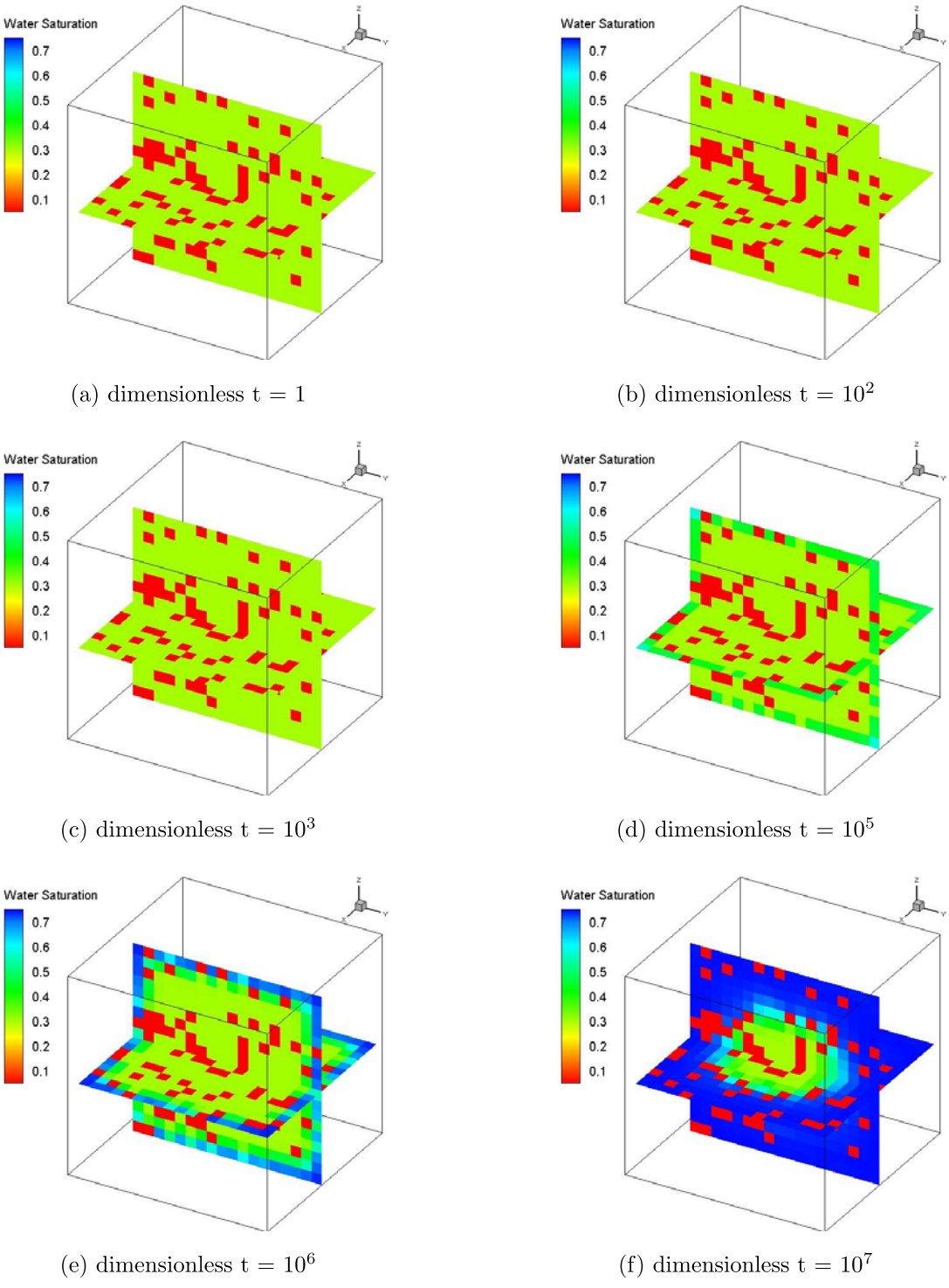

(a) dimensionless t = 1

(b) dimensionless t = 10^2

(c) dimensionless t = 10^3

(d) dimensionless t = 10^5

(e) dimensionless t = 10^6

(f) dimensionless t = 10^7

Figure 2.12: Water saturation distribution in the shale matrix is depicted at different times in this picture (water imbibition scenario). Despite pressure depletion, water imbibition into the system starts well after hydrocarbon production has begun (in the first two plots red grid blocks represent the kerogen and the remaining blocks are inorganic).

Now, consider the second production scenario in which, fracture is filled with the produced oil and gas with no water to imbibe into the matrix. Similar to the previous case, pressure in inorganic and kerogen media decreases as we start producing hydrocarbon from the matrix (Figure 2.13). In this case, oil and gas expansion will replace water imbibition as the drive mechanism. Despite what is observed in Figure 2.6, pressure becomes steady at the late production time and no pressure build up is observed (Figure 2.13). Looking at average water saturation values over time (Figure 2.14), one can see its value stays constant in both inorganic and kerogen medium. Water wet inorganic tends to hold water in it while there is no other source of water to imbibe into this medium. On the other hand, water saturation in kerogen is below its critical saturation, and the trapped water in kerogen is considered to be immobile.

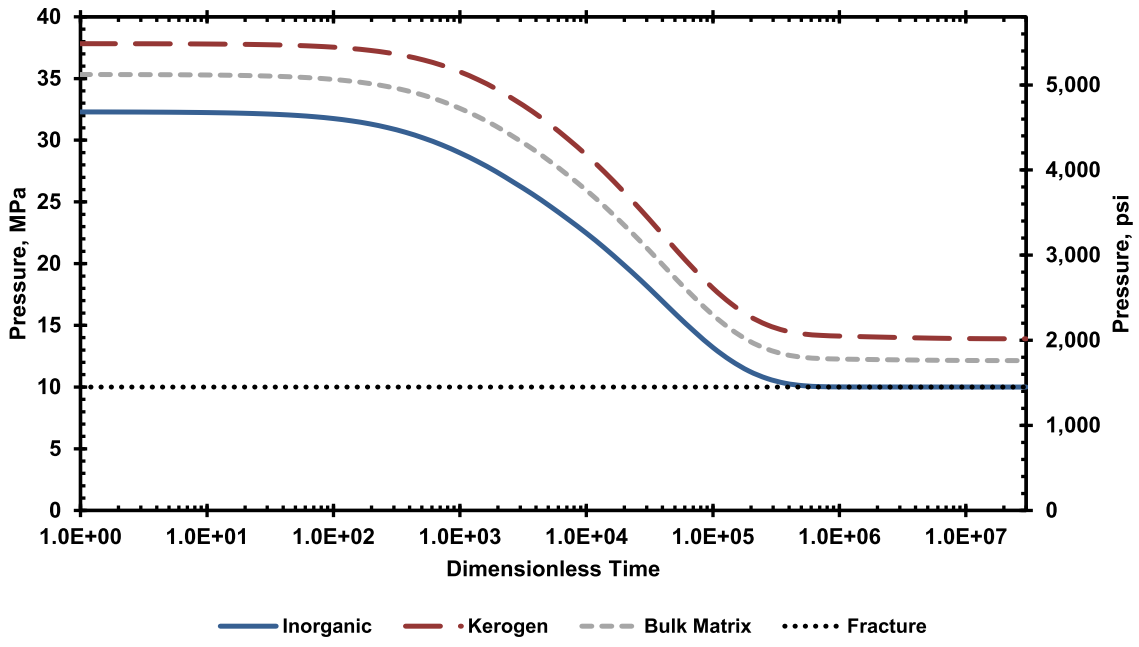

Figure 2.13: Matrix pressure (kerogen and inorganic matter) decreases steadily with time as we continue producing from the shale matrix for the cases where no water is in the fracture. The main drive mechanism in this scenario is oil and gas expansion.

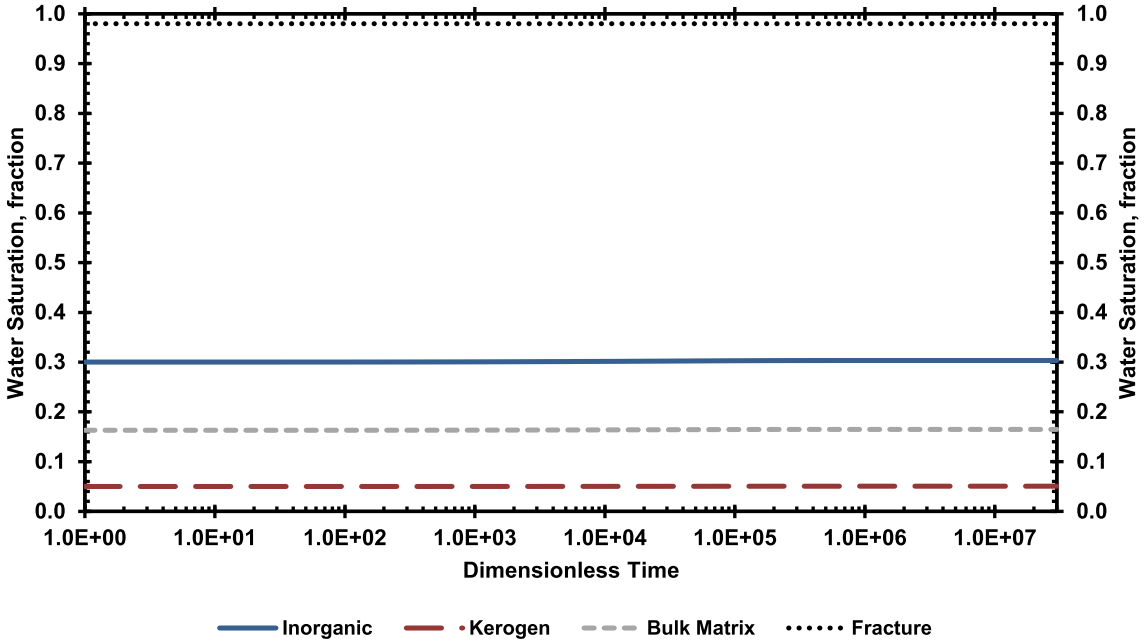

Figure 2.14: Water saturation in the inorganic and kerogen stays constant for cases where fracture is filled with hydrocarbon.

Average oil saturation for the water imbibition case (Figure 2.8) and oil/gas expansion case (Figure 2.15) show similar values over production time. On the other hand, contrary to the water imbibition case, gas saturation in the inorganic increases due to pressure depletion and gas expansion when fracture contains only hydrocarbon (compare solid lines in Figure 2.9 and Figure 2.16).

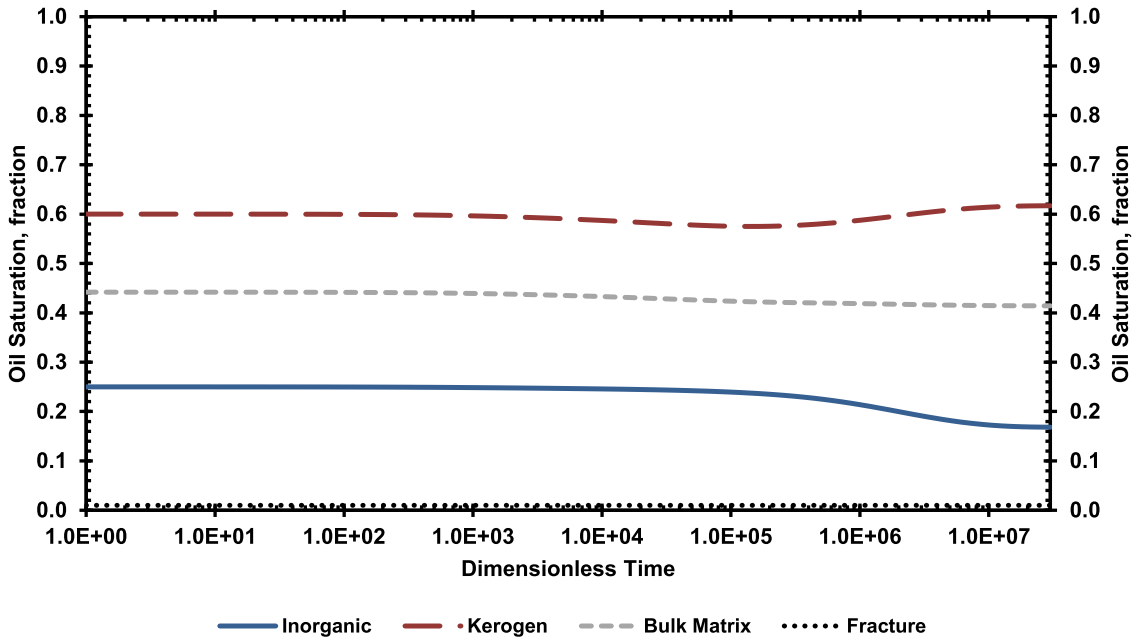

Figure 2.15: Oil saturation in kerogen stays almost constant, while its saturation in inorganic decreases and gas will replace oil in that media.

Comparing gas recoveries for two discussed production scenarios (Figure 2.10 and Figure 2.17), we will see gas production only decreases slightly when there is no water imbibition into the system. This is important because water imbibition occurs only in the inorganic mater and the final gas saturation (in inorganic) is approximately six times higher when the fracture is filled with hydrocarbon, compared to the water imbibition case (53% versus 9%) and this only decreases gas recovery 5% for the former case. In other words, the comparison between these cases show that most of gas production is coming from kerogen, indicating the significant share of hydrocarbon-rich kerogen in gas production. Oil recovery for both cases is small.

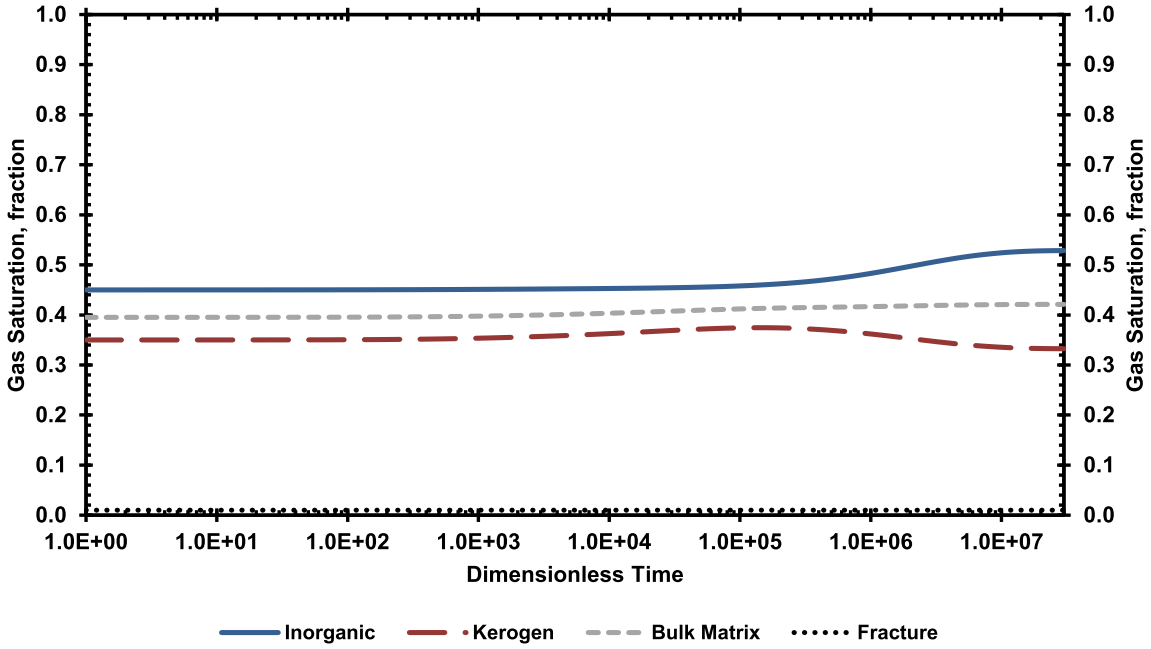

Figure 2.16: With further pressure depletion, gas comes out of solution and expands in the inorganic to compensate for oil production.

2.5.2 Alteration of producing gas–oil ratio in the near fracture regions

Liquid–rich shale producing wellstream is affected by factors such as very low permeabilities, localized large gas to oil mobility ratio gradients, substantial pressure drop near the fractures, and gas evolution in that region. Such behavior is analyzed in our paper by designing a case where the matrix is fully saturated with oil and water, and production starts from low–pressure fracture that is fully saturated with the produced oil and gas. Figure 2.18 shows the gas saturation map in the system, along with pressure distribution at dimensionless time of 5×10^4 after production starts. As pressure decreases from the sides, gas will evolve and its saturation increases in the region close to the fracture. Increasing mobility of the gas phase hinders oil production resulting in an increasing producing gas oil ratio over time (Figure 2.19).

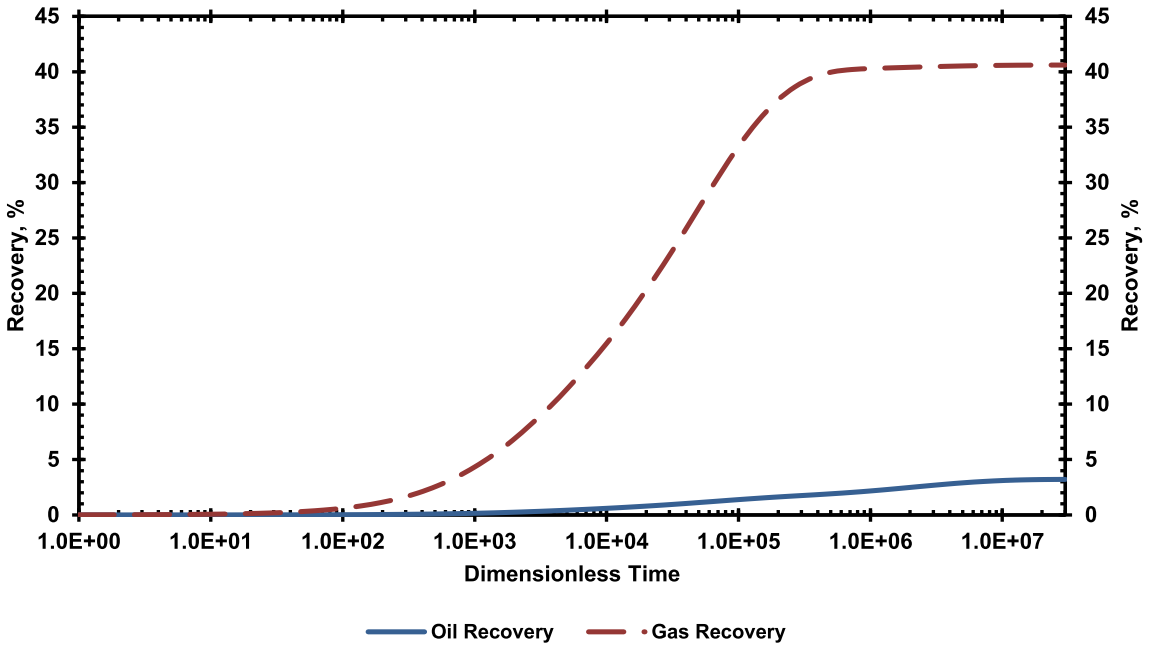

Figure 2.17: Gas recovery is slightly lower when no water imbibes into the matrix (compare it to Figure 2.10). Oil recovery is very low in such tight reservoirs.

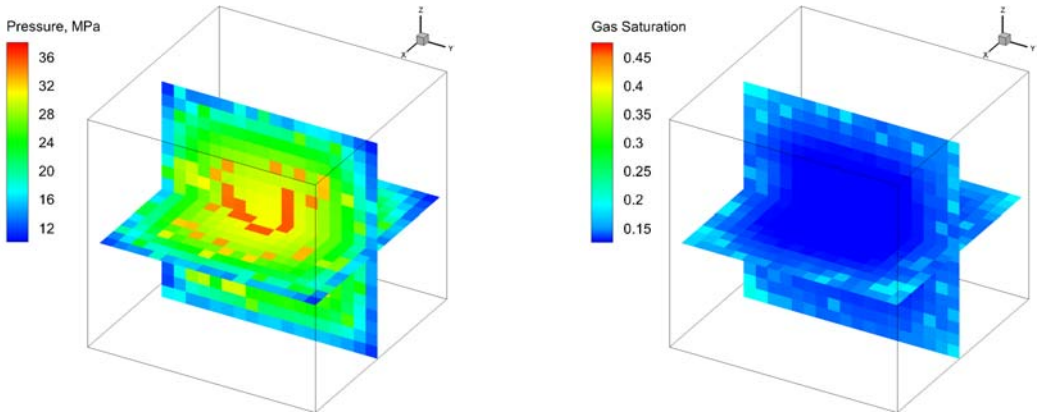

(a) Pressure distribution

(b) Gas saturation distribution

Figure 2.18: Pressure and gas saturation maps in the shale matrix (dimensionless time $= 5 \times 10^4$) show that gas saturation increases in the vicinity of fracture where pressure decreases considerably. Localized large gas–to–oil mobility ratio can considerably impact oil production in liquid–rich shale.

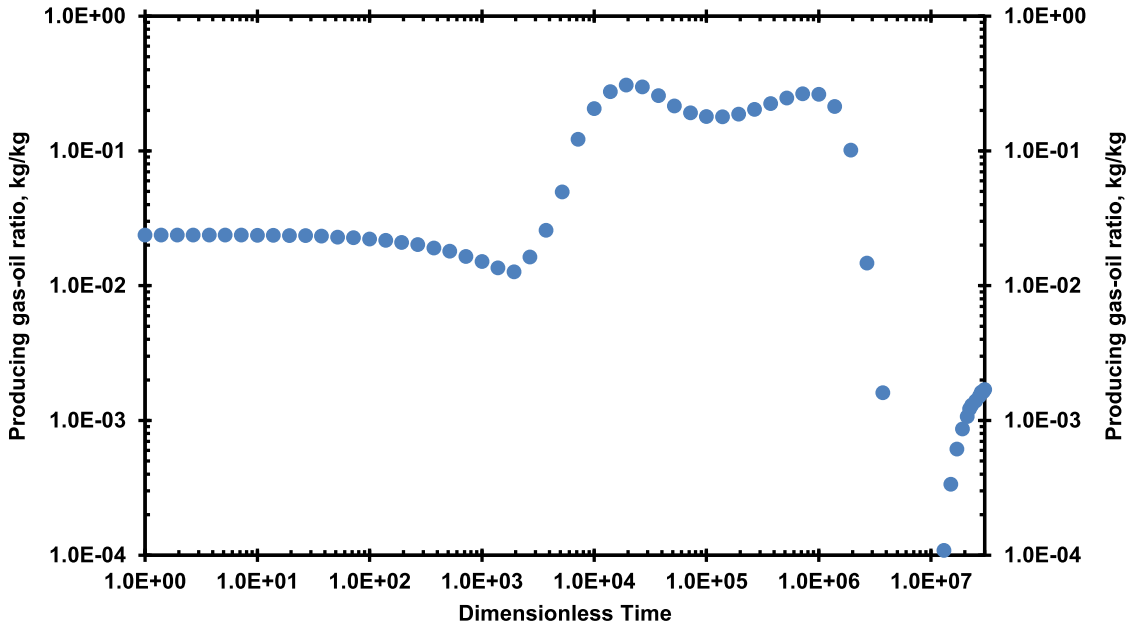

Figure 2.19: Producing gas–oil ratio increases as pressure in the near fracture region drops (starting at dimensionless time of 10^3) and gas comes out of solution.

Figure 2.20 shows gas saturation in the matrix with production time. As production continues, pressure decreases in the matrix and dissolved gas starts coming out of solution. This excessive gas is responsible for the increased producing gas–oil ratio in the matrix.

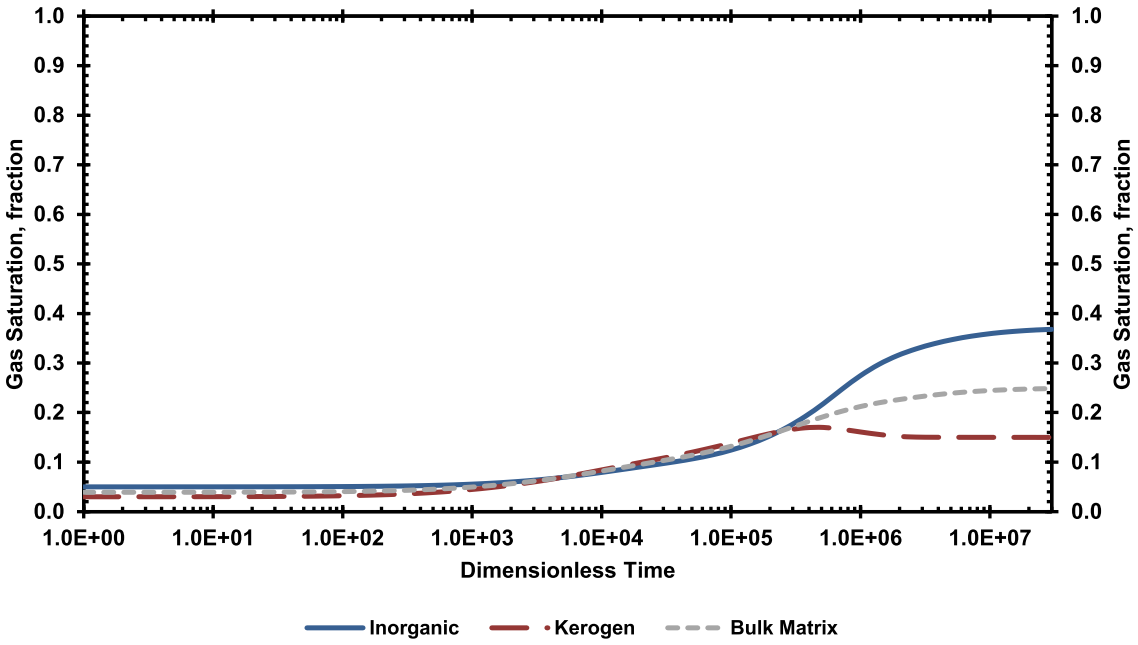

Figure 2.20: As production continues, pressure decreases in the matrix and dissolved gas starts coming out of solution. This excessive gas is responsible for the increased producing gas–oil ratio in the matrix.

2.5.3 Effect of TOC on hydrocarbon production

As mentioned earlier, TOC is a measure of the organic–richness of the shale. Productive shale plays have, in general, higher TOC values. TOC values in our model are reflected in the number of kerogen grid blocks. To see how TOC can affect flow dynamics in shale, we have sensitized its influence on hydrocarbon production by using three different TOC values of 6%, 9.5% (reference case discussed earlier), and 13%. Results are analyzed in terms of average matrix pressure and total gas and oil production. In this section, rather than being worried about the actual meaning of recovery factor (hydrocarbon produced divided by hydrocarbon in place for each case), we are interested in comparing the cumulative hydrocarbon production in each sensitivity case. This is achieved by using the concept of "normalized cumulative pro-

duction," which is calculated by normalizing the cumulative hydrocarbon production in each case to a constant total hydrocarbon in place (calculated from the reference case). A higher "normalized cumulative production" simply means higher amounts of produced hydrocarbon and normalizing all values to a constant number (hydrocarbon in place of the reference case) instead of reporting the actual productions makes the production values more readable and comparable to each other. Figure 2.21 shows average shale matrix pressure for cases with different TOC values follow a similar trend without any noticeable difference.

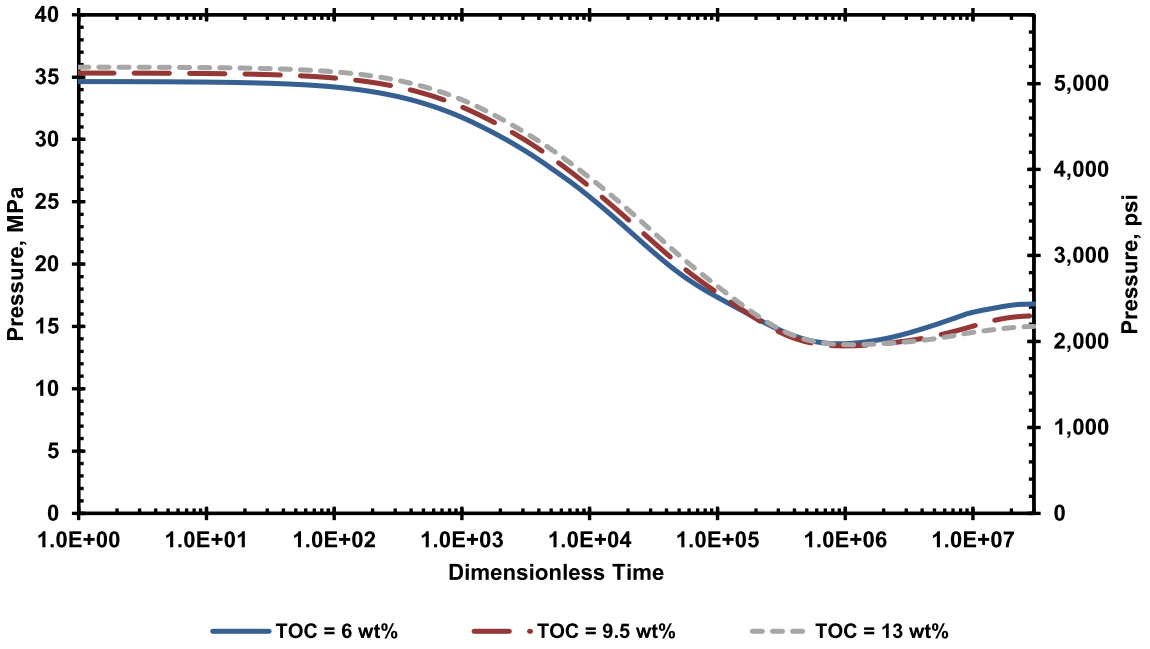

Figure 2.21: Average pressure in shale matrix follows a similar trend for higher and lower TOC values.

Cumulative gas production increases for higher TOC cases (Figure 2.22). As TOC increases in shale, the number of kerogen grid blocks increases in the system. High porosity kerogen can store considerable amounts of hydrocarbon. Compared

to the liquid phase, gas phase flow in shale is more efficient when considering its lower viscosity and improved permeability due to molecular slippage. Because of these reasons, higher TOC cases produce more gas. On the other hand, oil flow in the shale matrix has been restricted by its ultra–low permeability, and according to Figure 2.23, TOC values do not alter oil production substantially, even though oil in place increases with TOC.

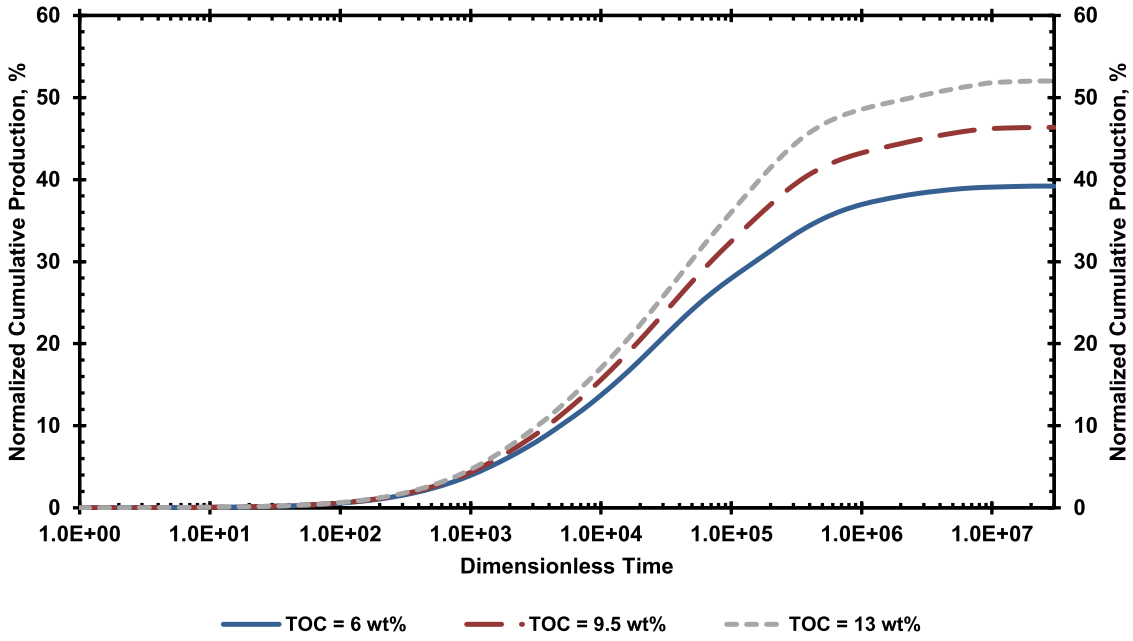

Figure 2.22: Higher TOC values increase total gas production from the shale matrix.

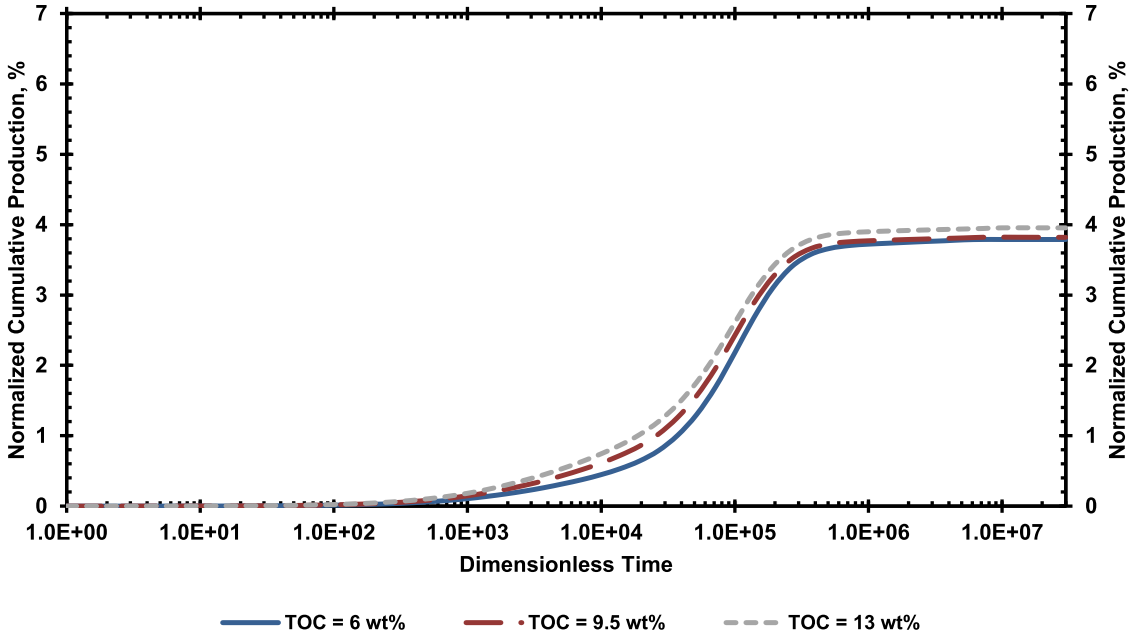

Figure 2.23: Total oil production from the shale matrix does not increase with higher TOC values due to the restricted oil flow in low permeability shale.

2.6 Conclusions

In this chapter, we proposed a micrometer scale model with a shale subdivision scheme to simulate three phase oil, gas, and water flow in liquid–rich shale. Porous media in shale is divided into three main parts: inorganic matter, kerogen (these two sub–systems form the shale matrix), and fracture network (hydraulic or natural fracture). Each of these subsystems has its own hydraulic, wettability, transport, and storage characteristics. Capillary pressure and relative permeability effects are explicitly accounted for in our model by employing appropriate functions specifically presented for shale reservoirs. On one hand, inorganic matter is considered to be water–wet with a relatively low porosity and high capillary pressure. Having a designated inorganic sub–block mainly contributes to the ability of better modeling dynamic water behavior in the system. On the other hand, oil–wet kerogen has a

higher porosity compared to the inorganic matter and can be a rich source of hydrocarbon. Our simulation results show that although total gas production increases as TOC increases in the shale matrix, oil flow does not change considerably because it is significantly influenced by low permeability of shale matrix and relatively high capillary pressure in kerogen. Due to a very small mean pore size in shale reservoirs, capillary pressure can have quite significant effects on flow dynamics of such reservoirs. This indicates the necessity of employing solid experimental techniques to comprehensively investigate capillarities in shale reservoirs. Additionally, our results show that producing gas–oil ratio increases with hydrocarbon production from liquid–rich shale, because of gas evolution near low–pressure fractures. Higher gas mobility in such regions will significantly influence oil production.

3. SIEVING EFFECT AND SIZE FILTRATION[†]

3.1 Introduction

Shale reservoirs are known as rocks with a very low permeability that are noticeable sources of hydrocarbon storage. Low permeability of such reservoirs is attributed to the fact that the average pore size in such reservoirs is considerably lower than the conventional sandstone reservoir rocks [43] in which high permeabilities provide a passage to hydrocarbon flow into the well without any significant stimulation scheme. Wang and Reed [44] investigated the presence, and importance, of different porosity systems in shale resources. They categorized the pores into micro– and nano–pore based on their size. According to authors, organic matter in shale acts as a nano–filter to hydrocarbon flow, meaning that it causes the flow in this system to be predominately single–phase hydrocarbon without residual water. Presence of different pore types in shale was also reported by Curtis et al. [4, 5], where they used analytical tools to further investigate the microstructure of shales.

Comparing these pore sizes with the molecular size of different hydrocarbons (0.3 to 1 nm), one can argue that different size pores can behave selectively when exposed to molecules of various sizes. While larger pores can accommodate any size hydrocarbon molecules, smaller pores will impose certain stereo–related restrictions, limiting the size of hydrocarbons that can be stored in such spaces. This can be seen as a so–called "sieving effect" where hydrocarbon distribution, driving forces, and thermodynamic properties can vary based on the pore size. Bjørlykke [45] has indicated occurrence of hydrocarbon size exclusion in shale reservoirs. The fact that

[†]Reprinted with permission from "Pore Size Variability and Sieving Effect in Liquid Shale–A Multiple Permeability Approach and Eagle Ford Case Study" by M. Alfi, C. An, Y. Cao, B. Yan, M. Barrufet, J. Killough. Paper presented at SPE Reservoir Simulation Conference (RSC2017). Copyright 2017 by SPE. Further reproduction prohibited without permission.

source oil contains more aromatics (larger species) compared to reservoir oil can be interpreted as the consequence of size filtration [46, 47]. In other words, one can suggest that oil (with larger molecules compared to the gas phase) is mostly stored in larger pores in the shale rock. Using statistical inferences, Wang et al. [48] have concluded that oil molecules can be stored in pores with pore diameters larger than 40 nm. The number presented by authors is not definitive and should not be taken as granted as there are some other factors (e.g. viscosity, temperature, and pressure) that play a role in this size–dependent oil storage. Similar conclusions were drawn by Zhang et al. [49, 50] while analyzing the shale samples from liquid–rich Eagle Ford and Bakken formations. Pore size distribution analysis, before and after using solvent to extract hydrocarbon in pores, suggested that oil will be mostly stored in pores with a size larger than 20 nm. Zou et al. [51] has simulated oil storability in pores with different diameters. The results show that oil storage and migration are determined by both surface free energy and the size of space. According to the authors, oil does not penetrate pore throats smaller than 20 nm. This is the lowest threshold that will allow oil to flow. They reported no chemical or physical limitation to oil to penetrate in pores larger than 200 nm. Rylander et al. [23] used the results of logs and core NMR to analyze fluid distribution in shale rocks. According to their results, oil is predominately produced from larger pores with diameters of 250 nm or more. The 250 nm pore diameter presented by the authors looks to be far larger than the upper limit of the molecular size of hydrocarbons routinely found in oil for any space hindrance to occur and in fact may overestimate the threshold pore size to see size filtration.

Based on these observations we propose a new model to consider variability in pore size of the shale reservoirs. This is achieved by dividing the porous media into two different sub–media (large pores and small pores) that are assumed to be in ther-

modynamic equilibrium with each other. The current model provides a powerful tool to interpret the unexpected and harder–to–explain production behavior—compared to the conventional resources—in shale by dividing the pores into different sizes and characteristics.

To the best of author's knowledge, this work is among the pioneers in analyzing size filtration, or better called sieving phenomenon in tight shale. In an effort to model a similar thermodynamics system, Geren et al. [52] and Zhu et al. [51] analyzed membrane effect in shale reservoirs. Their results are alongside with what we have found in this paper. However, the authors assumed that the principle of equal chemical potentials is not true for the large hydrocarbon molecules in small shale pores because of the membrane effect, which is a questionable assumption, as it does not yield a minimum Gibbs energy at the state of equilibrium.

3.2 Pore size distribution

Studies on architecture and structure of pores in shale show that the pore size in shale spans a range as low as a few nanometers up to hundreds of micrometers. Firouzi et al. [53] performed NMR and nitrogen desorption experiments, along with molecular modeling of the pore network to analyze pores of different synthetic and real field samples (Eagle Ford shale). The average pore size in Eagle Ford samples was reported to be around 10 nm. Farhadi Nia et al. [54] attributed one–third of the porosity in oil–rich Monterey shale to pores with sizes smaller than 45 nm. Analysis of pore size distribution in some of the North American shales through combining mercury porosimetry and low–pressure gas adsorption shows a significant pore volume between diameters 3-50 nm and lower than 2 nm [55, 56]. A similar conclusion has been drawn by Clarkson et al. [57] in which they reported a bimodal distribution of pores in tight formations with peaks at diameters less than 10 nm and

around 100 nm. Such a bimodality (with one of the modes revolving around 10 nm diameter) in shale pore size is also reported by Bustin et al. [58] and Hu et al. [59]. Alongside with what has been mentioned so far, mercury injection test in Barnett shale showed a non–uniform distribution of the pore throat size. For some other samples, the pore size was in the range of 2–8 nm [6]. Sondergeld et al. [6] considered a significant contribution to the total porosity for such small pores. A median pore size of 100 nm with the range from 5 nm to 800 nm was reported in Barnnet [9]. Lu et al. [17] used mercury injection porosimetry and scanning electron microscopy (SEM) to evaluate the pore structure of the middle Tuscaloosa mudstone at the Cranfield site, Mississippi. The results showed a bi–modal distribution of pores with modes at 8 and 20 nm with the pore size spanning hundreds of nanometers. Kuila and Prasad [60] experimented pore structure and pore size distribution in pure clay minerals and natural shales. According to the authors, mineralogy has a considerable impact on pore size and structure of clay and shales. Their results have revealed a multiscale pore structure in low permeability media. Nitrogen adsorption experiments on clay samples showed both unimodal and bimodal pore size distribution (peaks at 3 nm and 100 nm). Mercury injection experiments also reported bimodal pore distributions in clays with modes larger than what has been observed from adsorption tests. The authors claim three different multiscale structures of clays: fine mesopores (3 nm), large mesopores (20-25 nm) and larger micron size pores (2000 nm). Shale samples also exhibited different pore structure and size, either unimodal or bimodal (with a considerable variability in pore sizes), based on mineralogy. Such a multiscale nature of pore sizes in shale and the necessity to account for this feature is stressed out by other authors as well [16, 58, 60, 61, 62, 63, 64, 65, 66].

To be more specific, let us look at pore size distribution (Figure 3.1) of two samples acquired from Devonian Mississippian organic–rich Muskwa and Besa River

formations [67] and the Cretaceous Shaftesbury formation [63]. Pore size distribution in these samples show that pores as small as a few nanometer and as large as hundreds of micrometers can be found in shale samples. It is also important to notice that the pore volume is a mix of all these pores where neglecting any pore type (either very larger pores or very small ones) can result in missing a significant portion of the pore volume. While certain features and equations appear to be valid when used for pores of larger diameters, treating small pores with the same scale will create erroneous calculations in that media.

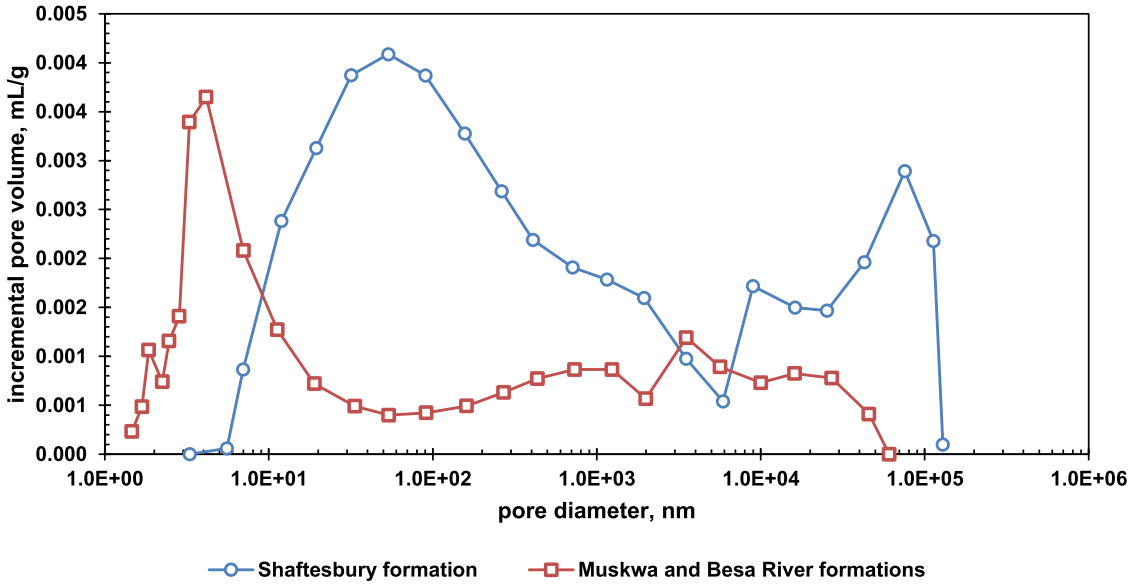

Figure 3.1: Pore size distribution in two different shale samples show that a broad range of pore sizes can be found in shale reservoirs. The sample from Muskwa and Besa Rive formations have pores with diameters as low as 1 nm, up to 100 µm which is five orders of magnitude larger (reprinted from Chalmers et al. [63] and Ross and Bustin [67]).

3.3 What is size filtration or sieving?

As mentioned in the previous section, the pore size in shale reservoirs spans a wide range. Built upon those evidences, this study divides pores in the shale matrix into two categories of large and small pores. Pores with a large diameter behave as expected. Their phase behavior is similar to the bulk phase behavior where the conventional phase behavior models (e.g. Peng–Robinson) are still valid in such media. However, for pore diameters as low as a few nanometers, it is conceivable that the molecular size of hydrocarbons in oil becomes comparable to that of the pore diameter. Paraffinic hydrocarbons can have a diameter approaching 1 nm while the size of hydrocarbons containing multiple rings in their structure can exceed 2–3 nm [43, 68, 69]. The tight porous media in such situations can act as a semi–permeable membrane that selectively filters molecules based on their sizes. This creates a compositional gradient between large and small pores because of steric hindrance. Figure 3.2 represents a schematic of the size filtration process proposed by this study. As explained before, large matrix pores (with no space restriction) are capable to accommodate more of the heavier hydrocarbons, which can later be translated into more liquid hydrocarbon at surface conditions; as opposed to the fluid composition in small pores (space restriction is observed) with a higher concentration of lighter species.

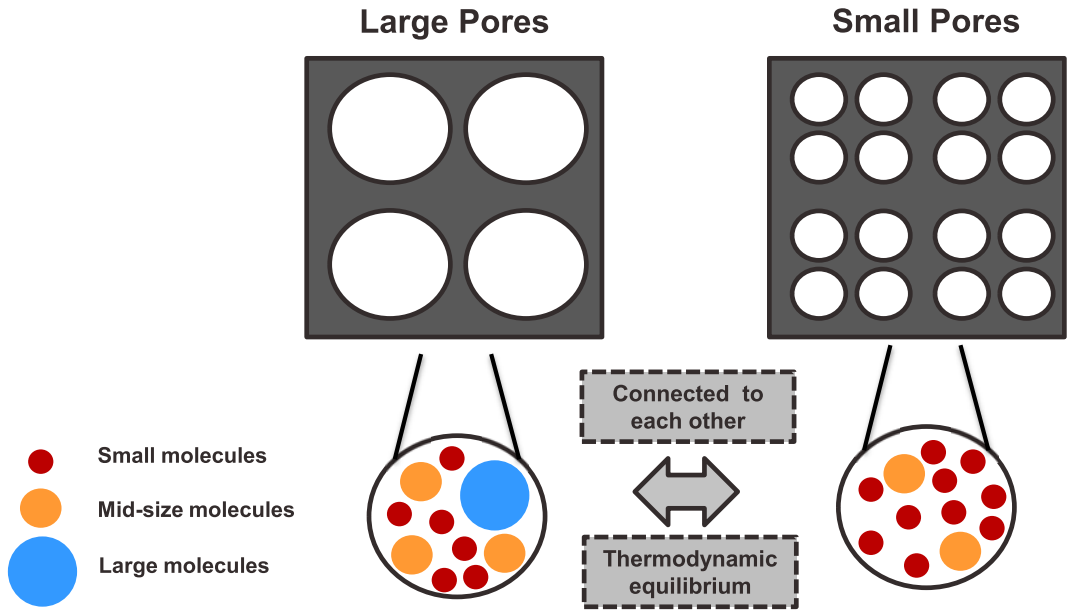

Figure 3.2: Schematic of the proposed size filtration effect in which larger hydrocarbon molecules are excluded from small pores. As a result, the fluid composition in the larger pores exhibits a heavier nature, compared to that of smaller pores.

The above–mentioned phenomenon has been investigated in a number of separate studies. Sundstrom and Krautz [70] investigated the equilibrium interaction of normal paraffins (in liquid phase) on molecular sieves. For their experiments, they used type 5A molecular sieves to determine the effect of temperature, molecular size, and concentration on equilibrium concentration of alkanes by considering different binary mixtures of heptane (C_7H_{16}), decane ($C_{10}H_{22}$), dodecane ($C_{12}H_{26}$), and tetradecane ($C_{14}H_{30}$). Their results show that alkanes with a lower molecular weight can preferentially enter the smaller size pores. Selectivity for lower molecular weight paraffins is determined mainly by steric factors in which smaller species satisfy the steric requirement to enter the small pores. Figure 3.3 shows the data reported by Sundstrom and Krautz [70] for two binary mixtures of heptane–decane

and heptane–tetradecane. The x–axis shows the fraction of heptane (smaller fluid molecule in the binary systems) in the bulk phase or in large pores. The y–axis shows that of heptane in the small pores (sieved composition). If there is no space hindrance, all data points should fall on the dashed line that shows the concentration of heptane in large and small pores is equal. However, experimental results show that concentration of heptane (smaller hydrocarbon species) is higher in the small pores (all points are located above the equal concentration line). This demonstrates the size filtration effect in small pores. In addition to that, it is obvious from the graph that the deviation of heptane concentration in small pores from that of large pores is more pronounced in the heptane–tetradecane binary system, compared to the heptane–decane system. This behavior is attributed to the larger molecular diameter of tetradecane, compared to decane, which makes the filtration phenomenon more severe. Studies by Alkandary et al. [71], Berenguer–Murcia et al. [72], Breck [73], Dunne and Manos [74] proposed a similar behavior in small pores. Being able to model such phenomenon requires a good understanding of molecule–wall interactions in small pores. The following section discusses the thermodynamics of size filtration in small and large shale pores.

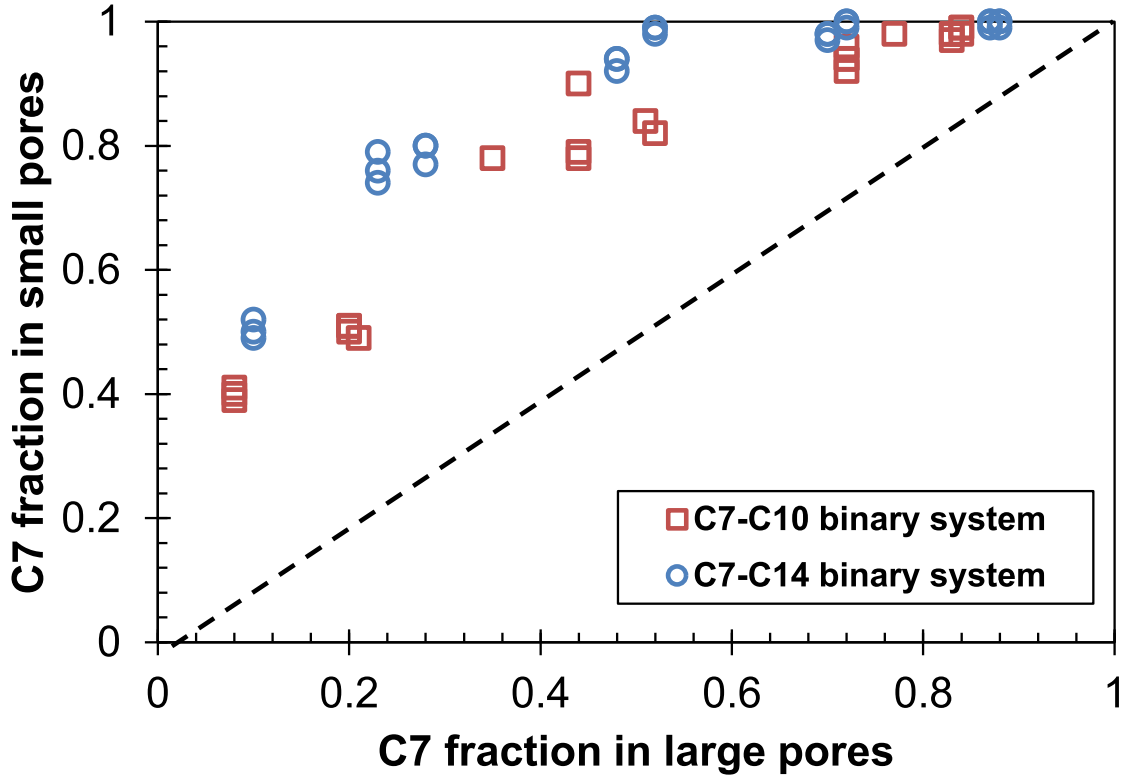

Figure 3.3: Hydrocarbon distribution in large and small pores for binary mixtures of heptane–decane and heptane–tetradecane. The dashed line shows situations where no sieving takes place and the composition of small and large pores are the same. 5A molecular sieve (pore opening is equal to 0.5 nm) was used for these experiments (reprinted from Sundstorm and Krautz [70]). The results show a clear filtration effect for larger–size molecules.

3.4 Thermodynamics of sieving

In this section, we provide detailed information about the thermodynamics of size filtration. It includes a discussion on the appropriate equation of state to be used in this process, along with model calibration and equilibrium calculation. Intermolecular interactions and interactions between fluid and wall molecules are believed to alter fluid properties in small pores of shale reservoirs. There has been a tremendous effort recently to understand such behavior either through experiments [75, 76, 77, 78, 79],

vapor–liquid equilibrium calculations [80, 81, 82, 83, 84, 85, 86], or more computationally expensive molecular simulations [87, 24, 25, 88]. Thermodynamics behavior of the fluid in small pores is modeled in this paper using the approach presented by Travalloni et al. [89, 90]. Travalloni et al. [90] extended the commonly used Peng–Robinson equation of state (Peng and Robinson [37]) to model the fluid behavior in confined media. Confinement effects are explicitly included in their analytical equation of state to calculate global fluid properties by adding an additional term to the original Peng–Robinson model to incorporate fluid–wall interactions. This feature makes the proposed equation of state a generic type of equation that can be used to calculate properties of both bulk state and confined fluid (by using appropriate parameters). The equation of state is derived assuming that each pore has a cylindrical shape with a continuous and homogeneous surface. Fluid molecules are assumed spherical. Fluid wall interactions are accounted for using square–well potentials with a pairwise additivity for the attractive potentials. An important part of the equation of state refers to the repulsive forces as those forces play a tremendous role in situations where molecular sizes are comparable to that of the pore diameter (such cases are of specific interest in this paper). The packing order of hard spheres in cylinders is used in the current equation of state to account for the repulsive forces and steric hindrance. Size filtration effects in this study is modeled using Equation 3.1 [90]:

$$P = \frac{\mathrm{R}T}{v - b_\mathrm{p}} - \frac{a_\mathrm{p}(T)}{v(v + b_\mathrm{p}) + b_\mathrm{p}(v - b_\mathrm{p})} - \theta \frac{b_\mathrm{p}}{v^2} \left(1 - \frac{b_\mathrm{p}}{v}\right)^{\theta - 1} (1 - F_\mathrm{pr}) \left(\mathrm{R}T \left(1 - \exp\left(-\frac{\mathrm{N_{av}}\epsilon_\mathrm{p}}{\mathrm{R}T}\right)\right) - \mathrm{N_{av}}\epsilon_\mathrm{p}\right) \quad (3.1)$$

where P is pressure, v is molar volume, T is temperature, a_p and b_p are the Peng–Robinson related parameters modified for pore–fluid interactions (subscript "p" de-

notes that specific parameter is modified for the pore effects), F_{pr} and θ are geometric functions for the confined fluids, and $\mathrm{N_{av}}$ is the Avogadro number. A complete explanation of Equation 3.1 with an accurate statement of the variables is presented elsewhere [90]. In addition to the pore diameter and regular fluid–related parameters like critical pressure, critical temperature, and acentric factor, finding pressure, volume, and temperature from Equation 3.1 requires two parameters (ϵ_{p}, δ_{p}) that are related to the fluid molecules and also the nature of the interaction between the fluid and pore surface. ϵ_{p} appears directly in the formula but δ_{p} is embedded into the other terms of the equation of state. ϵ_{p} accounts for the energy parameter of the attractive interactions between a fluid molecule and the pore wall and δ_{p} is the range parameter of the attractive forces between fluid molecules and pore. δ_{p} is the distance from pore walls at which hydrocarbon molecules are impacted by attractive forces from the pore wall. Given the fact that the average pore radius in the porous media (r) is known, energy and range parameters can be found for each fluid molecule at a given porous media by fitting the model–predicted properties to that of real experiments. Note that for cases where $r \to \infty$ (very large pore diameters or bulk phase), the value of the third term in the right hand side of Equation 3.1 goes to zero and $a_{\mathrm{p}}(T)$ and b_{p} become equal to $a(T)$ and b from the original Peng–Robinson equation of state, causing the pressure from Equation 3.1 to be equal to the one predicted by the Peng–Robinson equation of state.

To model the sieving process and quantify composition variation between large and small pores, we define a system composed of two different pore types that are connected to each other (Figure 3.4). These two porosity types are assumed to be in thermodynamics equilibrium with each other while temperature is the same. Given a composition in the larger pore, the composition distribution in the small pores will be calculated where size filtration and space hindrance will take place. Thermodynamics

equilibrium between these two media demands every individual component in large and small pores to have equal fugacities (Equation 3.2).

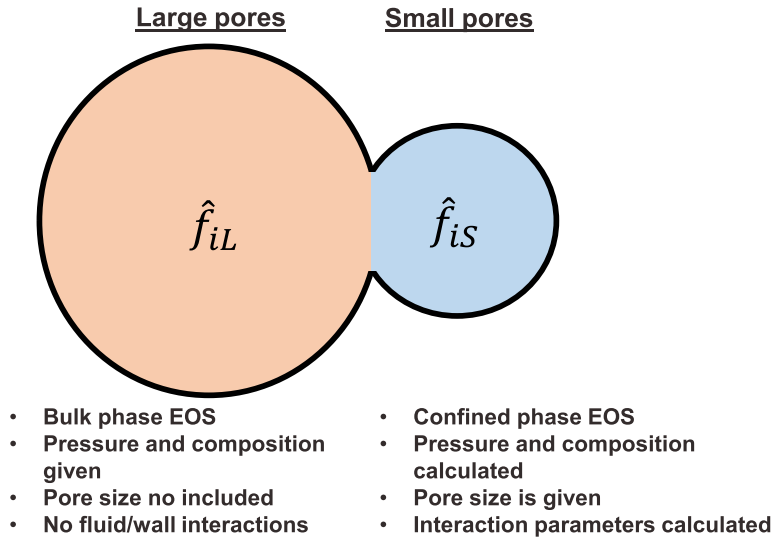

Figure 3.4: Large and small pores are considered to be in thermodynamic equilibrium, which means equality of fugacities of individual components through the system. Pressure and composition of the large pores are given in our calculations and those of the small pores will be calculated accordingly. $\hat{f}_i$ in this picture represents the fugacity of component i.

$$\hat{f}_{i\mathrm{L}} = \hat{f}_{i\mathrm{S}} \tag{3.2}$$

In Equation 3.2, $\hat{f}_i$ represents the fugacity of the component i and subscripts L and S denote large and small pores.

Equation 3.2 can be further simplified by introducing the fugacity coefficients (Equation 3.3). In this equation, the natural logarithm of two sides are equalized:

$$\ln(x_{i\mathrm{L}}\hat{\phi}_{i\mathrm{L}}P_{\mathrm{L}}) = \ln(x_{i\mathrm{S}}\hat{\phi}_{i\mathrm{S}}P_{\mathrm{S}}) \tag{3.3}$$

where $x_{i\mathrm{L}}$ and $x_{i\mathrm{S}}$ denote the mole fraction of the component i, in the large and small pores, $\hat{\phi}_{i\mathrm{L}}$ and $\hat{\phi}_{i\mathrm{S}}$ are fugacity coefficient of the component i, and P_{L} and P_{S} are pressures at large and small pores, respectively. The value of $\ln\hat{\phi}_i$ for each media can be calculated from Equation 3.4 and by using the appropriate fluid–wall interaction parameters in the equation of state.

$$\ln\hat{\phi}_i = \frac{1}{\mathrm{R}T}\int_v^{\infty}\left(\frac{\partial P}{\partial n_i} - \frac{\mathrm{R}T}{v}\right)dv - \mathrm{R}T\ln(z) \tag{3.4}$$

In Equation 3.4, z represents the compressibility value. Equilibrium calculations are performed by assuming a given pressure P_{L} and composition $x_{i\mathrm{L}}$ in the large pores and calculating the pressure and composition distribution in small pores, by solving Equation 3.3 for all components. This is to solve nc equations simultaneously and find P_{S} and $x_{i\mathrm{S}}$'s where $\sum_{i=1}^{\mathrm{nc}} x_{i\mathrm{S}} = 1$ (nc is the total number of components).

The equation of state introduced in the previous section (Equation 3.1) will be used in this study to calculate the fugacity coefficients of large and small pores in Equation 3.4, where the pore diameter in large pores is assumed to be a very large number. However, before being able to use the proposed equation of state, one should be able to properly calibrate the fluid–wall interaction parameters. Those parameters are not only related to the fluid molecules, but also depend on the type of the porous media and its composition. Relating these terms to common petroleum engineering terminologies, one can argue that the fluid-wall interactions depend on

geological and hydrological properties of the rock, as well as its wettability. The general nature of the problem we are trying to solve is very close to adsorption problems, in which an adsorbate will be adsorbed on the surface of an adsorbent, which can be a molecular sieve with a specific pore size. Hence, the experimental data on adsorption of hydrocarbons on different surfaces are good candidates to provide us with the required calibration data. There has been a considerable amount of experimental work on analyzing hydrocarbon adsorption on different surfaces [72, 91, 92, 93, 94, 95]. In all these experiments, the bulk hydrocarbon is in the vapor phase at a relatively low pressure. However, when we look at liquid shale reservoirs, we notice most of these resources like Eagle Ford can be located at very deep formations with initial pressures reaching 7000 to 8000 psi. In such a high–pressure environment, most of the reservoir fluid would be in the liquid phase. Indeed, it is very important to use the experimental data that better mimics the hydrocarbon phase condition encountered in liquid shale reservoirs. To be more specific, adsorption from the liquid phase on nanoporous media is associated with a high filling degree of the nanopores. Given the limited space in those pores, organization and packing of molecules in the pores can become the most dominant factor. Such conditions can result in specific selectivity effects, often completely different from the selectivity patterns observed in gas phase conditions. In this study, we will use the experimental data published by Gupta et al. [96] on liquid phase adsorption of hydrocarbons on molecular sieves to calibrate our equation of state model.

Gupta et al. [96] used n–pentane, n–hexane, n–heptane, and n–octane to investigate the effect of concentration on adsorption of liquid hydrocarbons upon LMS–5A zeolite molecular sieves. Experiments were performed at temperatures in the range of 6 to 42 °C (42 to 107 °F) and the results were reported as the amount of adsorbed hydrocarbon versus their concentration in the bulk phase for different temperatures.

Properties of the molecular sieve (e.g. specific pore volume) can be found elsewhere [97]. Experimental data from Gupta et al. [96] can be correlated to our model by converting the adsorption amounts to molar density of adsorbate that is equivalent to the molar density of hydrocarbon in the small pores. The concentration of hydrocarbon in the bulk phase in experiments is in fact equivalent to the hydrocarbon concentration in large pores of the current model. Figure 3.5 shows the molar density of hexane and octane in small pores as a function of their concentration in large pores, both for the experimental data and predicted data from the modified Peng–Robinson equation of state at 42 °C (107 °F). The regression parameters used in this study to match the experiment results were $\frac{\epsilon_{\mathrm{p},i}}{\mathrm{k}}$ (units in K) and $\frac{\delta_{\mathrm{p},i}}{\sigma_i}$ (unitless parameter) where $\epsilon_{\mathrm{p},i}$ and $\delta_{\mathrm{p},i}$ are introduced in previous sections (energy parameter and range parameter of the attractive forces between the fluid component i and pore), k is the Boltzmann constant, and σ_i is molecular diameter of the component i. According to Figure 3.5, the model–predicted densities exhibit an acceptable match with the experimental data. Table 3.1 shows the regression parameters (for hexane (C_6) and octane (C_8) on zeolite molecular sieve) that generate the best match with the experimental data. These values will be used in this study.

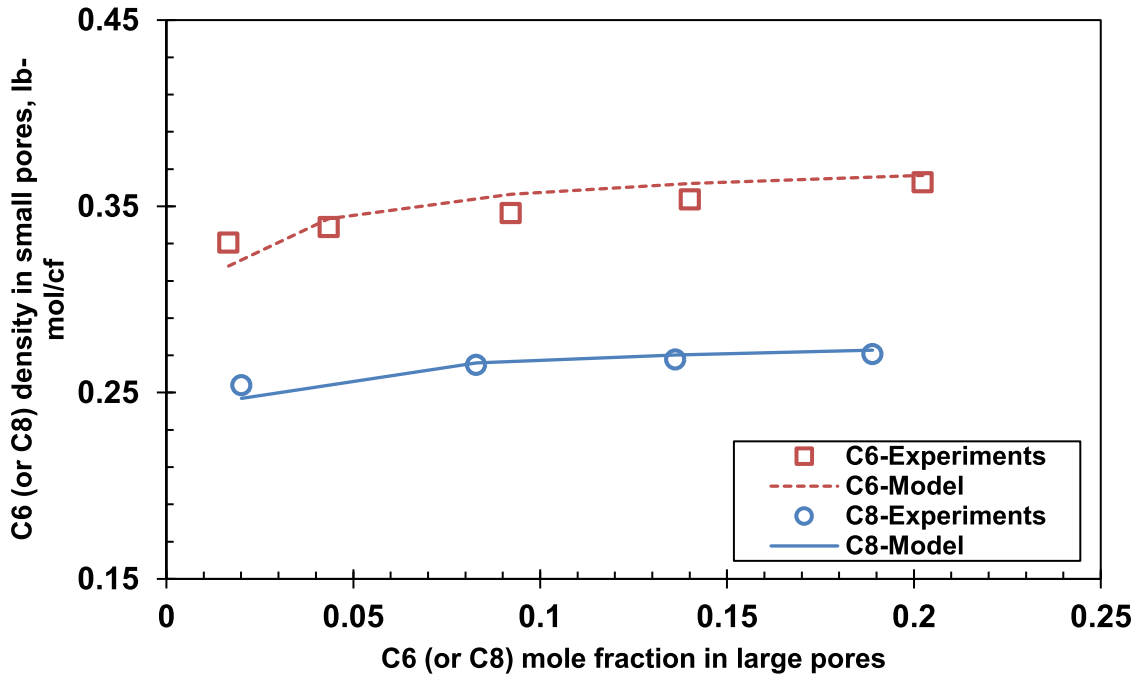

Figure 3.5: Density of hexane and octane in small pores versus hydrocarbon concentration in large pores from the experimental data (reprinted from Gupta et al. [96]) are used to calibrate the equation of state model. Adsorption experiments were performed for each hydrocarbon individually (no mixture) and benzene was used to dilute the samples and achieve different mole fractions in the large pores. The model–predicted density values show a good agreement with the experimental data. Data reported at 42 °C (107 °F) and atmospheric pressure.

Table 3.1: The regressed $\frac{\epsilon_{p,i}}{k}$ and $\frac{\delta_{p,i}}{\sigma_i}$ parameters (for C_6 and C_8 on zeolite molecular sieve) that generate the best match with the experimental data.

	$\frac{\epsilon_{p,i}}{k}$ (K)	$\frac{\delta_{p,i}}{\sigma_i}$ (unitless)
Hexane	2697	0.56
Octane	3102	0.46

3.5 Single– and multi–component sieving

In this section, we start by considering a case where pure octane (C_8) is included in large and small pores and try to evaluate the effect of different parameters on size exclusion of C_8 in small pores. For our purposes, the molar density of octane is used as an indication of how easy octane molecules can enter the small pores at different pore sizes. The larger the molar density of octane in small pores, the easier their movement into small pores would be (more efficient packing), which is interpreted as a weaker size exclusion. The molecular size of octane in this work is calculated to be 6.8 °A. All simulations were performed at 212 °F (100 °C, 373K) to resemble real reservoir conditions in liquid shale. Figure 3.6 shows the molar density of octane in small pores versus pressure for different pore diameters. As we can see, the density of octane in small pores goes down as pore diameter decreases (the dashed line in the graph shows octane molar density at large pores or bulk density of octane). Given the size of small pores, steric (or entropic) effects govern the thermodynamics behavior at relatively lower pore diameters. Entropic effects are often at least as important as energetic effects in the adsorption of molecules in confined environments. This is certainly true for adsorption in liquid phase, or at high pressures, where the organization and packing of molecules in the fully saturated pores becomes critical. In fact, the packing would be less efficient at smaller pore diameters and space hindrance will prevent molecules from entering the small pores.

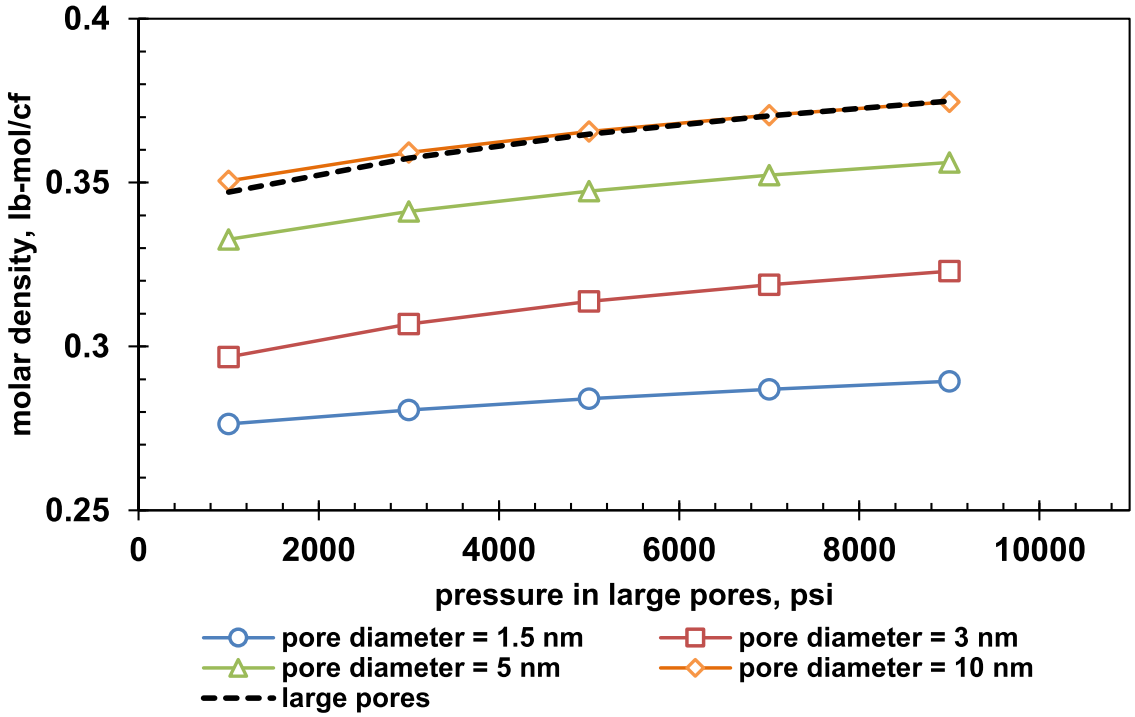

Figure 3.6: Comparison of the molar density of octane in small pores with various diameters. Pores with smaller diameters will impose a more pronounced steric hindrance, preventing the hydrocarbon molecules to enter small pores and resulting in a lower molar density for the same given bulk phase pressure. The dashed line shows the molar density of bulk octane in large pores. 3102K and 0.46 are used for $\frac{\epsilon_{\mathrm{p},i}}{\mathrm{k}}$ and $\frac{\delta_{\mathrm{p},i}}{\sigma_i}$ respectively (see Table 3.1).

It is important to note that the rock–fluid parameters are specific characteristics of hydrocarbon molecules and the porous media and can vary for different media. To see how rock–fluid interaction parameters can alter the equilibrium state, Figure 3.7 analyzes molar density of octane in small pores for different pore sizes at various fluid–wall affinities (high, medium, and low). As we can see, at low pore diameters (less than 6 nm for the case of octane), the entropic effect plays an important role in phase behavior of the confined octane molecules. Even when the rock–fluid affinity is very large, the molar density of octane in small pores is lower than that of large

pores or the bulk phase (dashed–line in Figure 3.7). As pore diameter grows, steric hindrance effects diminish while energetic effects start gaining more weight. Such a reversal in influential factors causes the molar density in small pores with a high rock–fluid affinity to be higher than that of the bulk phase. That is because strong attractive forces between the wall and fluid molecules draw more molecules into the confined media, as long as no steric restriction is felt by the molecules. We can see from the graph that the effect of steric restrictions on density is more pronounced than the energetic effects as density reduction in smaller pore diameters (less than 6 nm) is larger than the density increase in larger diameters (more than 6 nm). Based on our observations so far, three distinctive rock–fluid interaction regions can be recognized in tight media. When the pore size is smaller than a certain value (region I), entropic effects are the ones that determine the equilibrium in the system. Larger molecules are harder to enter a pore in this region. As pore radius becomes larger (region II), the steric hindrance effect will be replaced by energetic factors in which molecules with a higher rock–fluid affinity (typically molecules with a larger mass) would be preferentially adsorbed into the pores. For very large pores, the phase behavior becomes similar to the bulk phase where the pore/wall interactions can be ignored. Such behavior can be observed in pores of diameters larger than 40 nm in our simulation case (region III).

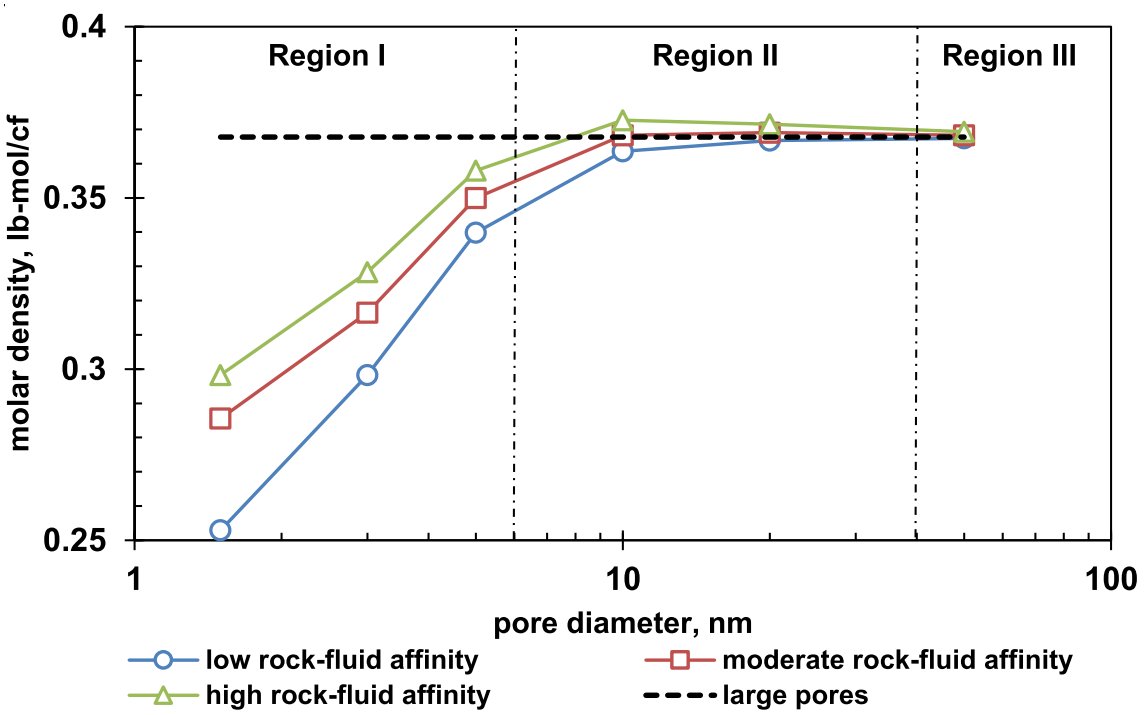

Figure 3.7: Molar density of octane (at 6000 psi and 212°F) in small pores for different pore sizes at various fluid–wall affinities. The $\frac{\epsilon_{\mathrm{p},i}}{\mathrm{k}}$ values for low, moderate, and high rock–fluid affinities are 1200, 3102, and 5300 K, respectively.

Now, let us investigate the effect of size filtration on composition distribution of mixtures. To do that, we need to have the attractive energy parameter ($\frac{\epsilon_{\mathrm{p},i}}{\mathrm{k}}$) and range parameter ($\frac{\delta_{\mathrm{p},i}}{\sigma_i}$) for all the hydrocarbon molecules with the medium of interest. The above mentioned parameters are found for hexane and octane based on the experimental data by Gupta et al. [96]. As the experimental data is not available for other hydrocarbons, we used the data from hexane and octane to estimate that of other hydrocarbons. The energy parameter ($\frac{\epsilon_{\mathrm{p},i}}{\mathrm{k}}$) for normal alkanes were extrapolated based on their molecular mass. That means larger molecules would feel a stronger attractive force from the wall and exhibit a larger $\epsilon_{\mathrm{p},i}$ value. A uniform average $\frac{\delta_{\mathrm{p},i}}{\sigma_i}$ was considered for all hydrocarbon molecules. Table 3.2 provides the

attractive energy and range parameters used in this section.

Table 3.2: The following experimental and extrapolated $\frac{\epsilon_{\mathrm{p},i}}{\mathrm{k}}$ and $\frac{\delta_{\mathrm{p},i}}{\sigma_i}$ parameters for different hydrocarbon species were used in the current paper.

	$\frac{\epsilon_{\mathrm{p},i}}{\mathrm{k}}$ (K)	$\frac{\delta_{\mathrm{p},i}}{\sigma_i}$ (unitless)
Methane	1684	0.49
Ethane	1887	0.49
Hexane	2697	0.56
Octane	3102	0.46
Dodecane	3912	0.49

Let us start with two binary mixtures of C_6/C_8 and C_6/C_{12} in a system where the pore diameter in small pores is 5 nm and temperature is 212 °F. Figure 3.8 shows the mole fraction of hexane in small pores versus pressure. As depicted in the graph, the hexane mole fraction in large pores is 0.3 for both binary mixtures. The larger the mole fraction of hexane in the small pores, the more pronounced the effect of sieving would be as less of the larger molecules (either C_8 or C_{12}) can enter the small pores in a competition with smaller molecules of C_6. As we can see from the graph, the small–pore mole fraction of C_6 in both binary mixtures is larger than C_6's mole fraction in large pores (0.3). Such behavior is interpreted as size filtration of larger species. In addition to that, it can be seen that the mole fraction of C_6 in small pores is larger for the C_6–C_{12} system, compared to the C_6–C_8 case. In fact, the larger diameter of C_{12} molecules causes a more pronounced steric hindrance so the mole fraction of C_{12} in small pores is less, compared to that of C_8. Figure 3.8 also shows that higher pressures can force more of the heavier species into small pores

(C_6 mole fraction in small pores decreases as pressure increases).

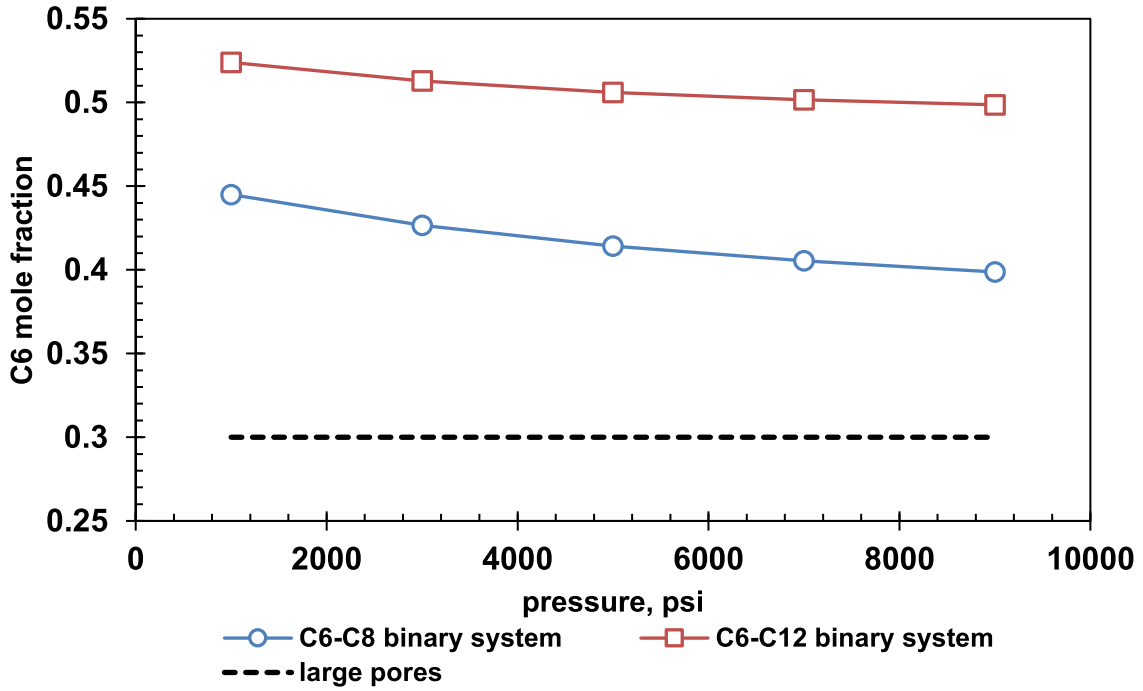

Figure 3.8: The composition distribution of binary mixtures of C_6–C_8 and C_6–C_{12} in a 5 nm wide pore shows larger species (C_8 and C_{12}) will face a steric hindrance when competing with a smaller hydrocarbon (C_6) to enter small pores. The larger the hydrocarbon molecules, the more pronounced the size sieving effect is.

Assume we have a mixture of methane (C_1), ethane (C_2), hexane (C_6), Octane (C_8), and dodecane (C_{12}) at 6000 psi and 212 °F with the following respective mole fractions in large pores: 0.3, 0.1, 0.1, 0.1, and 0.4. Figure 3.9 shows the composition distribution of hydrocarbons in large pores and small pores with a pore diameter of 5 nm and 10 nm. According to the graph, molar concentration of heavier alkanes (C_8 and C_{12}) decreases in small pores. This is attributed to the size filtration effect we have discussed before. In addition to that, comparing the composition distribution in small pores with pore diameters of 5 nm and 10 nm, one can see for smaller pores,

the size filtration effect becomes more noticeable, resulting in a lower concentration of heavier species (C_{12}) and higher values of lighter hydrocarbons (C_1 and C_2).

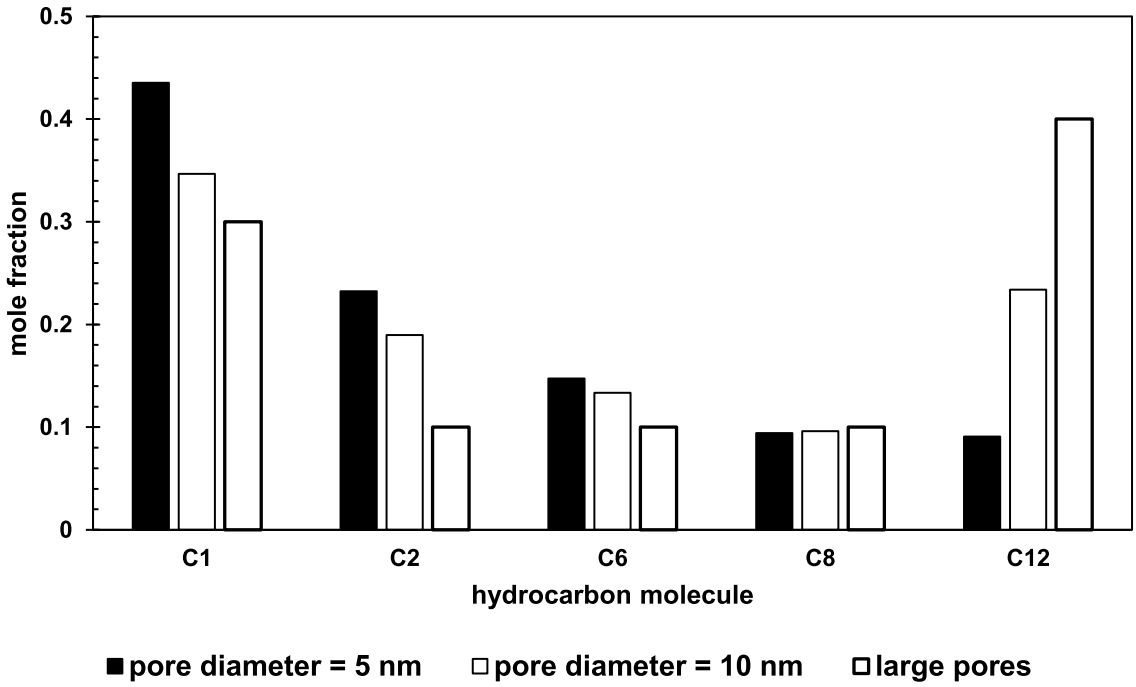

Figure 3.9: Hydrocarbon distribution in small pores shows an apparent sieving effect due to size hindrance and pore–fluid interactions. Heavier hydrocarbons exhibit a lower mole fraction in pores of smaller diameters.

Equilibrium calculations in this section have shown that the composition distribution in shale pores can vary depending on the pore size. In order to have an accurate estimate of hydrocarbon distribution, more details about the porous media, its structure and geology, and pore size distribution are needed. In cases where this information is available, the equation of state model can be tuned accordingly to find the composition distribution. More often than never, such information is not available for the reservoir of interest. In such cases, the initial composition of pores

can be treated as a history matching parameter where material balance is honored and the in–situ composition of the reservoir (if available through preserved cores) or production stream of the reservoir can lead us to an educated initial guess of the composition.

3.6 Impact of sieving on production behavior

In this section, we will provide a synthetic reservoir case and try to analyze the production behavior of the reservoir when sieving takes place. To do that, a sensitivity analysis will be performed on different factors to see their effect on reservoir response. The discussion will continue with a case study in which the production data from an Eagle Ford reservoir is matched with this new model. In order to provide a more realistic picture of the stimulated reservoir volume and fracture network, microseismic events were used to build the Eagle Ford numerical model.

3.6.1 Multiple porosity model

Our multiple permeability approach divides the porous media into different sub–media. To numerically model this phenomenon, each of the grid blocks in the simulator is dimensioned into associated media or porosity/permeability types (sub–grids) at the same location. In this regard, our multiple porosity model is similar to conventional dual permeability cases with the difference being that the matrix is further divided into small pores and large pores with different characteristics. By structure, the model presented in this work is categorized as a multiple permeability model (due to the connectivities among sub–grids of the same type); however, the terms "multiple permeability" or "multiple porosity" will be used interchangeably in this dissertation, for the sake of simplicity. The same is true for terms "permeability" or "porosity" while representing each of the sub–grids or sub–medium types (fracture, large pores, and small pores). Sub–grids representing different porosity types at the

same physical location are considered associated and can be termed as "set." The connectivity within and across porosity types can be adjusted based on the physics of the problem we are investigating. For the specific case of this paper, we have used a triple porosity/permeability approach in which each physical grid is composed of three different porosity types or sub–grids (Figure 3.10). Fracture sub–grids represent the fracture network (induced or natural) in the reservoir. Fracture sub–grids have a relatively higher permeability (compared to shale matrix) but a low porosity, and serve as pathways to produce the stored hydrocarbon in shale matrix through the wellbore. The shale matrix contains two sub–grid types: matrix with large pores (the term "large pores" is interchangeably used in this paper to represent this medium) and matrix with small pores (the term "small pores" is interchangeably used in this paper to represent this medium). Each of these porosity types or sub–grids can have their own initial composition, porosity, wettability, compressibility and rock properties, capillary pressure, and relative permeability. Compared to small pores, large pore sub–grids will have a larger permeability. The small pore diameter in small pores will impose a specific space hindrance, as discussed in the previous section, which causes the fluid composition in this porosity to be lighter than that of large pores. As we can see from Figure 3.10b, all three sub–porosities in one set are connected to each other (through appropriate transfer functions) and to similar sub–grids in adjacent sub–grid sets (in either 1D, 2D, or 3D configurations). The capability of assigning different petrophysical and hydraulic properties and initial conditions to each of these permeability types helps our model to provide a close–to–reality picture of the flow dynamics in heterogeneous shale reservoirs. Similar portioning approaches to divide the shale matrix into kerogen/inorganic sub–blocks was discussed by a number of authors [11, 13, 61, 98, 99, 100, 101, 102, 103].

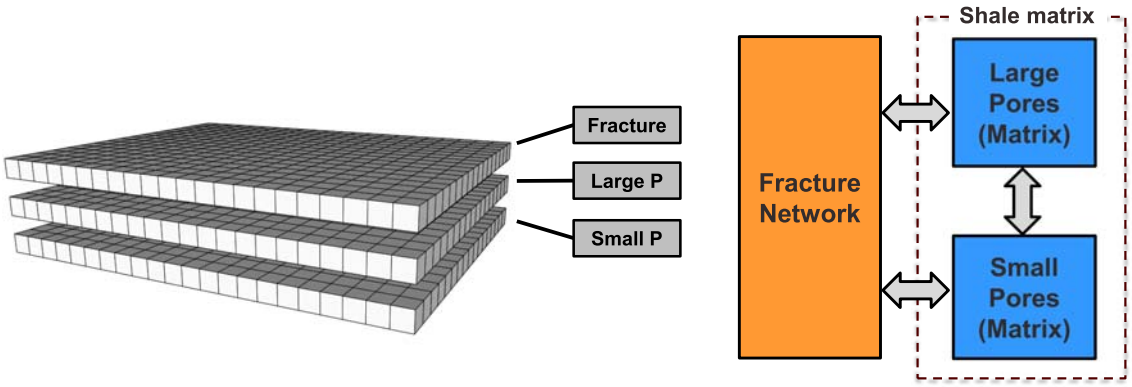

(a) Triple permeability model with three distinctive porosity/permeability types (sub–grids) connected to each other.

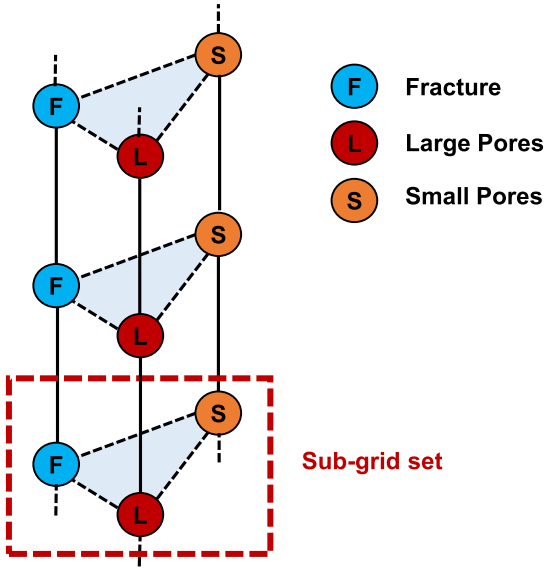

(b) A schematic of how different sub–grids are connected to each other through inter–grid (solid lines) and intra–grid connections (dashed lines) in a 1D array of sub–grid sets or grid blocks. Each circle represents a specific sub–grid (they all have the same physical location) and three connected sub–grids represent one sub–grid set or physical grid.

Figure 3.10: The triple permeability model used in this study to account for sieving and size filtration effects in liquid rich shales.

3.6.2 Base case model

To analyze the effect of sieving on oil and gas production, a triple porosity synthetic reservoir model is used in this section. A compositional approach is employed and fluid flow in the reservoir is modeled using Nexus Desktop from Landmark [104]. The reservoir of interest in this section is part of a horizontal well with multiple transverse fractures. To reduce the computational load, we will focus on a 1000 ft $\times$ 1000 ft area of the reservoir, where three fracture stages with a 325 ft cluster spacing constitute the stimulated reservoir volume. Fracture half–length is assumed to be 250 ft. The reservoir is modeled using a triple porosity approach where three distinctive porosity types are recognized as: matrix with large pores, matrix with small pores, and fracture. The numerical model consists 39$\times$39$\times$5 grid blocks (i, j, k) with each grid block of the size 25$\times$25$\times$25 ft (x, y, z). Figure 3.11 shows a picture of the area of study along with the stimulated reservoir volume. Fractured volume in the reservoir is divided into two regions. Hydraulic fractures are accounted for by considering a slab crossing the horizontal well where we have perforations. The stimulated reservoir volume is extended 75 ft from both sides of the hydraulic fractures by considering micro fractures with a lower permeability compared to hydraulic fractures.

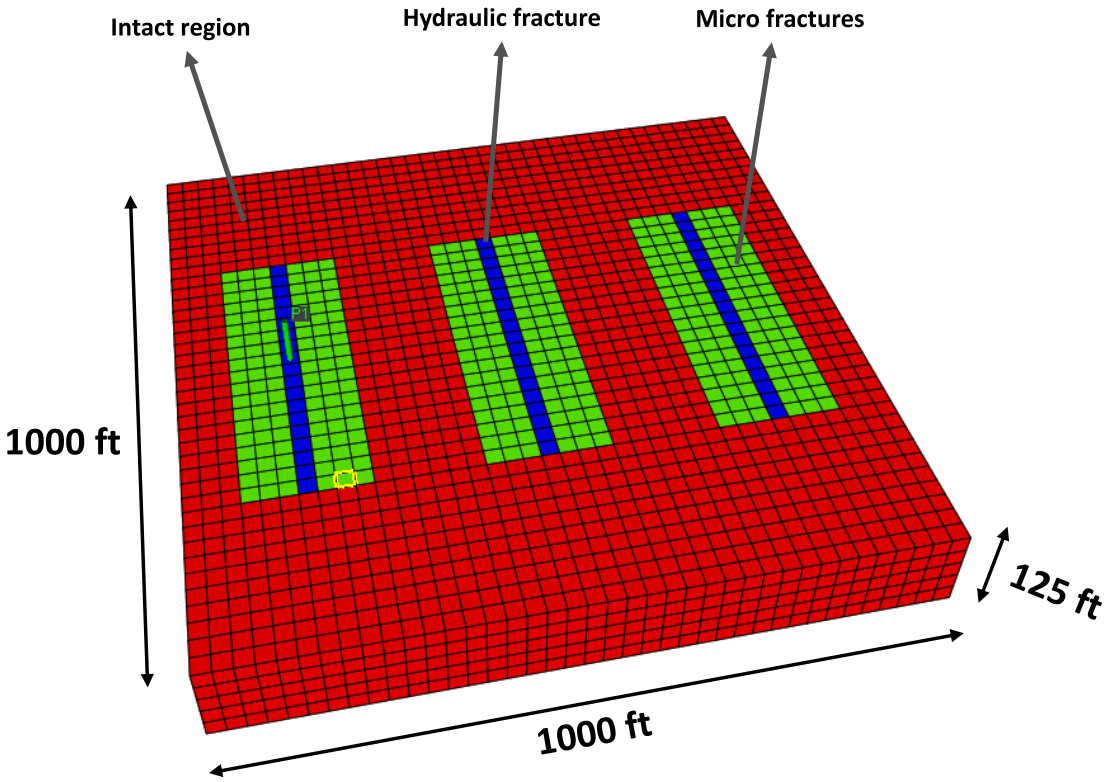

Figure 3.11: Reservoir dimensions along with the fracture distribution for the synthetic reservoir model. The blue blocks show the hydraulic fracture plane, the green region shows the micro fracture distribution (blue and green blocks constitute the stimulated reservoir volume) and the red blocks show the unfractured reservoir volume.

For an easier interpretation, porosity of small pores and large pores are considered to be equal (0.03) for the base case in our synthetic model. Note that such properties are not necessarily equal for the large and small pores and can differ from case to case based on the available geological data. It is intuitive to assume that larger pores can provide a better pathway for fluid flow, hence exhibiting a higher permeability. Permeability of large pores in our model is assumed to be 50 nd, while that of small pores is 5 nd. Fracture grids in the current model are upscaled to coarse blocks of 25

ft width. Assuming a fracture conductivity of 12.5 md.ft for the hydraulic fracture, the equivalent permeability for hydraulic fracture grid blocks is 0.5 md when the grid width is 25 ft. Fracture conductivity in micro fractures is assumed 1/1000th of the hydraulic fractures, yielding the permeability in upscaled micro fracture grids to be 0.0005 md. The well is producing at a constant bottomhole pressure of 1500 psi during the production period.

Initial reservoir pressure in our simulations is 8200 psi and reservoir temperature is 270 °F. Table 3.3 shows the reservoir fluid composition used in our case. To find the composition distribution in large and small pores, we assumed an average pore diameter of 5 nm for small pores and computed the fluid distribution in large and small pores. As we can see from the table, the fluid in small pores exhibits a lighter nature. The saturation pressure at small pores is 2127 psi and the solution gas–oil ratio for the fluid in small pores is 4768 scf/STB. On the other hand, the fluid in larger pores exhibits a rather heavier nature where the bubble point pressure is 1431 psi and its solution gas–oil ratio is 724 scf/STB. Recombining the fluids in large and small pores (based on each media's porosity) will give us a third fluid composition, which is the overall (or global) composition or the "no–sieving" fluid. The no–sieving composition here refers to cases where the hydrocarbon composition in large and small pores are the same and is equal to that of the given overall composition in the reservoir. The no–sieving case has exactly the same reservoir properties, and hydrocarbon overall–mole–in–place as the sieving case. Comparing the no–sieving and sieving cases will help us understand the impact of sieving on reservoir performance. The no–sieving fluid has a bubble point pressure of 1923 psi with a solution gas–oil ratio of 1774 scf/STB.

Table 3.3: In–situ reservoir fluid composition for cases with and without sieving.

	No–sieving composition	**Sieving composition**	
		Small pores	Large pores
C_1	0.33	0.38	0.25
C_2	0.14	0.18	0.08
C_3	0.1	0.12	0.09
C_4	0.1	0.11	0.08
C_5	0.13	0.12	0.15
C_{6+}	0.20	0.09	0.35

Figure 3.12 compares the gas saturation in small and large pores with that of the no–sieving case, five years after production starts. As evident from the graph, gas saturation in small pores is higher than that of large pores. This is because small pores have a lighter hydrocarbon composition with a higher bubble point pressure. Hence, gas evolves sooner in such pores. However, the rock permeability in small pores is lower than that of large pores. In other words, because of sieving, the reservoir retains more of gas–rich fluid while allowing more oil to flow into the well. This behavior can be responsible for the anomalous gas–oil ratios in liquid shales where the observed gas–oil ratio is lower than the expected gas–oil ratio. Another explanation for such behavior in liquid shale reservoirs can be related to the effect of high capillary pressure in low permeability shale and its influence upon phase behavior of the reservoirs [48, 80, 84, 85]. Gas saturation in the no–sieving case is somehow between that of the large pores and small pores.

Sieving case

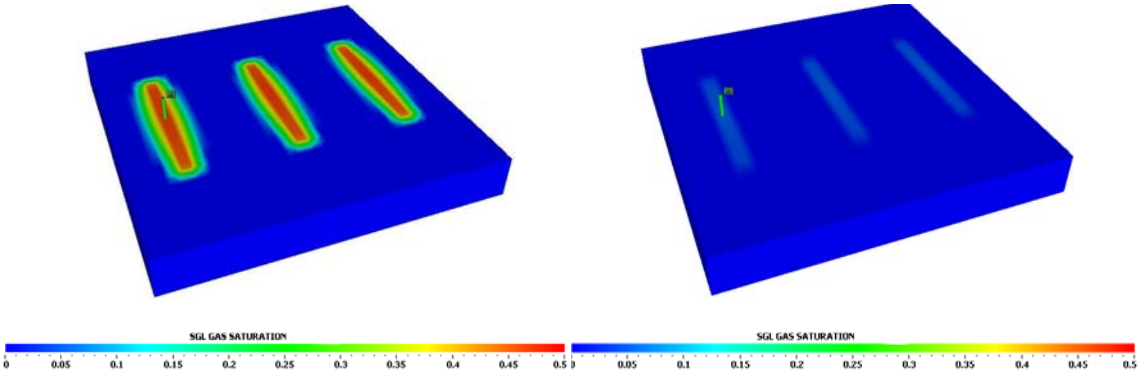

(a) Gas saturation in small pores

(b) Gas saturation in large pores

No–sieving case

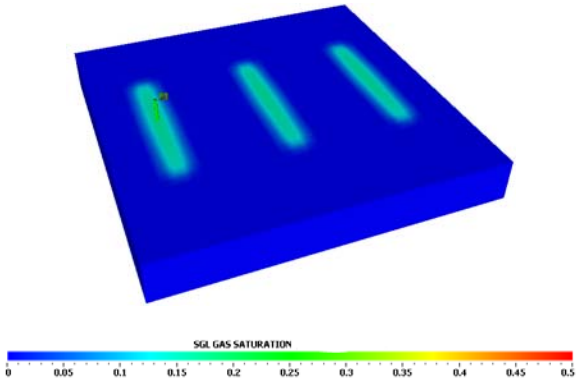

(c) Gas saturation for the no–sieving case

Figure 3.12: (a,b) Gas saturation maps in the small pores and large pores (5 years after production) show a higher gas saturation in small pores due to a lighter composition in such pores, (c) gas saturation for the no–sieving case where the composition is considered to be uniformly distributed in the reservoir.

Figure 3.13 shows the producing gas–oil ratio for sieving and no–sieving cases. The horizontal line in this graph (1774 scf/STB) shows the solution gas–oil ratio for the global reservoir composition. This is when we combine the fluid in small and large pores and put this global composition in a homogeneous reservoir with no small or large pores. In no–sieving cases, gas–oil ratio at the beginning is equal to the global composition solution gas–oil ratio. Gas evolves in the reservoir and producing gas–oil ratio increases as production starts. On the other hand, sieving phenomenon decreases the producing gas–oil ratio from the reservoir. In fact, sieving process causes production well stream to be heavier than the no–sieving cases. Because of size filtration, heavier hydrocarbons are stored in larger pores with higher permeabilities and when production starts, such pores form a considerable portion of the production.

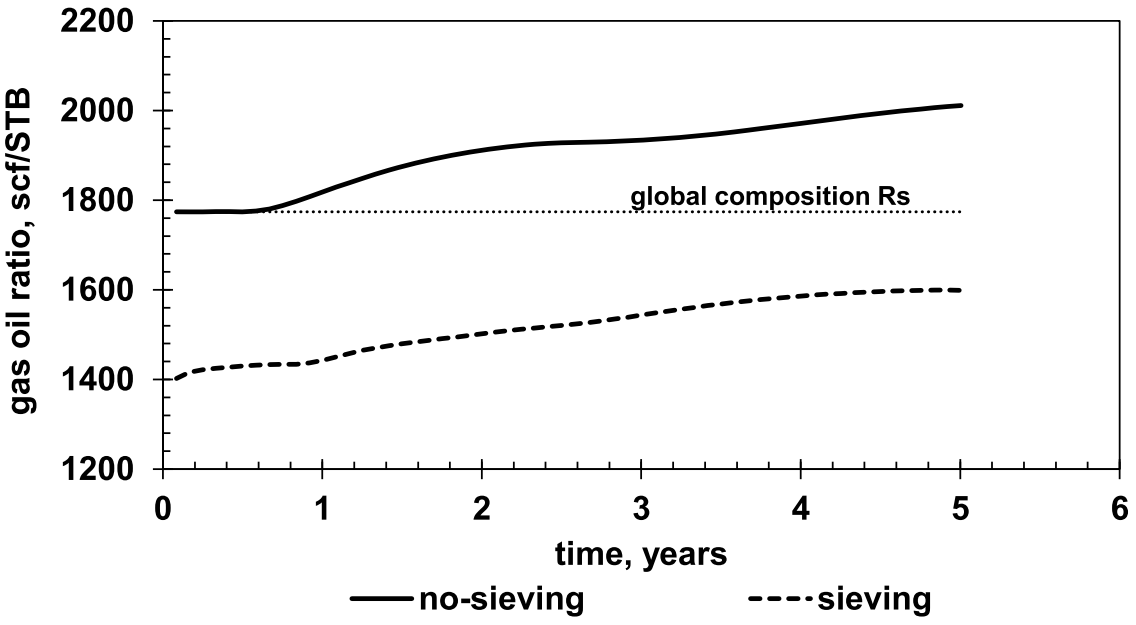

Figure 3.13: Producing gas–oil ratio for the cases with and without sieving and comparison to the global fluid solution gas–oil ratio shows that sieving can alter the production stream (compared to the no–sieving fluid) towards producing more of the heavy components. Gas–oil ratio decreases when sieving happens in the reservoir.

Such effects can be better analyzed by comparing the global mole percentage of C_1 and C_{6+} with that of the producing well stream for reservoirs with sieving (Figure 3.14). The producing well stream shows that the mole fraction of methane in the produced fluid is less than the total methane fraction inside the reservoir. In contrast, the well stream is richer in C_{6+} (heavier components), compared to the global reservoir fluid. Our results reveal that size filtration and space hindrance can cause the produced fluid composition to be different from the in–situ fluid, in favor of a heavier well stream.

3.6.3 Sensitivity analysis

The effect of permeability ratio and sieving degree on reservoir performance is analyzed in this section. Figure 3.15 compares the influence of permeability contrast (in large and small pores) upon producing gas–oil ratio. For this purpose, we have considered a case with permeability of large pores equal to 50 nd and small pores equal to 5 nd (large to small permeability ratio is 10). The second case has large pores with a permeability of 250 nd while the permeability of small pores is still 5 nd and the permeability ratio ($\frac{K_L}{K_S}$) is 50. As we can see from the graph, when the permeability contrast between larger and smaller pores ($\frac{K_L}{K_S}$) increases, the relative capacity of larger pores increases, which can be translated into more produced oil and a lower gas–oil ratio.

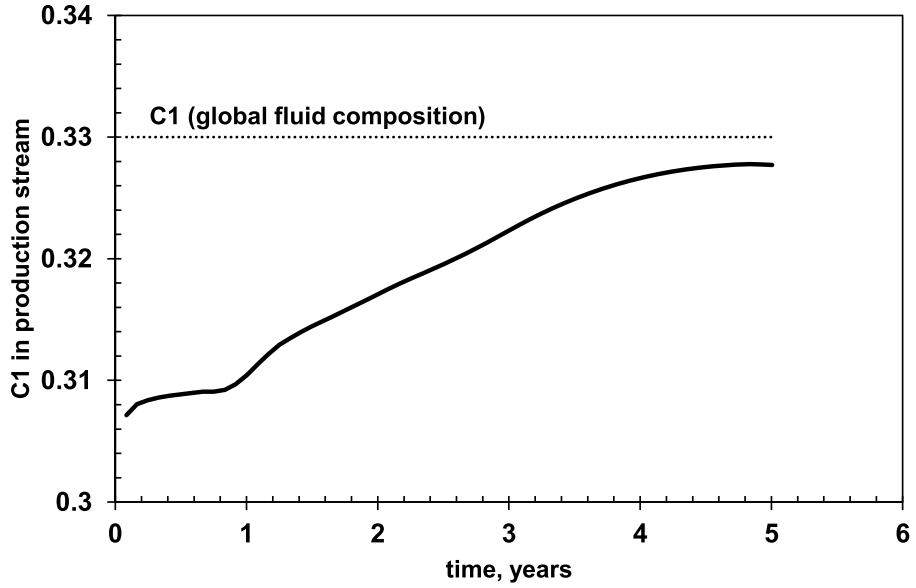

(a) C_1 mole fraction in producing well stream

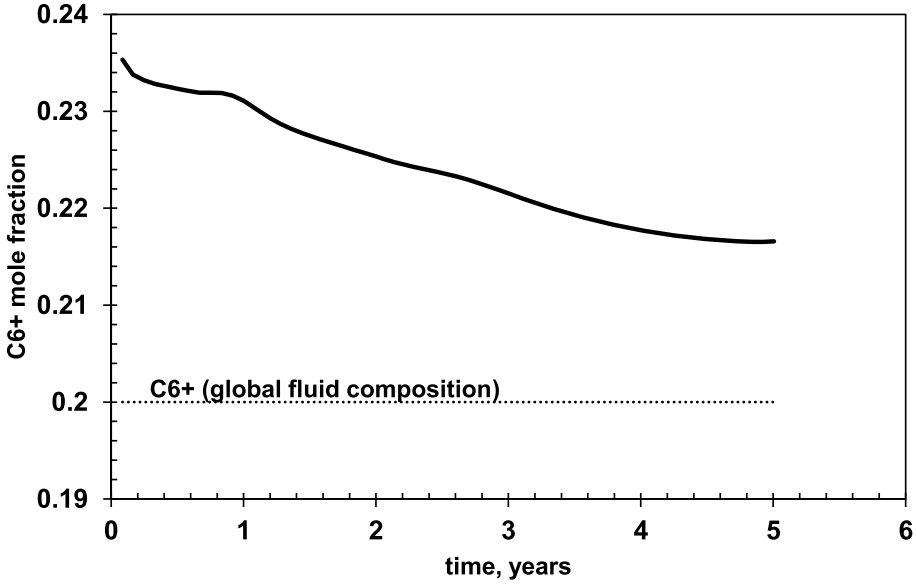

(b) C_{6+} mole fraction in producing well stream

Figure 3.14: Producing well stream shows that sieving causes the produced fluid to be heavier than the in–situ reservoir fluid.

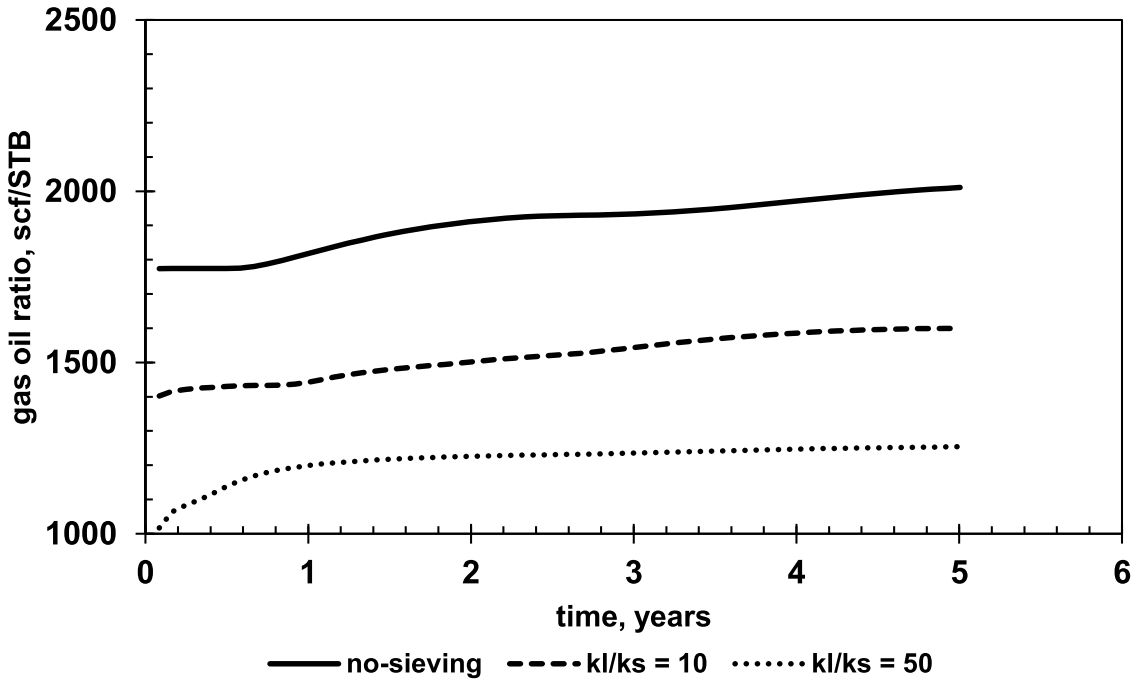

Figure 3.15: Producing gas–oil ratio in the reservoir decreases by increasing the permeability contrast ($\frac{K_L}{K_S}$ shows the ratio of permeability in large pores to that of small pores).

Figure 3.16 depicts the producing gas–oil ratio for two sieving cases and compares it to the no–sieving case. For all cases, $\frac{K_L}{K_S}$ is equal to 10. The low–sieving term refers to a case where the small–pore diameter is about 25 nm. This means the sieving is less intensified compared to the moderate–sieving case with a pore diameter of 5 nm in small pores. As the pore size in small pores increases, the composition of the fluid in small pores and large pores become similar to each other and to that of the no–sieving or overall composition and sieving effect will fade away. Table 3.4 shows the reservoir compositions. According to Figure 3.16, we can see the more pronounced the sieving effect, the lower producing gas–oil ratio will be. Similar to what was discussed before, the moderate sieving cases put more of the heavier compounds in the higher permeability large pores and increases the oil production potential.

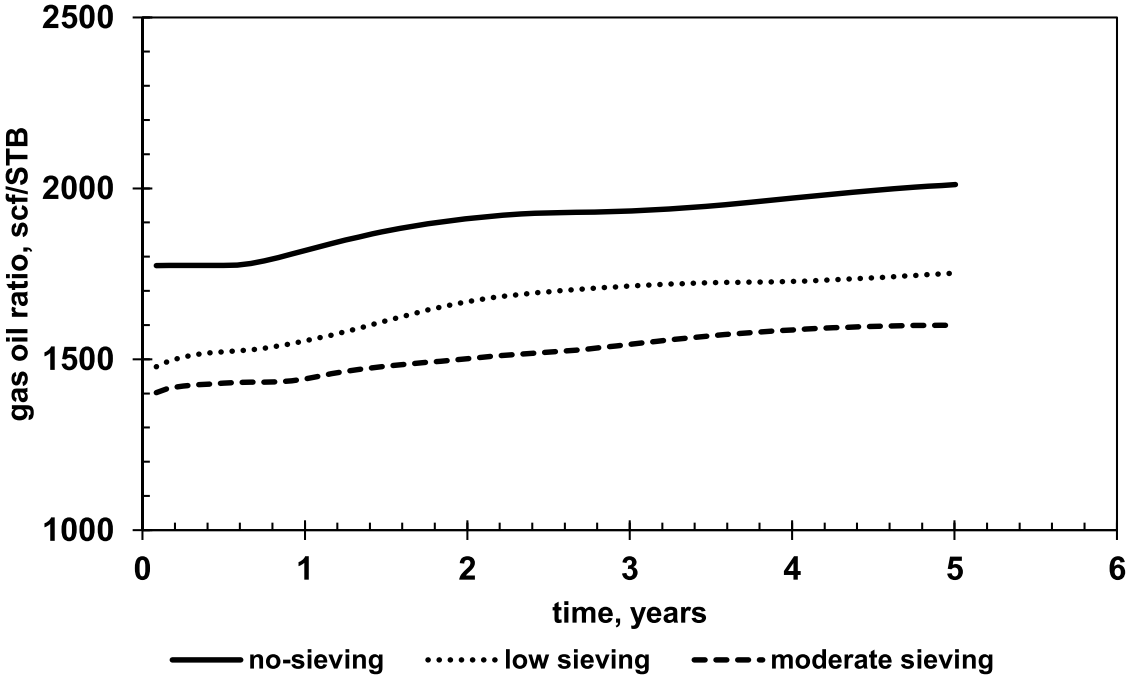

Figure 3.16: Producing gas oil ratio in the reservoir decreases as sieving becomes more pronounced.

Table 3.4: In–situ reservoir fluid composition for low sieving and moderate sieving cases.

	No–sieving	**Low sieving**		**Moderate sieving**	
		Small pores	Large pores	Small pores	Large pores
C_1	0.33	0.35	0.29	0.38	0.25
C_2	0.14	0.16	0.12	0.18	0.08
C_3	0.1	0.11	0.10	0.12	0.09
C_4	0.1	0.10	0.11	0.11	0.08
C_5	0.13	0.11	0.14	0.12	0.15
C_{6+}	0.20	0.17	0.24	0.09	0.35

3.6.4 Eagle Ford case study

To analyze the applicability of the presented model, we have studied an Eagle Ford case and tried to match the production data using the above mentioned multiple permeability model and sieving concept. This section provides detailed information about the reservoir properties, in–situ fluid, well completion scenarios, seismic acquisition, and the numerical reservoir model.

3.6.4.1 Reservoir dimensions and well completion

To analyze the applicability of the presented model, we have studied an Eagle Ford case and tried to match the production data using the above mentioned multiple permeability model and sieving concept. The reservoir of interest in this study is producing through a 5500 ft long horizontal well with 22 fracture stages of 250 ft spacing. The well spacing is 900 ft and the reservoir has a payzone thickness of 175 ft. In this case, we will focus on one single well with no flow boundaries extended from both sides. The well was completed with HiWAY channel–fracturing stimulation treatments, to create stable channels within fractures and decouple fracture conductivity from the proppant pack, where crosslinked gel was employed as the fracturing fluid. The designed volumes of treatments were approximately 15000 gallons of total fluid, with 130000 lbs of proppant, placed at 60 barrels per minute. Table 3.5 shows the treatment well data for the well of interest.

Table 3.5: Treatment well data

Well type	Horizontal
Completion	Perf/Plug
KB (ft)	300
Total measured depth (ft)	16802
Maximum vertical depth (ft)	11113
Casing data	5–1/2" 20 lb/ft

3.6.4.2 Fluid properties

The fluid model in Eagle Ford case is built based upon a complete set of PVT experiments from the field. At the reservoir temperature of 270 °F, the reservoir fluid shows a saturation pressure of 2866 psi. The fluid is initially considered to be undersaturated as the initiation reservoir pressure (8250 psi) is well above the bubble point pressure. At reservoir conditions, the reservoir fluid has a density of 0.659 gr/cc and a formation volume factor of 1.528 rb/STB, while the fluid viscosity and compressibility are 0.327 cp and 9.59×10^{-6} 1/psi. The separator gas has a specific gravity of 0.755. Table 3.6 shows the composition of the reservoir fluid.

Table 3.6: Molar composition of the Eagle Ford fluid sample with hydrocarbons up to C_{30}.

Component	**Mole%**	**Component**	**Mole%**	**Component**	**Mole%**
N_2	0.17	C_8	3.44	C_{20}	0.599
CO_2	1.272	C_9	2.986	C_{21}	0.527
H_2S	0.0	C_{10}	2.588	C_{22}	0.479
C_1	40.79	$_{11}$	1.981	C_{23}	0.412
C_2	10.594	$_{12}$	1.562	C_{24}	0.373
C_3	6.983	C_{13}	1.558	C_{25}	0.335
iC_4	1.191	C_{14}	1.337	C_{26}	0.301
nC_4	3.162	C_{15}	1.162	C_{27}	0.281
iC_5	1.339	C_{16}	.939	C_{28}	0.259
nC_5	2.001	C_{17}	0.841	C_{29}	0.22
C_6	2.632	C_{18}	0.779	C_{30+}	3.02
C_7	3.105	C_{19}	0.753		

Figure 3.17 shows the results of constant composition expansion experiments on the reservoir fluid. The results of differential liberation experiments show how liquid density, liquid viscosity, gas viscosity, formation volume factor, and solution gas oil ratio change with pressure (Figure 3.18).

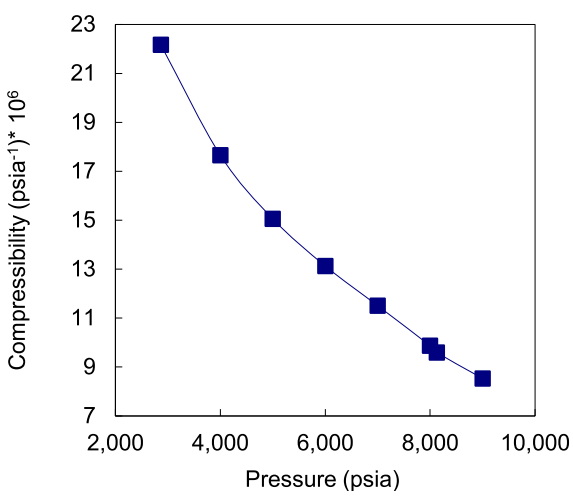

(a) Oil compressibility

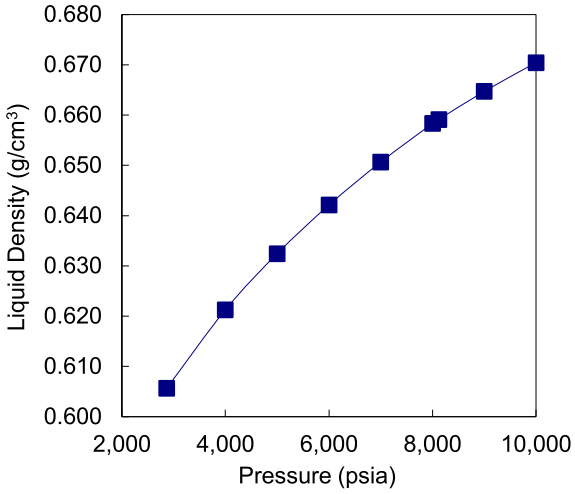

(b) Liquid density

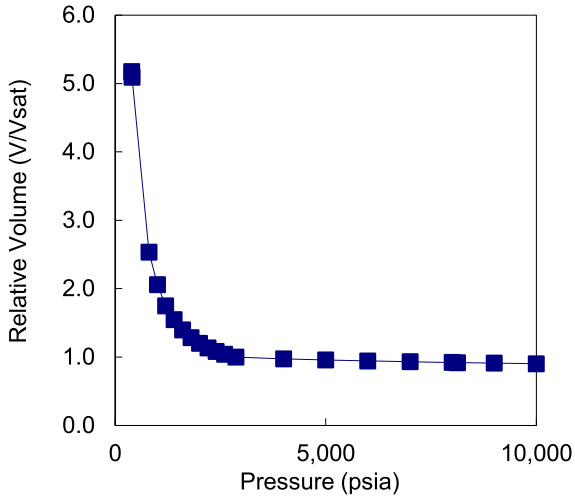

(c) Pressure volume relations

Figure 3.17: Constant composition expansion experiments on the Eagle Ford sample of interest.

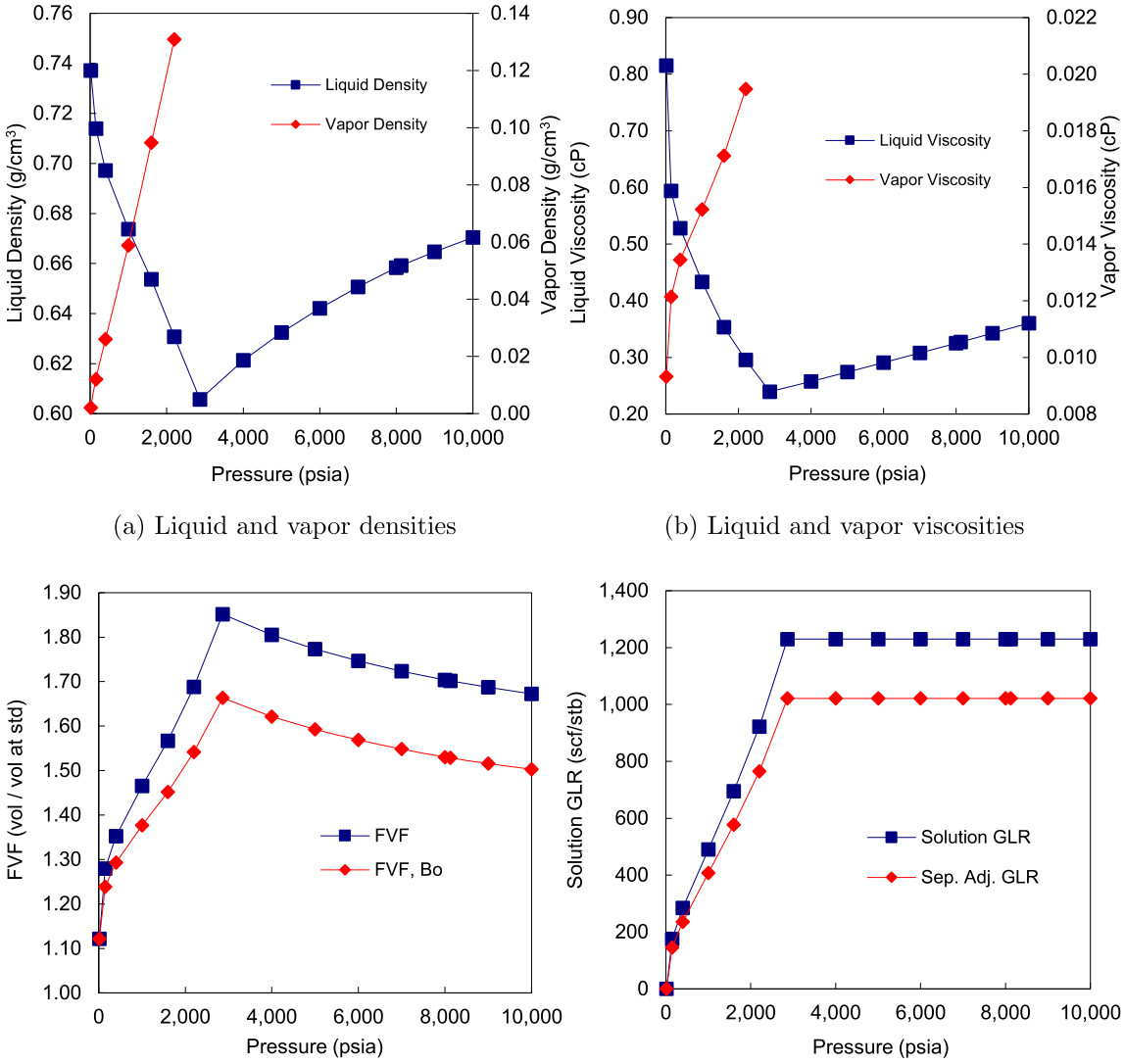

(a) Liquid and vapor densities

(b) Liquid and vapor viscosities

(c) Oil formation volume factor

(d) Solution Gas liquid ratios

Figure 3.18: Differential liberation experiments on the Eagle Ford sample of interest.

3.6.4.3 Microseismic events

For a more reliable reservoir simulation, effective reservoir management, and optimized wellbore completion, it is highly desirable to have an accurate estimate of the stimulated reservoir volumes. While in many simulations, fractures are considered planner with an estimate of the fracture half–length, such an approach is not able to capture the complex nature of the induced fracture network. Instead, microseismic events can be used to produce a more realistic representation of the fracture extent in the reservoir. In reservoirs where complex fracture networks are created, the concept of the stimulated reservoir volume from microseismic events applies. Microseismic events are generated as a byproduct of the hydraulic fracturing process, which can be detected by a nearby geophone array. In the current study, we take advantage of the availability of microseismic events to directly generate the stimulated reservoir volume and import it into the simulation model. Out of the 22 fracture stages in this case, microseismic data is available for the last 11 stages (half of the total fracture stages). This data is used to generate the fracture network and study the reservoir performance for half of the well length, while dividing the total production rates by two. Figure 3.19 shows a map view of the microseismic events for the reservoir of study in this section.

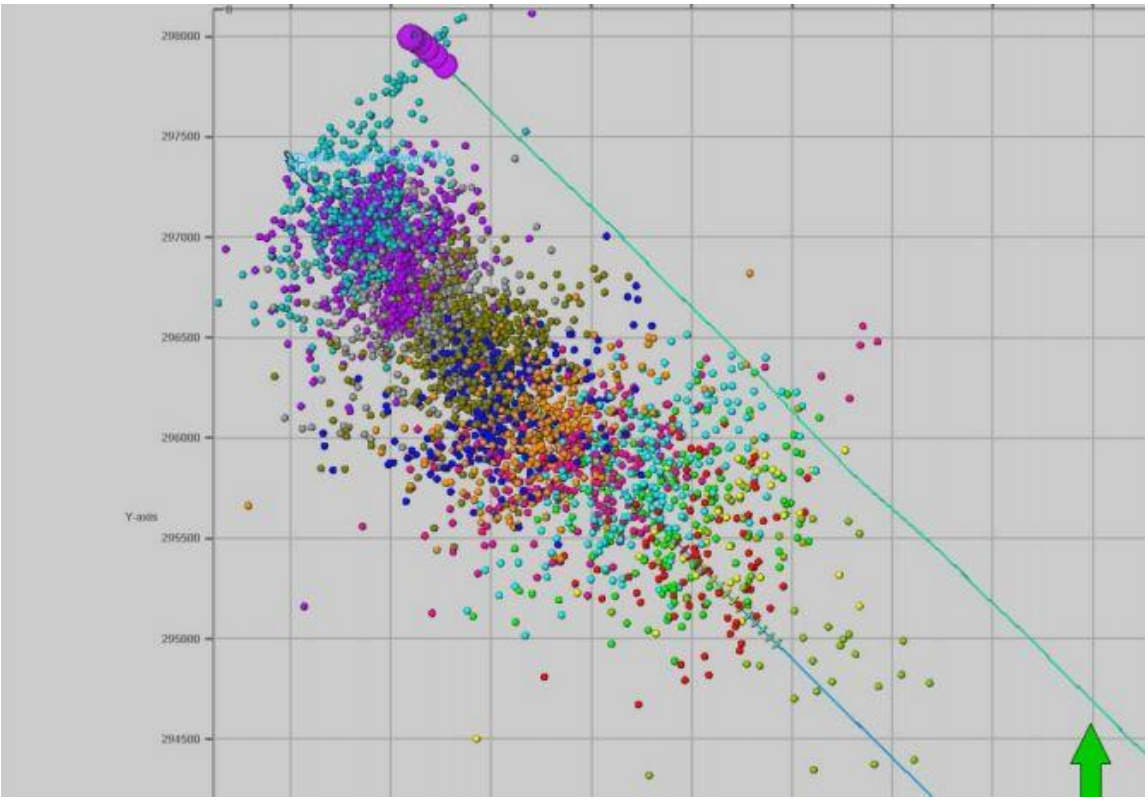

Figure 3.19: Map view of the microseismic events from the well of interest.

The total data set was scanned with an event detector algorithm which first detects signals above a given signal–to–noise (SNR) threshold on each shuttle. Location confidence improves as the signal–to–noise ratio increases. For each detected signal, the known velocity model can be used to calculate a range of expected signal arrival times for the other shuttles. Signals arriving in these expected time ranges are said to be associated, meaning they come from the same microseismic event. If signals are detected on a given minimum number of shuttles, an event is declared and stored in an event file for further processing. Figure 3.20 shows a summary of the event count for each of the 11 fracturing stages. The sonic logs in the well of interest were used to build the velocity model. P&S wave sonic slowness logs were converted to

P wave velocity and S wave velocity, smoothing and blocking was applied to the raw P and S wave velocity logs to build the initial model. The distance from the center of the geophone array in the monitor well ranged from 3,400 ft to 1,100 ft where 12 geophones were used in a vertical orientation with the spacing of 100 ft. The detection threshold in microseismic interpretation is the minimum magnitude necessary to locate a microseismic event at a given distance. To assure the quality of microseismic data for evaluation purposes and minimize spatial bias, events with magnitudes lower than a threshold were filtered out. Filtered data were then used to build the stimulated reservoir volume in the numerical model.

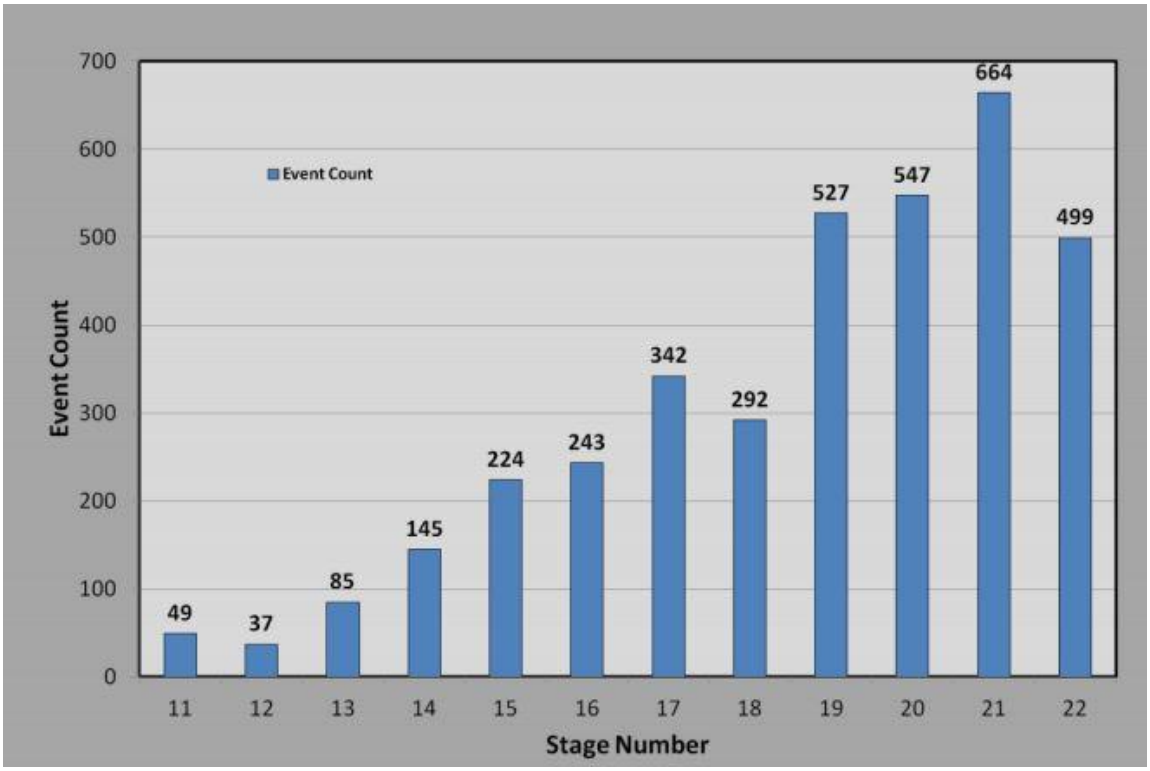

Figure 3.20: Event count by the stage for the modeled well in our simulation case.

3.6.4.4 Numerical model

The Eagle Ford case study is simulated using a 90×36×5 model (16200 grid blocks with grid size of 50×50×35 ft). Microseismic events from the previous section were used to build the reservoir model and fracture network. In the workflow of generating the numerical model, seismic events are spatially bounded and overlaid on a frame of structured gridblocks and fracture gridblocks are activated in cells with one or more seismic events located inside (Figure 3.21).

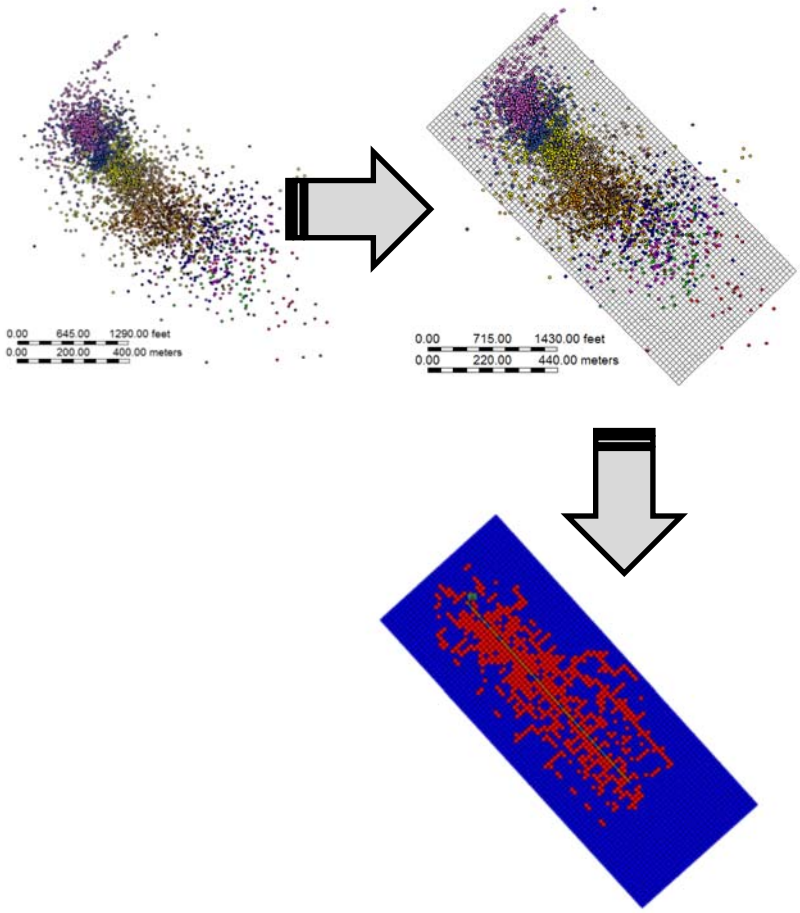

Figure 3.21: In the workflow of generating the numerical model, seismic events are spatially bounded and overlaid on a frame of structured gridblocks and fracture gridblocks are activated in cells with one or more seismic events located inside.

As mentioned before, only 11 fracture stages (out of 22) have microseismic data available so the numerical model covers half of the productive area. The reservoir top is 10600 ft deep, initial reservoir pressure and temperature are around 8250 psi and 270 °F; and reservoir fluid is in liquid phase at these conditions. The well operates with a wellhead pressure constraint and gas and liquid production rates at surface conditions are reported on a daily basis for 2.5 years from the beginning of the production. The triple porosity model explained in the previous section was used to model the reservoir performance. Figure 3.22 shows the reservoir dimensions. The blue blocks show the intact reservoir volume while the red ones represent the stimulated reservoir volume. We can see how fracture grid blocks are connected to each other and to the well.

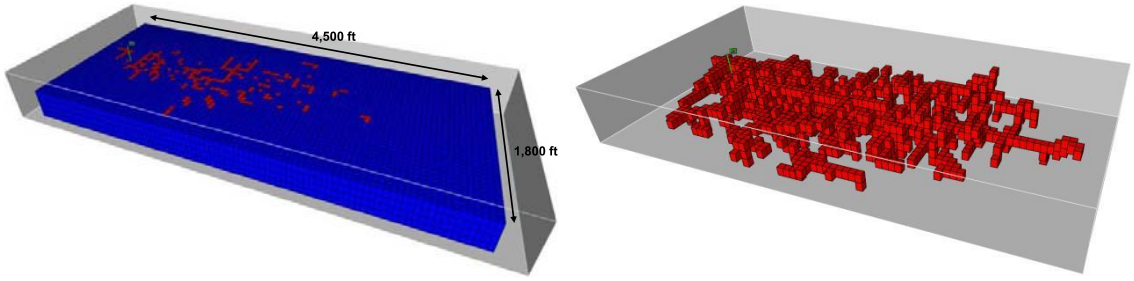

(a) Eagle Ford model dimensions

(b) Fracture distribution in the stimulated reservoir volume

Figure 3.22: Fracture network model generated by the microseismic data. Using the microseismic data to model the stimulated reservoir volume has provided a realistic picture of the induced fracture network.

History matching was performed by adjusting matrix permeability, porosity, relative permeability, and fracture properties. Figure 3.23 show the two–phase relative permeability curves for the best match. Although we assigned different permeability

and porosity values to large and small pores, the relative permeability curves for both media are assumed to be identical as there were no evidence of altering relative permeability based on the pore size. However, this can be adjusted in our model by using different relative permeability tables for each porosity. Furthermore, in cases where additional data on pore size distribution and material characterization of the reservoir rock is available, fluid distribution in small and large pores can be calculated using the procedure provided in previous chapters. However, as in this case, such parameters can be treated as additional history matching knobs wherever needed information about the reservoir rock and its properties is not available.

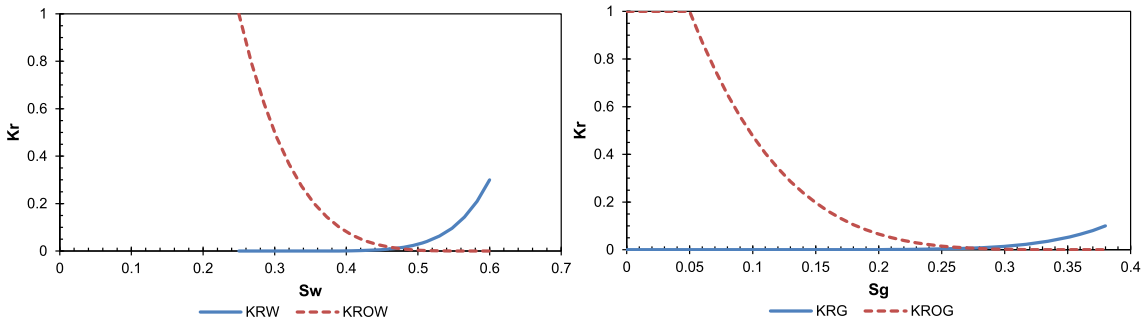

(a) Water oil relative permeability

(b) Gas oil relative permeability

Figure 3.23: Water–oil and gas–oil two–phase relative permeabilities are used in our model to model the three phase relative permeability.

Figures 3.24 and 3.25 show the oil and gas production rates from the field data along with the best match. During the history match process, the wellhead pressure was used as the well operating constraint in which the bottomhole pressure was calculated in a fully coupled surface/subsurface manner. The oil and gas production data were used as the objective function and the difference between simulated production

rates and the field production data was minimized. Although gas oil ratios show a detectable discrepancy (GOR in Figure 3.26 is not matched during the history match process), the current multiple porosity model, with sieving in effect, provides a good match with the oil and gas production data. This implies the robustness of such an approach to predict the complicated reservoir behavior in liquid shale reservoirs.

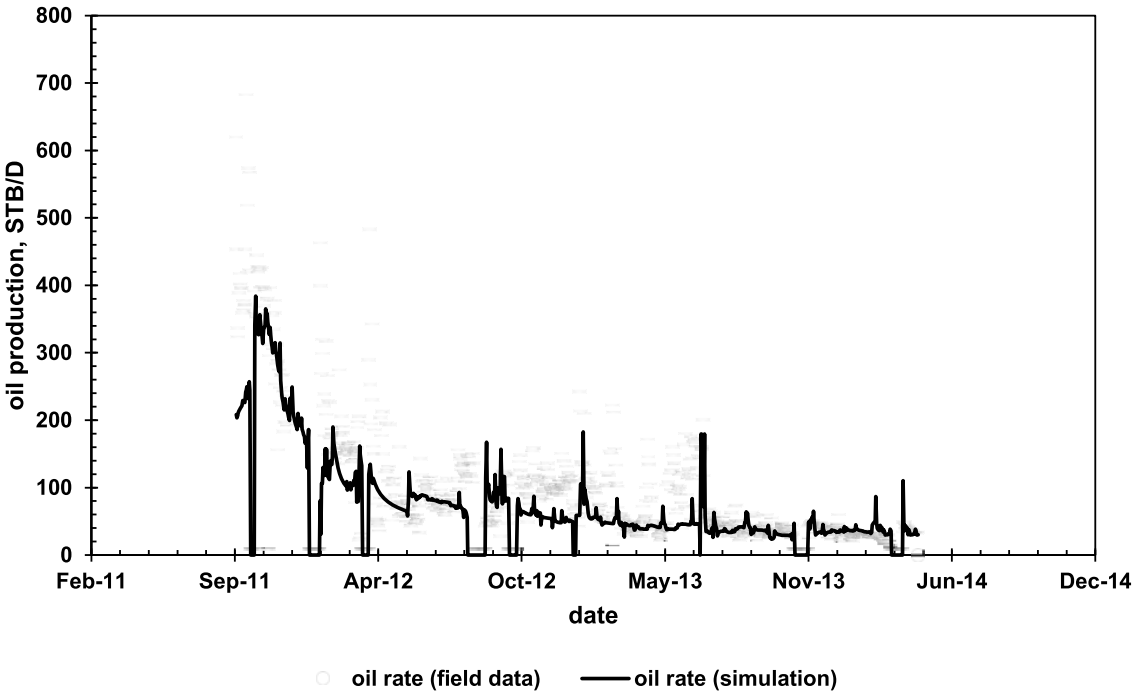

Figure 3.24: Oil production rates from that of field data and simulation closely resemble, increasing our confidence on the reliability of the proposed sieving model.

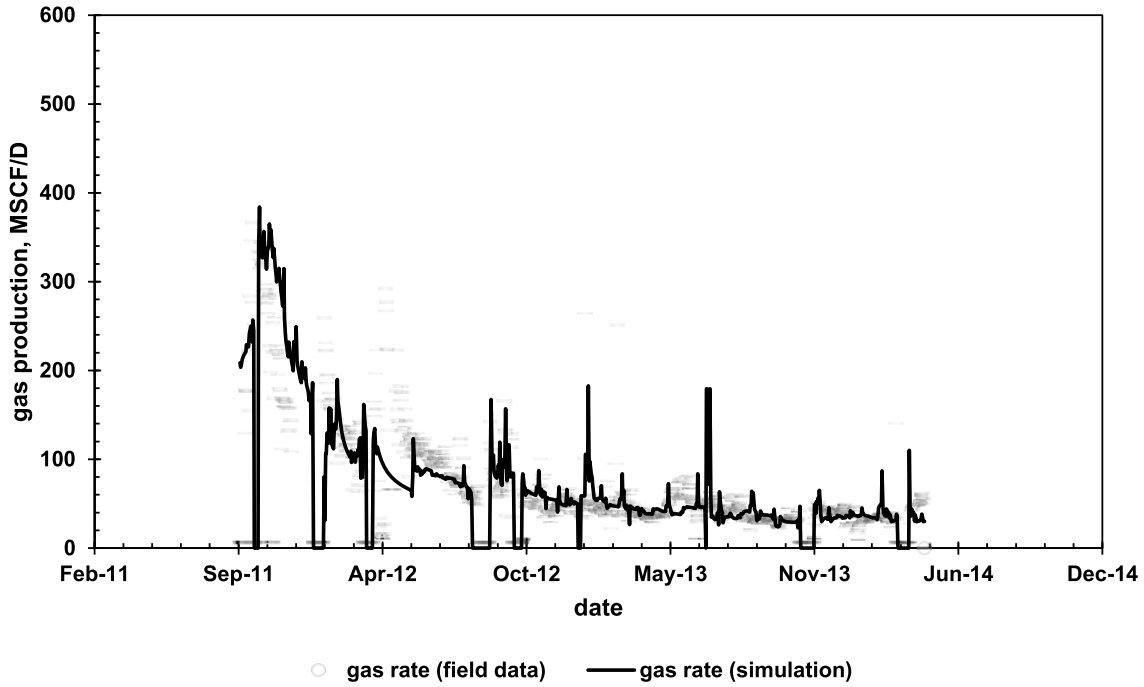

Figure 3.25: Similar to the oil rates, our model closely matches the gas production rates from the Eagle Ford case.

To analyze the flow dynamics in the presented multiple porosity model, Figure 3.27 shows the pressure and gas saturation maps for large and small pores in the middle layer of the reservoir, 2.5 years after production starts. According to the graph, pressure distribution is very similar in small and large pores. However, gas saturation in small pores is considerably higher than that of the large pores. This is attributed to the lighter nature of hydrocarbons in small pores. More information about the numerical model and the input parameters of the commercial simulator (Nexus) is provided in Appendix C.

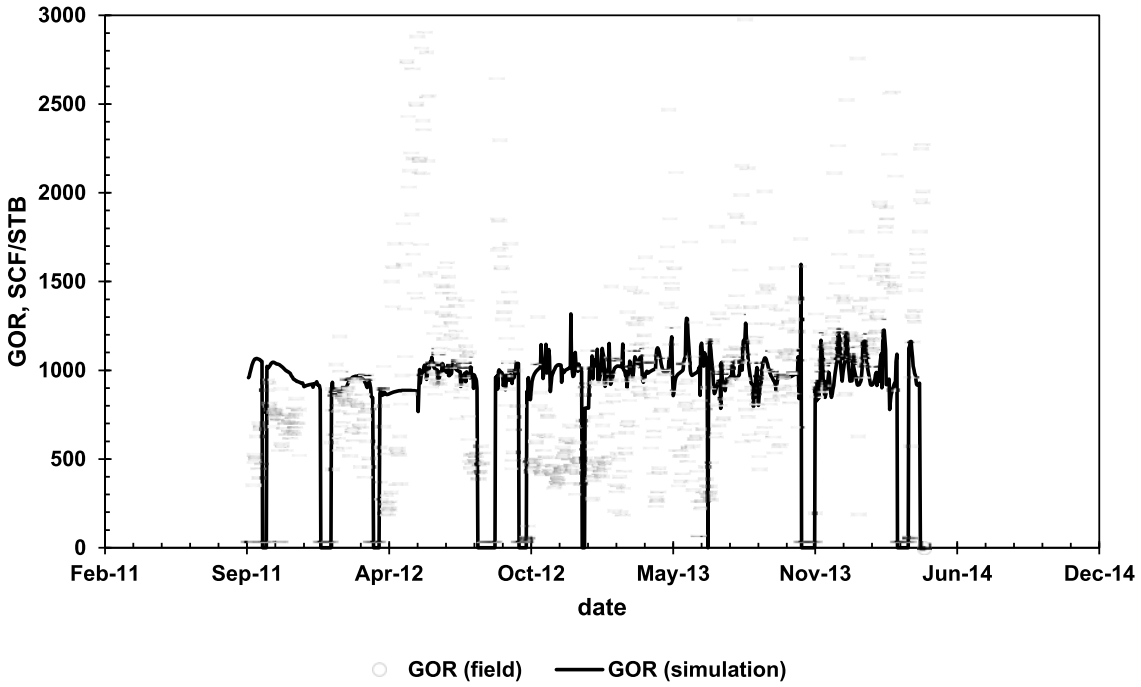

Figure 3.26: Despite oil and gas production, the GOR match of the field and simulation data looks to be poor. Parts of it is attributed to the discrepancy in reading the data as GOR's show a considerable fluctuation.

3.7 Using the fluid–rock affinity in our favor

So far in this dissertation, we have proposed a partitioning scheme to separate the large and small pores in shale rock because of the fact that pores with different sizes can react in complete different ways when exposed to hydrocarbon molecules. Our analysis shows that steric restrictions in small pores will keep larger hydrocarbon molecules (that are most likely to form the oil phase at surface conditions) to enter such pores. As a result, a composition gradient and size filtration phenomenon is conceivable in shale rocks. This process is modeled in the current work by using a modified Peng–Robinson equation of state that accounts for the attractive and repulsive forces between the hydrocarbon molecules and the pore rock. As stated

in section 3.5, the repulsive forces become important specially for cases where the molecule size is comparable to that of the pore size. That has been the focus of this dissertation so far as we showed a size filtration phenomenon can be resulted by such processes. On the other hand, the attractive forces between the pore walls and fluid molecules are also important for relatively larger pore sizes or smaller molecules ("region II" in Figure 3.7). In this section, we will discuss how we can take advantage of such attractive forces by the use of our proposed partitioning approach.

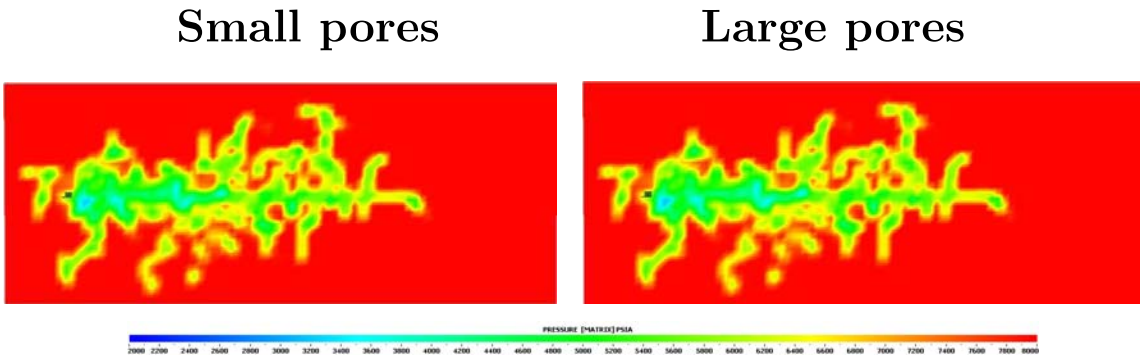

(a) Pressure distribution

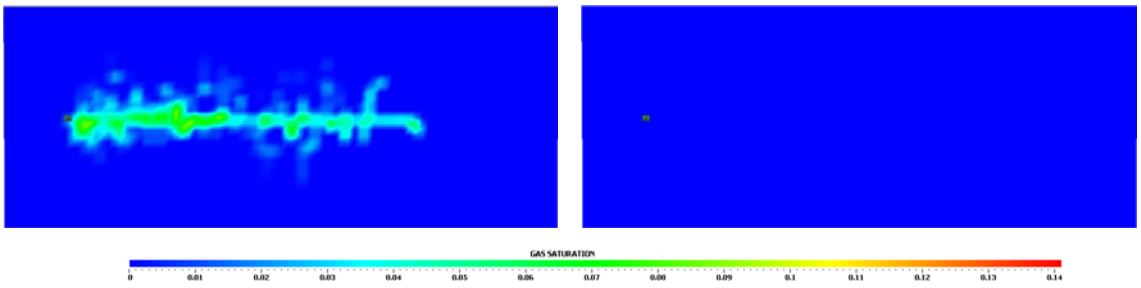

(b) Gas saturation distribution

Figure 3.27: Pressure and gas saturation distribution in small and large pores (middle layer of the reservoir) 2.5 years after production starts.

Typical hydrocarbon recovery factor from hydraulically fractured shale reservoirs

barely reaches 5-7% through the primary recovery mechanism. Such reservoirs are believed to be substantial oil production potentials due to their huge extent. This means even very small improvement in ultimate recovery will make significant difference. A solid understanding of the reservoir behavior is required to suggest an efficient enhance recovery scheme in shale. The proposed model in this dissertation can be implemented as a tool to identify an efficient scenario to boost the hydrocarbon production from shale. For this reason, we will evaluate the potential application of using various fluids (methane, nitrogen, and carbon dioxide) to improve hydrocarbon recovery, in the context of the presented model. To do that, imagine a model similar to the one presented in Figure 3.4. Assuming that the pore size in larger pores is large enough for all EOR gases to go through, large pores are assumed to be saturated with either methane, nitrogen, or carbon dioxide during the gas injection process. Now, the question remains whether these gas molecules can penetrate deep enough into the small pores so they can effectively mix with the oil and push it towards the larger pore or fracture network. Assuming an average pore size diameter of 5 nm (or similar) in the small pores, one can say that neither of the injected gases will face a space hindrance (due to their small molecular size: CH_4 0.38 nm, N_2 0.36 nm, and CO_2 0.33 nm [105]) while trying to enter the small pores and all pores are accessible to the injected gas. Therefore, what makes difference here is the affinity of these molecules to the pore walls, which results in a tendency to enter the small pores.

To model the behavior of each injected gas in our model, we should first tune the equation of state and find the appropriate rock–fluid interaction parameters for each gas (similar to what has been done in section 3.4). Unlike to the very specific problem we were investigating in section 3.4 (adsorption of heavy hydrocarbons in liquid phase), the adsorption data for components of interest in this section can be readily

found in the literature. The experimental data for this section is retrieved from Dreisbach et al. [106]. Dreisbach et al. [106] reported the adsorption equilibrium of CH_4, N_2, and CO_2 on activated Norit R1 Extra, which is an activated carbon molecular sieve. Activated carbon stands for highly porous materials consisting mostly of carbon that exhibit a large internal surface with a homogeneous pore size [107, 108]. Activated carbon molecular sieve is used in this section, as it is believed that this type of molecular sieve can resemble closely the structure of pores in liquid shale with high TOC values and relatively abundant organic matter in their structure. The characteristics of Norit R1 Extra is reported by Himeno et al. [109]. An average pore diameter of 1.94 nm was calculated for this molecular sieve.

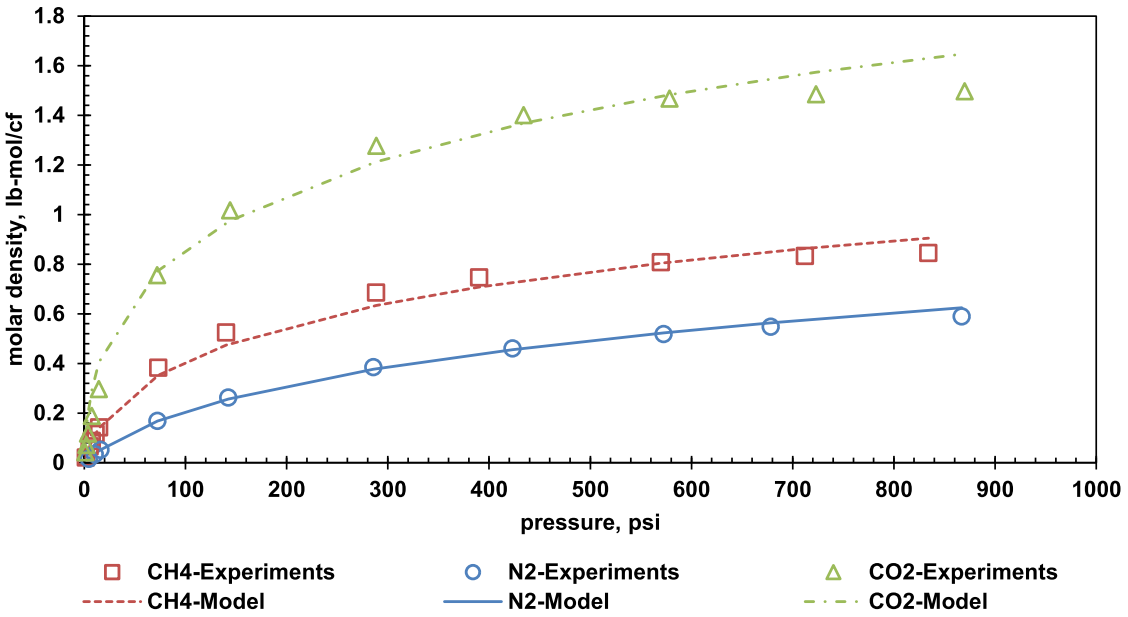

Figure 3.28: Comparison of the density of gases in small pores from the experimental data (reprinted from Dreisbach [106]) and the equation of state model. Experiments are performed at 298K (77 °F).

Figure 3.28 shows the density of CH_4, N_2, and CO_2 in small pores of the activated

carbon versus pressure, measured at 77 °F. Following the same procedure as section 3.4, the rock fluid interaction parameters included in Table 3.7 appear to provide an acceptable match with the experimental data, hence the right parameters to be used in our model.

Table 3.7: Rock/fluid interaction parameters to match CH_4, N_2, and CO_2 adsorption data on activated carbon.

	$\frac{\epsilon_{p,i}}{k}$ (K)	$\frac{\delta_{p,i}}{\sigma_i}$ (unitless)
Methane	1495	0.59
Nitrogen	1080	0.57
Carbon dioxide	2050	0.75

Now that the equation of state is properly tuned, we see which component has a better penetration capability into the small pores. To do that, assume a mixture of 0.3, 0.3, and 0.4, CH_4, CO_2, and N_2 injected into the large pores at 6000 psi and 212 °F. Figure 3.29 shows the injected gas composition (the white bars) along with the mole fraction of these gases in small pores. According to the graph, as an injection EOR gas, CO_2 is able to penetrate more into the small pores, when in competition with other gases. That is because CO_2 has more affinity to the pore walls of small pores, which means easier access to those pores. When we compare the relative penetration capacity of CO_2, N_2, and CH_4 at different pore sizes, one can conclude that the superiority (and efficiency) of CO_2, over to the other EOR gases, increases at smaller pore sizes (5 nm pores have a higher mole fraction of CO_2 compared to 10 nm). This behavior, along with other properties of CO_2 as an EOR gas, makes it a good candidate for any improve recovery attempt from smaller—and harder to

access—pores in shale. Such behaviors can influence our interpretation of wettability, as an important factor in analyzing partially wetting droplets and multiphase flow behaviors [110].

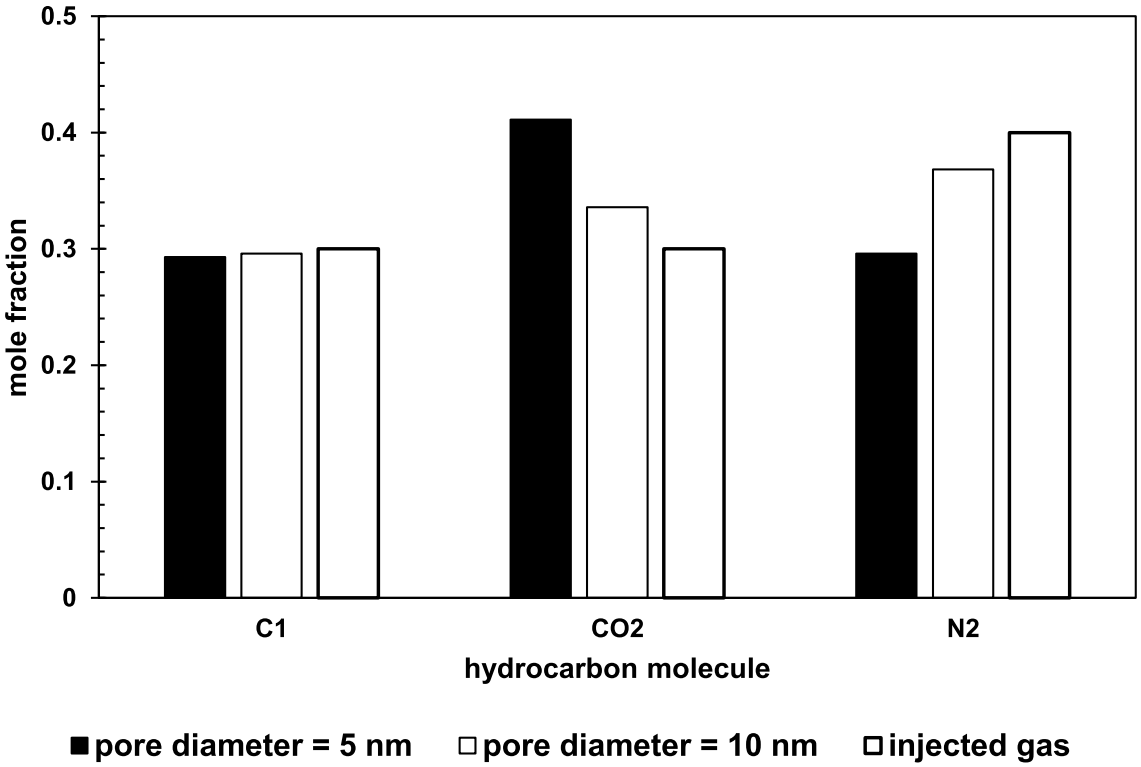

Figure 3.29: This graph shows the composition distribution of the injected gas into the shale, along with the composition in the pores. CO_2 exhibits a better capability of entering small pores and extracting the oil trapped in such a tight media.

Inspired by the results of this section, next chapter discusses a series of core scale and field scale simulations followed by and in–depth discussion to evaluate efficiency of CO_2 injection to improve hydrocarbon recovery from shale, using the multiple porosity model presented in this chapter.

3.8 Conclusion

This chapter provides an in–depth view towards pore size variability and how it can affect hydrocarbon distribution in liquid shale. Based on numerous studies by different authors, it has been shown that the pore diameter in shale reservoirs can vary from a few nanometers, up to micrometers. Pores with small diameters can pose certain steric restrictions to larger hydrocarbon species. As a result, a filtration phenomenon can be observed in which small pores can accommodate lighter hydrocarbons while larger pores do not exhibit any steric hindrance. Such behavior is reported in a number of studies and can influence the producing well stream from liquid shale. In this study, we used the results of some published experimental data to tune the equation of state that is applicable for confined media. The modified equation of state was then used to predict the filtration effect in shale. Our results show that the smaller the pore size, the harder it will be for large hydrocarbons to enter those pores. In other words, oil phase hydrocarbons reside more in the large pores of shale reservoirs while small pores contain mostly gas phase. A triple permeability/porosity model is then presented in this work to account for the presence of small pores, large pores, and fracture network in shale and to incorporate the sieving effect into a real reservoir simulation. Our sensitivity analysis shows that considering the sieving process can explain the commonly observed anomalous gas–oil ratios in liquid shale. The presented model is then tested against a real Eagle Ford case where microseismic data were employed to model the stimulated reservoir volume. Our reservoir model was able to match the oil and gas production data. Additionally, our analysis introduces CO_2 as the best improve recovery option during gas injection as its higher affinity or the wall of organic–rich shale helps CO_2 to penetrate into small and harder–to–access pores.

4. MULTIPLE POROSITY AND IMPROVE RECOVERY FROM SHALE

4.1 Introduction

Recent developments in technology has introduced unconventional low permeability shales as reliable energy sources. Capacity wise, unconventional resources are found to be more abundant than conventional ones. These resources have opened up new challenges and technical difficulties along with this admirable capacity. Low permeability, complicated geology, and reservoir heterogeneity impact liquid recovery in these reservoirs, with ultimate recoveries barely reaching close to double digits during primary recovery mechanisms that are limited to depressurization and solution gas drive [111, 112]. Because of the large scale of unconventional plays, even a very small improvement in ultimate recovery will result in a considerable enhancement in hydrocarbon production. As an example, Hawthorne et al. [113] stated that 1% increase in recovery factor can be translated into 1.6–9 billion barrels of recovered oil from the Bakken formation, North Dakota.

Being able to offer an effective remedy for low recoveries in shale reservoirs requires an extensive knowledge of the difference between reservoir characteristics of conventional and unconventional resources. Same methods will not necessarily result in similar throughputs when applied to conventional and unconventional resources. For example, although water flooding is known to be a popular improve recovery approach in conventional reservoirs with high injectivities, its application in tight reservoirs is quite limited due to a low permeability and lack of injectivity. While not completely resolved, the problem becomes less severe when gases (with a lower viscosity) are used instead. In addition to that, our results from the previous chapter show that the rock/fluid interactions between CO_2 molecules and the tight shale

medium makes CO_2 even a more attractive choice to enhance recovery from shale reservoirs. Gamadi et al. [114, 115] presented experimental works on core plugs from different North American shale plays to evaluate improve recovery from shale using CO_2 or hydrocarbon injection in a cyclic manner. Depending on the injection pressure and the shale core type, they reported 10 to 50% improve recovery as a result of hydrocarbon gas injection and 30 to 70% during CO_2 injection. In addition to that, authors investigated the effect of different factors such as injection pressure and soaking time. The analysis of x–ray computed tomography performed by Tovar et al. [116] revealed a clear oil saturation decrease and CO_2 invasion during shale core experiments of CO_2 improve recovery. The authors observed 20 to 50% improve in hydrocarbon recovery. In addition to the experimental studies, there has been some efforts to simulate CO_2 EOR in shales [117, 118]. However, the problem still remains as conventional approaches are mostly used to address unconventional problems. The multiple porosity model developed in the previous chapter is used in this chapter to analyze CO_2 EOR in shales. Core size samples were simulated first to provide a more clear understanding of the recovery mechanism. The discussion is then continued with some field–scale simulations where the previously developed Eagle Ford model is used to test the performance of the suggested multiple porosity model upon CO_2 injection in shale. Numerical simulations in this chapter are all performed using Halliburton's Nexus Desktop.

4.2 Core experiments simulation

To get a first hand information about the transport mechanism during CO_2 injection and improve our understanding of the new model capabilities, this chapter starts with a core scale simulation case in which CO_2 is injected in a huff–n–puff manner.

4.2.1 Numerical model dimensions

In this section, we model a core experiment in which CO_2 is used to extract oil from a core sample. Figure 4.1 shows a schematic of the experimental setup. as we can see from the graph, CO_2 can enter the core from all sides and we will see a counter current flow of CO_2 and produced oil. The improve recovery process is performed in three stages where CO_2 is firstly injected into the fracture (CO_2 injection and oil production occur only through the fracture network, similar to the actual process in fractured low–permeability reservoirs). During this process, the pressure in the CO_2 filled fracture is kept constant at 3000 psi and we let it soak for 12 hrs before the 12–hr production period starts. A total number of 15 cycles is simulated in our case.

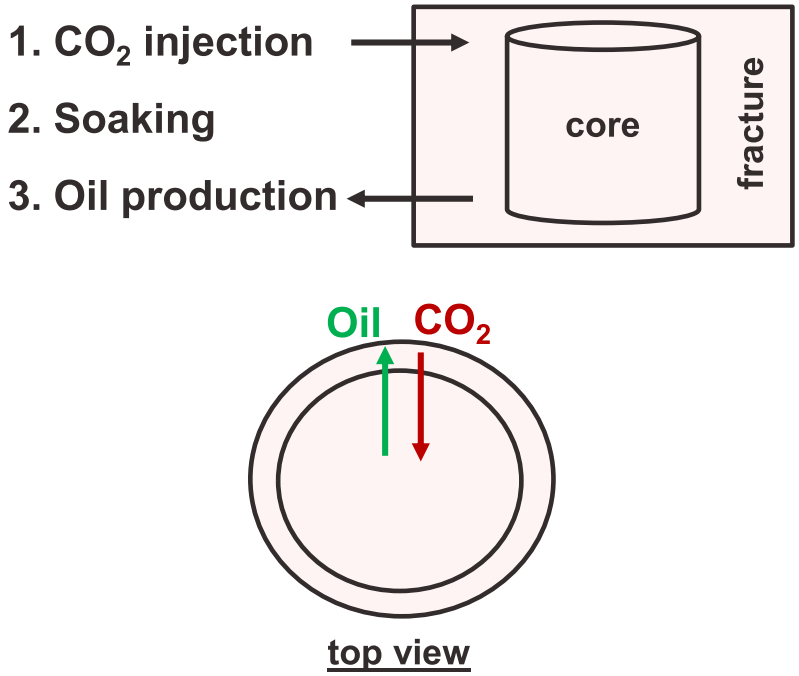

Figure 4.1: Schematic of the numerical model for the multiple–porosity core–scale CO_2 EOR simulation case.

Our model is composed of $21 \times 21 \times 5$ blocks in i, j, and k directions. The grid size is $0.1 \times 0.1 \times 1$ in (x,y,z), which results in a total core diameter of 2 in and length of 5 in. As mentioned earlier, the test is designed in a way that CO_2 invasion occurs only though the sides so there will be a minimum movement in k direction so the grids are coarser in the z direction. The runs are performed in a constant temperature of 212°F and the initial pressure is 3000 psi. During the production period, the fracture pressure is kept at the constant value of 1000 psi. To make the model resembling a more realistic condition, we have considered a heterogeneous distribution of porosity and permeability in the cells. Figure 4.2 shows porosity and permeability histograms in small pores. The average porosity in small pores is considered to be 0.04 with an average permeability of 20 nd. The larger pores have the same porosity, but their permeability is one order of magnitude larger. Figure 4.3 depicts the heterogeneous porosity distribution in the top layer of our core. The composition distribution in large and small pore is similar to the previous chapter with minimum miscibility pressures of 2426 and 2112 psi, respectively.

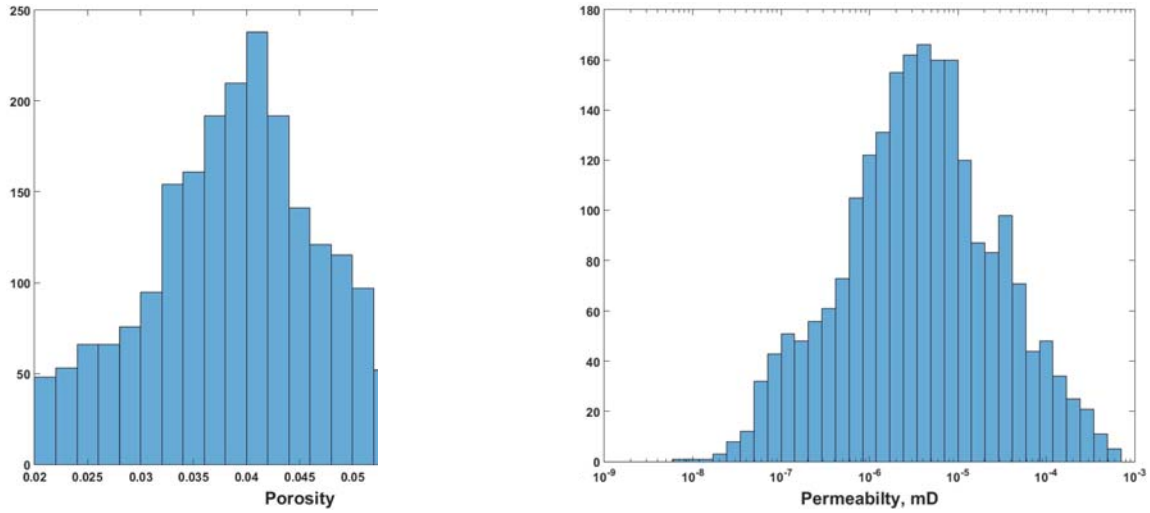

(a) Porosity histogram

(b) Permeability histogram

Figure 4.2: Porosity and permeability histogram of the small pores for the core experiment simulation.

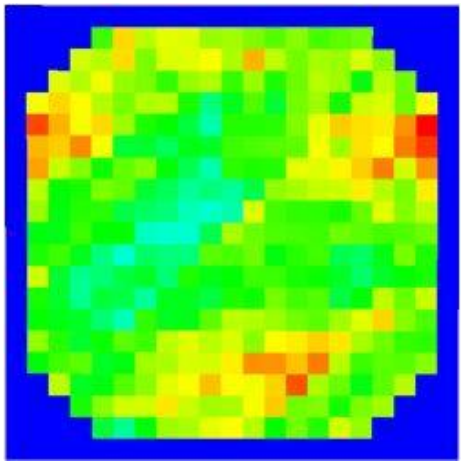

Figure 4.3: Porosity distribution in small pores of the top layer of the core simulation.

4.2.2 Production mechanism

As mentioned before, each experiment consists of a 12–hr injection/soaking period followed by 12 hrs of production. Figure 4.4 shows the molar–based hydrocarbon recovery for the base core simulation. The recovery in this case is calculated by the number of *moles* of produced hydrocarbon divided by total initial moles of hydrocarbon in place (oil and gas production is combined). According to the graph, hydrocarbon production is doubled during the first 5 cycles of CO_2 huff–n–puff. This introduces CO_2 as a potential high–efficiency improve recovery candidate in shale reservoirs. However, it should be mentioned that while a recovery of 0.38 during the primary production period and 0.9 after CO_2 injection are achievable in lab–scale experiments (as also shown by some other authors), one should not expect nearly as close numbers in real field cases as CO_2 has access to just a limited portion of the reservoir. According to the graph, recovery increases by 0.12, 0.08, 0.05, 0.04, and 0.03 for the first 5 cycles. Along side with the recovery analysis, Figure 4.5 shows the oil saturation at the end of each cycle. As evident, CO_2 invades the core from sides and pushes oil out of the core. Figure 4.6 shows the CO_2 concentration in the oil phase at the end of 15th cycle. As we can see, CO_2 takes hydrocarbons out of the oil phase and substitutes them. As production increase from cycle 6 is not considerable, we will focus on the results from the first 5 cycles.

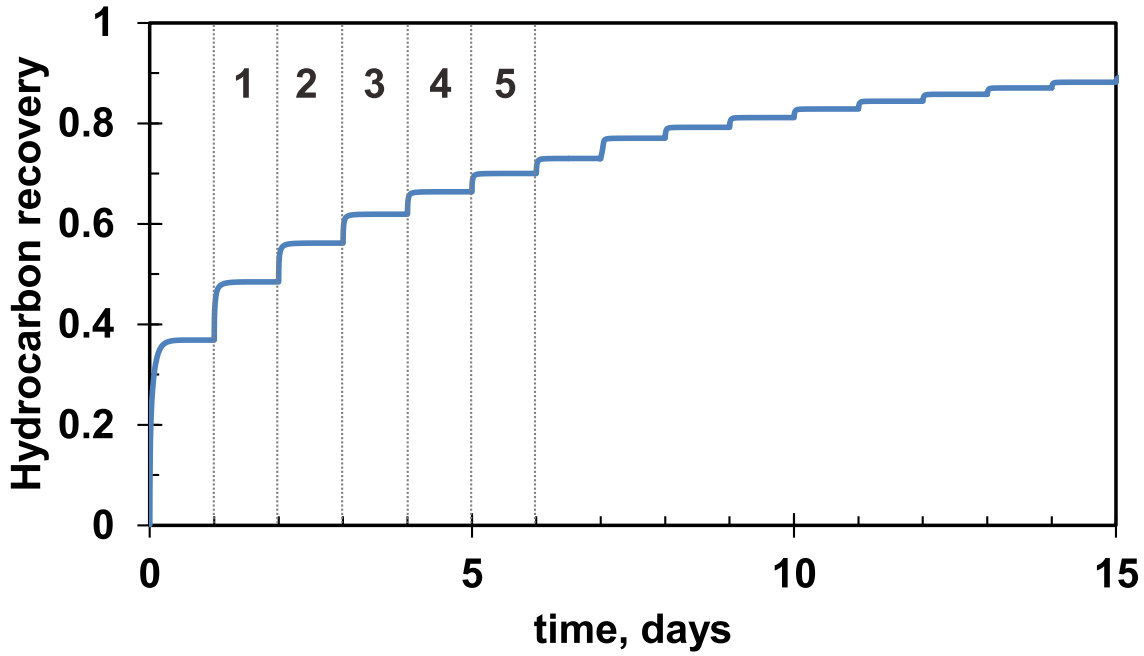

Figure 4.4: Molar–based hydrocarbon recovery shows CO_2 injection can double the initial recovery within the 5th cycle. Such a high recovery has been also reported in some experiments but it is hardly achievable in field scales. Despite core experiments, CO_2's access to oil in field cases is just limited to the fracture network.

To understand the production mechanism Figure 4.7 shows the average molecular weight of the production stream for each cycle. Cycle 0 is the molecular weight of the initial hydrocarbon in place. As we can see, after the first CO_2 cycle, producing stream becomes lighter than the initial composition and becomes heavier as time goes on. Figure 4.8 depicts a detailed composition of the production stream (CH_4 and C_{6+} are selected as the lightest and heaviest species). Along side with what we discussed earlier, this graph shows that CO_2 strips light hydrocarbons out of the oil phase and extracts them out of the core. In fact, what can be interpreted as the "light component stripping" phenomenon adds up to the previously known swelling mechanism to extract oil out of the tight shale using CO_2.

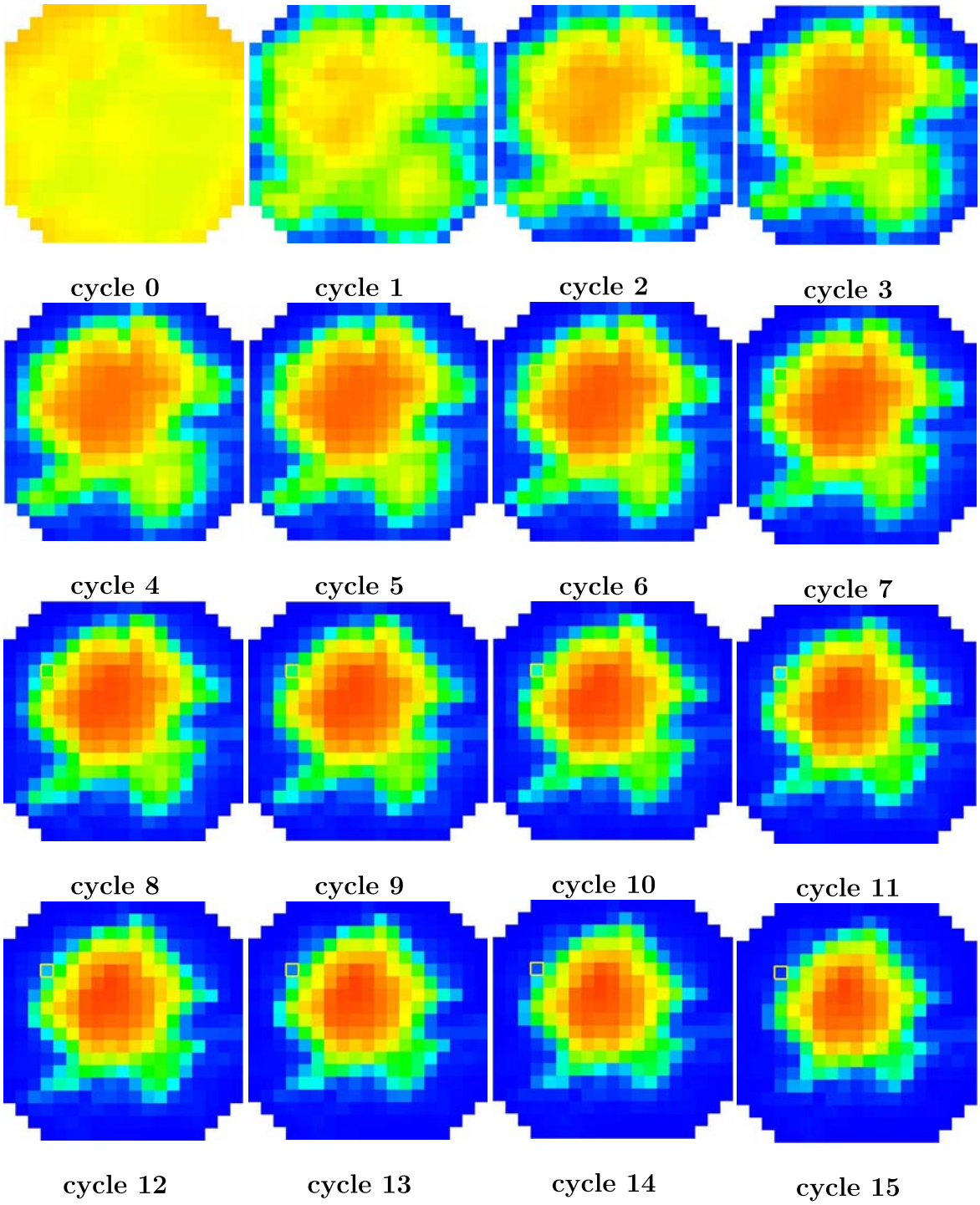

Figure 4.5: Oil saturation at the end of each cycle. Blue and red are the ends of the color bar, representing 0 and 1 for oil saturation, respectively.

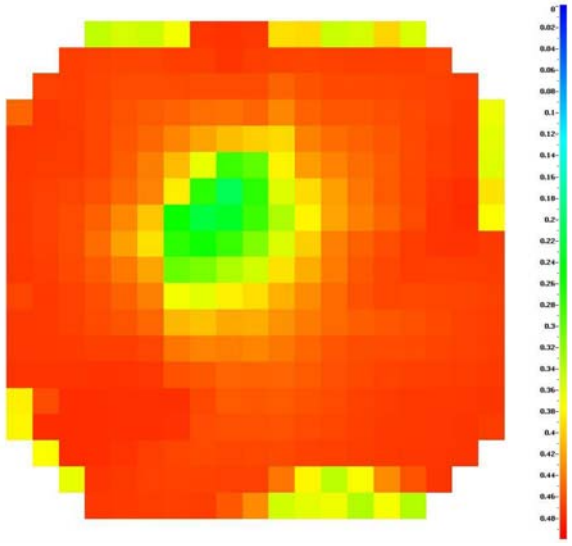

Figure 4.6: CO_2 mole fraction in the oil phase at the end of the 15th cycle shows CO_2 concentrations as high as 50% in the oil phase, meaning that CO_2 takes hydrocarbons out of the oil phase and substitutes them.

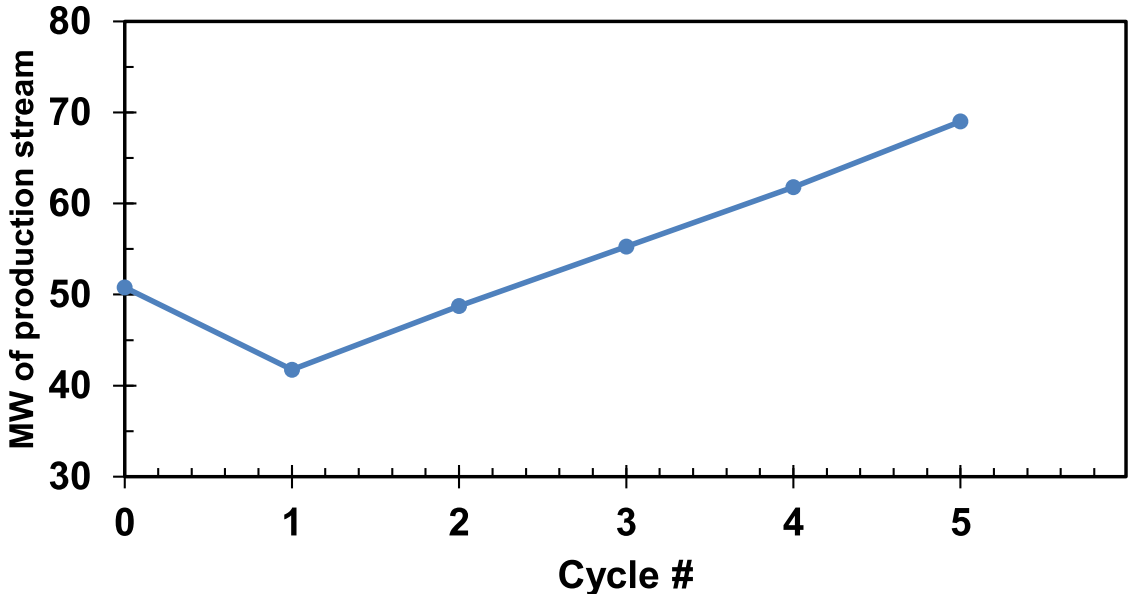

Figure 4.7: The production stream shows that after initial recovery (cycle 0), the produced hydrocarbon becomes very light and it slowly becomes heavier at the later cycles.

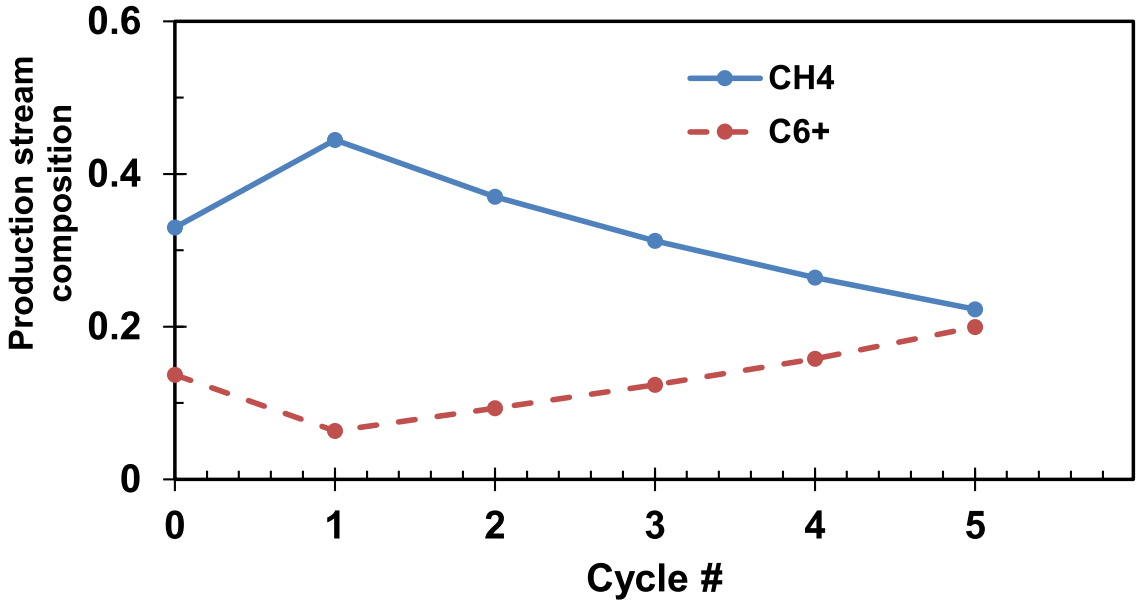

Figure 4.8: Lighter components are extracted by CO_2 sooner than the heavier species.

Figure 4.9 compares two different recovery factors during CO_2 EOR in our case. The solid blue line is the total hydrocarbon recovery (moles of produced hydrocarbon/total models of hydrocarbon in place) and the red dashed line is oil recovery (hydrocarbon recovered at standard condition as oil/total oil in place). As we can see from the graph, when more than 90% of the total hydrocarbon is recovered from the reservoir (at the end of day 15), only 40% of the initial oil in place is recovered as the oil phase in surface. That means although CO_2 increases the oil ultimate recovery, it vaporizes some of the lighter oil components and converts them into the gas phase at surface conditions.

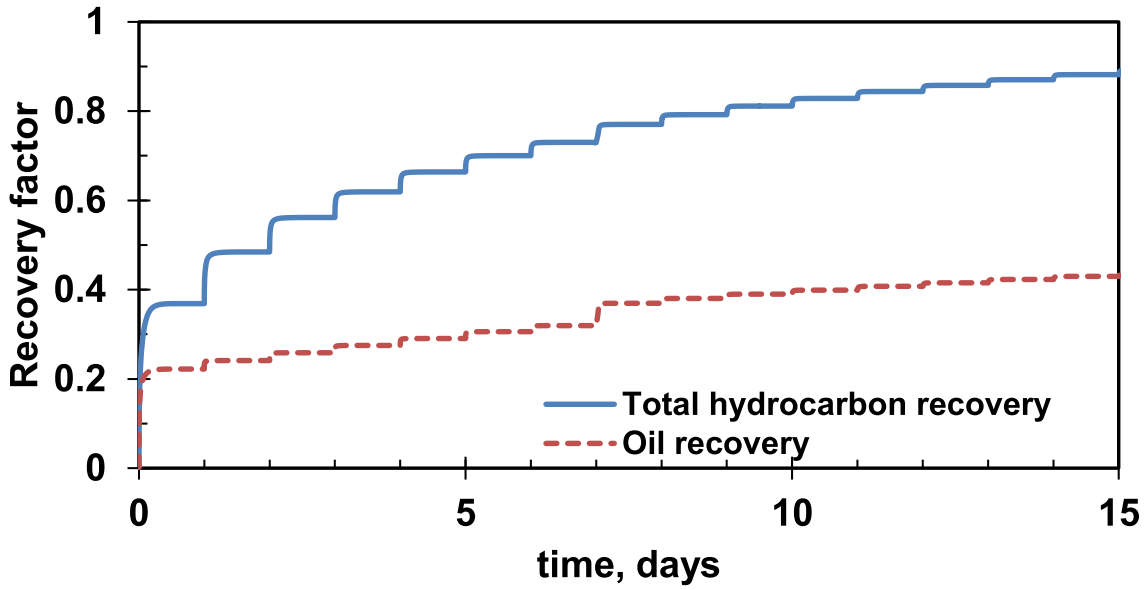

Figure 4.9: The blue line in this graph shows the total hydrocarbon recovery (molar basis) and the red dashed line shows oil recovery. According to the graph, although CO_2 increases the ultimate recovery, it also strips some of oil components out of the oil phase and produces them as separator gas.

4.3 Full field simulation

Core simulation results helped us to get a better understanding of the production mechanism during CO_2 injection. In this section, the Eagle Ford case study from section 3.6.4 is used to evaluate the effectiveness of CO_2 injection as an enhance recovery method upon the newly developed multiple porosity model. The field is assumed to be in production for three years and after that CO_2 is injected into the field in a huff–n–puff manner. Cyclic gas injection could be an efficient technique because it is a single–well process where no well connectivity is required. If fracturing is efficient, the fracture network provides a large contact area for the injected gas to penetrate and diffuse into the low–permeability matrix. The payback period of the cyclic gas injection process is rather short compared with that of the field–

scale flooding process. This makes the single–well cyclic injection process a low–risk process. Injection pressure (9000 psi) is selected to be slightly higher than the initial reservoir pressure (8250 psi). A total of 3 injection cycles were modeled, where each cycle consists 6 months of injection, 6 months of soaking (or well shut–in) followed by 1 year of production. Figure 4.10 shows the cumulative oil production with and without CO_2 injection. As we can see, a 50% increase in oil production is observed after 72 months. As mentioned earlier, this is attributed to the oil swelling as a result of CO_2 dissolution and also the stripping of lighter hydrocarbons by the CO_2 phase.

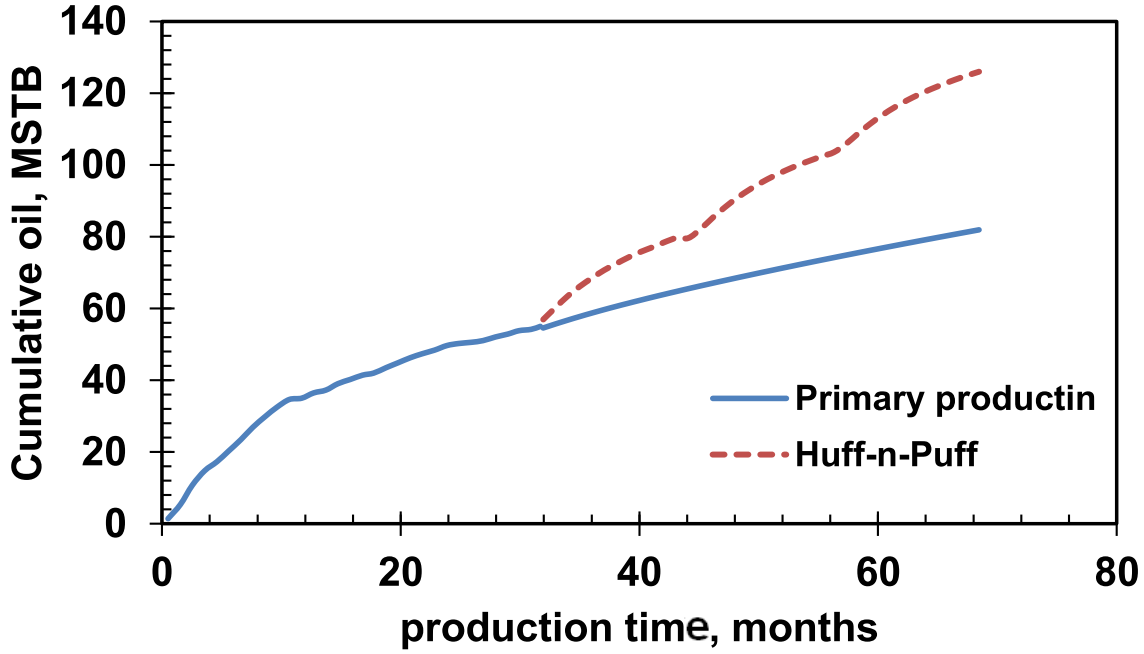

Figure 4.10: As we can see from the graph, CO_2 injection increases ultimate recovery by a factor of 50% after 72 months.

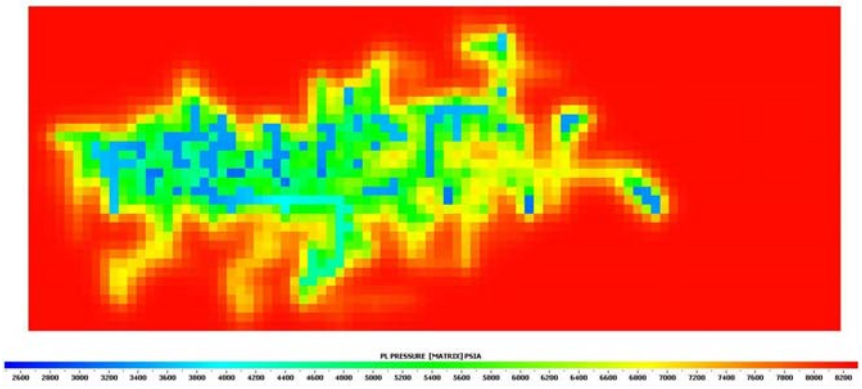

(a) Pressure map before injection

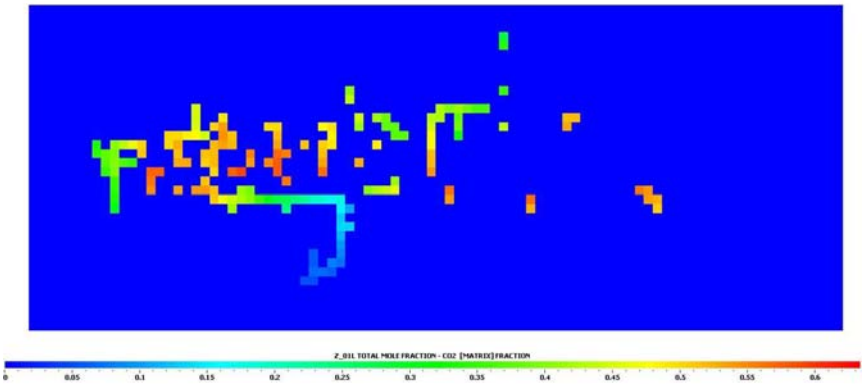

(b) CO_2 concentration map after injection

Figure 4.11: CO_2 concentration map after injection shows CO_2 barely goes far into the reservoir rock and will be mostly concentrated in the vicinity of the fracture network.

Improving the efficiency of CO_2 injection requires a good understanding of the mechanism and effective factors. One part of that is to see how deep CO_2 is able to penetrate into the formation. Figure 4.11a shows the pressure distribution in the formation before CO_2 injection and Figure 4.11b shows CO_2 concentration after EOR. According to the map, CO_2 does not travel deep into the formation even after 3 injection/production cycles. This directs attentions to the well–known problem of low–injectivity in low–permeability shales. To compensate for this limited injectivity,

we should try to maximize the injection fluid exposure to the formation. Such an improvement will be achieved by an efficient fracturing design that generates a more complex network of induced fractures.

To see how operating conditions can impact the ultimate recovery and injection throughput, we have compared the results for cases with 6 months and 18 months soaking time (Figure 4.12). Although not quite significant, we can see longer soaking times slightly increase the ultimate recovery. That is because more CO_2 is able to dissolve into the oil phase and more hydrocarbon is stripped out of the oil phase.

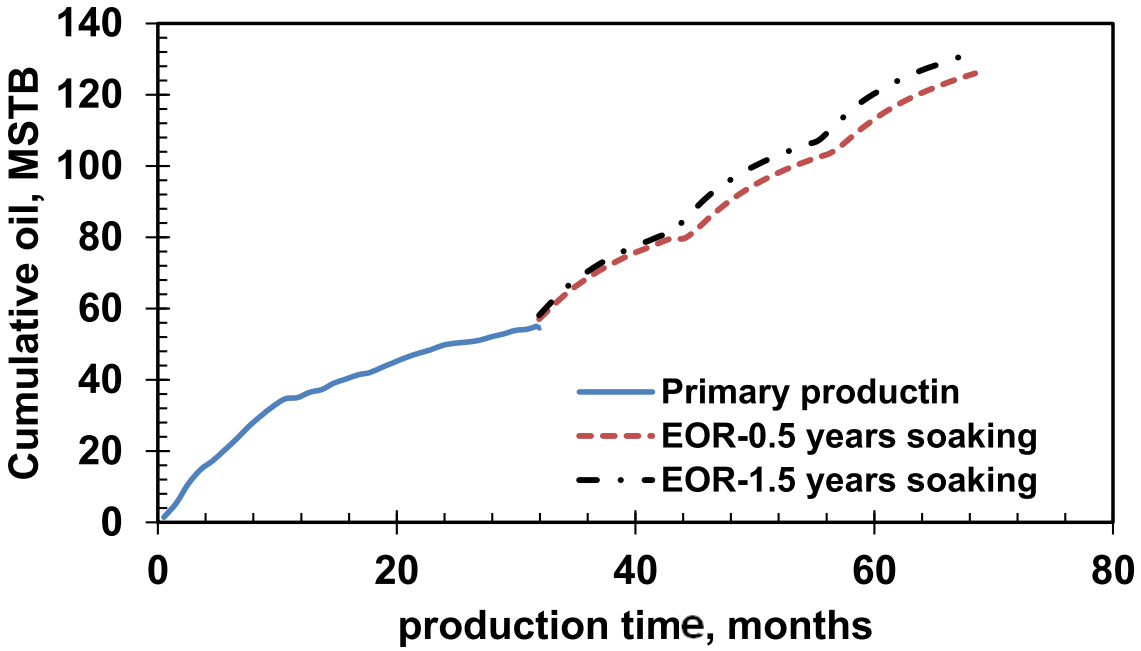

Figure 4.12: Although ultimate recovery increases for longer soaking periods, the increment is not that significant.

4.4 Conclusions

Low hydrocarbon recoveries from liquid–rich shale plays remain to be a challenge to the petroleum industry. One possible remedy to this problem is to apply improve recovery methods. Being able to evaluate performance of different EOR methods in shale requires a model that explains the process dynamics reliably. This chapter tested our proposed multiple porosity model against simulating CO_2 EOR in shale. Core scale simulations show that the relatively high ultimate recovery in core experiments reported by a number of authors can be simulated using the current model. However, these relatively high ultimate recoveries in the core experiments should be treated with cautious as nearly close results cannot be expected in real field examples due to a very limited reservoir exposure to CO_2 and low injectivities. Analysis of the production stream suggests that one major production mechanism is stripping of lighter hydrocarbons from the oil phase into the gas phase by the injected CO_2. Field–scale simulations has proven CO_2 EOR as a viable technique of improving recovery from shale. In addition to that, our results show that an effective fracturing design and a complex fracture network can increase reservoir exposure to CO_2 and boost up the ultimate recovery.

5. SUMMARY AND CONCLUSIONS

In this research, I have used multiple porosity simulation to model fluid flow in heterogeneous shale reservoirs. My research is discussed in three major parts. The first chapter proposes a micro–scale model with a shale subdivision scheme to simulate three phase oil, gas, and water flow in liquid–rich shale. Porous media in shale is divided into three main parts: inorganic matter, kerogen (these two sub–systems form the shale matrix), and fracture network (hydraulic or natural fracture). Each of these subsystems has its own hydraulic, wettability, transport, and storage characteristics. Our micro–scale model provides a very clear picture of water and hydrocarbon interactions and flow behavior in low permeability shale. The second part of this dissertation provides an in–depth view towards pore size variability and how it can affect hydrocarbon distribution in liquid shale. Based on numerous studies by different authors, it has been shown that the pore diameter in shale reservoirs can vary from a few nanometers, up to several micrometers. Our results show that the smaller the pore size, the harder it will be for large hydrocarbons to enter those pores. In other words, oil phase hydrocarbons reside more in the large pores of shale reservoirs while small pores contain mostly gas phase. A triple permeability/porosity model is then presented in this work to account for the presence of small pores, large pores, and fracture network in shale and to incorporate the sieving effect into a commercial reservoir simulator. Our proposed multiple porosity model is then tested against simulating CO_2 EOR in shale. The core scale simulations show that the relatively high ultimate recovery in core experiments reported by a number of authors can be simulated using the current model. However, these relatively high ultimate recoveries in the core experiments should be treated with cautious as nearly

close results cannot be expected in the field examples due to a very limited reservoir exposure to CO_2 and low injectivities. The analysis of the production stream suggests that one major production mechanism is stripping of lighter hydrocarbons from the oil phase into the gas phase by the injected CO_2. Field–scale simulations have proven CO_2 EOR as a viable technique of improving recovery from shale. In addition to that, our results show that an effective fracturing design and a complex fracture network can increase reservoir exposure to CO_2 and improve the ultimate recovery.

REFERENCES

[1] X. Gong, Assessment of Eagle Ford Shale Oil and Gas Resources, Ph.D. dissertation, Texas A&M University (2013). doi:1969.1/151324.

[2] J. D. Edman, J. K. Pitman, Geochemistry of Eagle Ford Group Source Rocks and Oils from the First Shot Field Area, Texas, Gulf Coast Association of Geological Societies Transactions 60 (2010) 217–234.

[3] Y. Tian, Occurrence of Multiple Fluid Phases Across a Basin, in the Same Shale Gas Formation Eagle Ford Shale Example, Ph.D. dissertation (2014). doi:1969.1/152773.

[4] M. E. Curtis, C. H. Sondergeld, R. J. Ambrose, C. S. Rai, Microstructural Investigation of Gas Shales in Two and Three Dimensions Using Nanometer-scale Resolution Imaging, AAPG Bulletin 96 (4) (2012) 665–677. doi:10.1306/08151110188.

[5] M. E. Curtis, R. J. Ambrose, C. H. Sondergeld, Structural Characterization of Gas Shales on the Micro- and Nano-Scales, in: Canadian Unconventional Resources and International Petroleum Conference, Society of Petroleum Engineers, Calgary, Alberta, Canada, 2010. doi:10.2118/137693-MS.

[6] C. H. Sondergeld, R. J. Ambrose, C. S. Rai, J. Moncrieff, Micro-Structural Studies of Gas Shales, in: SPE Unconventional Gas Conference, Society of Petroleum Engineers, Pittsburgh, Pennsylvania, USA, 2010. doi:10.2118/131771-MS.

[7] R. J. Ambrose, R. C. Hartman, M. Diaz Campos, I. Y. Akkutlu, C. Sondergeld, New Pore-scale Considerations for Shale Gas in Place Calculations, in: SPE

Unconventional Gas Conference, Society of Petroleum Engineers, Pittsburgh, Pennsylvania, USA, 2010. doi:10.2118/131772-MS.

[8] D. K. Davies, W. R. Bryant, R. K. Vessell, P. J. Burkett, Porosities, Permeabilities, and Microfabrics of Devonian Shales, Springer, New York, NY, 1991, pp. 109–119. doi:10.1007/978-1-4612-4428-8_10.

[9] R. G. Loucks, R. M. Reed, S. C. Ruppel, D. M. Jarvie, Morphology, Genesis, and Distribution of Nanometer-Scale Pores in Siliceous Mudstones of the Mississippian Barnett Shale, Journal of Sedimentary Research 79 (12). doi:10.2110/jsr.2009.092.

[10] B. Yan, M. Alfi, Y. Wang, J. E. Killough, A New Approach for the Simulation of Fluid Flow in Unconventional Reservoirs Through Multiple Permeability Modeling, in: SPE Annual Technical Conference and Exhibition, Society of Petroleum Engineers, New Orleans, Louisiana, USA, 2013. doi:10.2118/166173-MS.

[11] B. Yan, Y. Wang, J. E. Killough, Beyond Dual-porosity Modeling for the Simulation of Complex Flow Mechanisms in Shale Reservoirs, Computational Geosciences 20 (1) (2016) 69–91. doi:10.1007/s10596-015-9548-x.

[12] M. Alfi, B. Yan, Y. Cao, C. An, Y. Wang, J. He, J. E. Killough, How to Improve our Understanding of Gas and Oil Production Mechanisms in Liquid-rich Shale, in: SPE Annual Technical Conference and Exhibition, Society of Petroleum Engineers, Amsterdam, The Netherlands, 2014. doi:10.2118/170959-MS.

[13] M. Alfi, B. Yan, Y. Cao, Y. Wang, J. E. Killough, J. Killough, Three-Phase Flow Simulation in Ultra-Low Permeability Organic Shale via a Multiple Permeability Approach, in: Unconventional Resources Technology Conference

(URTEC), American Association of Petroleum Geologists, Denver, Colorado, 2014. doi:10.15530/urtec-2014-1895733.

[14] R. G. Loucks, R. M. Reed, S. C. Ruppel, U. Hammes, Spectrum of Pore Types and Networks in Mudrocks and a Descriptive Classification for Matrix-related Mudrock Pores, AAPG Bulletin 96 (6) (2012) 1071–1098. doi:10.1306/08171111061.

[15] U. H. Robert G. Loucks, Robert M. Reed, Stephen C. Ruppel, Preliminary Classification of Matrix Pores in Mudrocks, Gulf Coast Association of Geological Societies Transactions 60 (2010) 435–441.

[16] M. Milner, R. McLin, J. Petriello, Imaging Texture and Porosity in Mudstones and Shales: Comparison of Secondary and Ion-Milled Backscatter SEM Methods, in: Canadian Unconventional Resources and International Petroleum Conference, Society of Petroleum Engineers, Calgary, Alberta, Canada, 2010. doi:10.2118/138975-MS.

[17] J. Lu, K. Milliken, R. M. Reed, S. Hovorka, Diagenesis and Sealing Capacity of the Middle Tuscaloosa Mudstone at the Cranfield Carbon Dioxide Injection Site, Mississippi, U.S.A., Environmental Geosciences 18 (1). doi:https://doi.org/10.1306/eg.09091010015.

[18] B. Yan, J. E. Killough, Y. Wang, Y. Cao, Novel Approaches for the Simulation of Unconventional Reservoirs, in: Unconventional Resources Technology Conference, American Association of Petroleum Geologists, Denver, Colorado, USA, 2013.

[19] B. Yan, A Novel Approach For the Simulation of Multiple Flow Mechanisms and Porosities in Shale Gas Reservoirs, Master's thesis, Texas A&M University (2013). doi:1969.1/151163.

[20] F. P. Wang, R. M. Reed, Pore Networks and Fluid Flow in Gas Shales, in: SPE Annual Technical Conference and Exhibition, Society of Petroleum Engineers, New Orleans, Louisiana, USA, New Orleans, Louisiana, USA, 2009. doi:10.2118/124253-MS.

[21] Q. R. Passey, K. Bohacs, W. L. Esch, R. Klimentidis, S. Sinha, From Oil-Prone Source Rock to Gas-Producing Shale Reservoir - Geologic and Petrophysical Characterization of Unconventional Shale Gas Reservoirs, in: International Oil and Gas Conference and Exhibition in China, Society of Petroleum Engineers, Beijing, China, 2010. doi:10.2118/131350-MS.

[22] S. J. Dueppenbecker, D. H. Welte, Petroleum Expulsion from Source Rocks-Insights from Geology, Geochemistry and Computerized Numerical Modelling, in: 13th World Petroleum Congress, World Petroleum Congress, Buenos Aires, Argentina, 1991.

[23] E. Rylander, P. Singer, T. Jiang, R. Lewis, R. H. Mclin, S. Sinclair, NMR T2 Distributions in the Eagle Ford Shale: Reflections on Pore Size, in: SPE Unconventional Resources Conference, Society of Petroleum Engineers, The Woodlands, Texas, USA, 2013. doi:10.2118/164554-MS.

[24] B. Rahmani Didar, I. Akkutlu, Pore-Size Dependence of Fluid Phase Behavior and the Impact on Shale Gas Reserves, in: Unconventional Resources Technology Conference, Denver, Colorado, USA, Society of Exploration Geophysicists, American Association of Petroleum Geologists, Society of Petroleum Engineers, 2013, pp. 1793–1814. doi:10.1190/urtec2013-183.

[25] B. Rahmani Didar, I. Y. Akkutlu, Pore-size Dependence of Fluid Phase Behavior and Properties in Organic-Rich Shale Reservoirs, in: SPE International

Symposium on Oilfield Chemistry, Society of Petroleum Engineers, The Woodlands, Texas, USA, 2013. doi:10.2118/164099-MS.

[26] S. A. Schaaf, P. L. Chambre, Flow of Rarefied Gases, Princeton University Press, Princeton, 1961.

[27] S. Roy, R. Raju, H. F. Chuang, B. A. Cruden, M. Meyyappan, Modeling Gas Flow Through Microchannels and Nanopores, Journal of Applied Physics 93 (8) (2003) 4870–4879. doi:10.1063/1.1559936.

[28] S. P. Mahulikar, H. Herwig, O. Hausner, Study of Gas Microconvection for Synthesis of Rarefaction and Nonrarefaction Effects, Journal of Microelectromechanical Systems 16 (6) (2007) 1543–1556. doi:10.1109/JMEMS.2007.908434.

[29] A. Beskok, G. E. Karniadakis, G. Karniadakis, A Model for Flows in Channels, Pipes, and Ducts at Micro and Nano Scales, Microscale Thermophysical Engineering 3 (1). doi:10.1080/108939599199864.

[30] F. Civan, Effective Correlation of Apparent Gas Permeability in Tight Porous Media, Transport in Porous Media 82 (2) (2010) 375–384. doi:10.1007/s11242-009-9432-z.

[31] F. Javadpour, Nanopores and Apparent Permeability of Gas Flow in Mudrocks (Shales and Siltstone), Journal of Canadian Petroleum Technology 48 (08) (2009) 16–21. doi:10.2118/09-08-16-DA.

[32] F. Javadpour, D. Fisher, M. Unsworth, Nanoscale Gas Flow in Shale Gas Sediments, Journal of Canadian Petroleum Technology 46 (10). doi:10.2118/07-10-06.

[33] A. Sakhaee-Pour, S. Bryant, Gas Permeability of Shale, SPE Reservoir Evaluation & Engineering 15 (04) (2012) 401–409. doi:10.2118/146944-PA.

[34] N. Dongari, Y. Zhang, J. M. Reese, Modeling of Knudsen Layer Effects in Micro/Nanoscale Gas Flows, Journal of Fluids Engineering 133 (7) (2011) 071101. doi:10.1115/1.4004364.

[35] J. A. V. Butler, C. Ockrent, Studies in Electrocapillarity. III, The Journal of Physical Chemistry 34 (12) (1929) 2841–2859. doi:10.1021/j150318a015.

[36] I. Langmuir, The Constitution and Fundamental Properties of Solids and Liquids. Part 2. Liquids, Journal of the American Chemical Society 38 (11) (1916) 2221–2295. doi:10.1021/ja02268a002.

[37] D. Peng, D. B. Robinson, A New Two-Constant Equation of State, Industrial & Engineering Chemistry Fundamentals 15 (1) (1976) 59–64. doi:10.1021/i160057a011.

[38] T. N. Narasimhan, P. A. Witherspoon, An Integrated Finite Difference Method for Analyzing Fluid Flow in Porous Media, Water Resources Research 12 (1) (1976) 57–64. doi:10.1029/WR012i001p00057.

[39] R. Brooks, A. Corey, Hydraulic Properties of Porous Media, Hydrology Papers 3 (0) (1964) 1–27.

[40] K. Aziz, A. Settari, Petroleum Reservoir Simulation, Applied Science Publishers, London, 1979.

[41] J. M. Dacy, Core Tests for Relative Permeability of Unconventional Gas Reservoirs, in: SPE Annual Technical Conference and Exhibition, Society of Petroleum Engineers, Florence, Italy, 2010. doi:10.2118/135427-MS.

[42] H. Luo, X. Wang, Oil Displacement for One-Dimensional Three-Phase Flow with Phase Change in Fractured Media, Transport in Porous Media 79 (3) (2009) 377–392. doi:10.1007/s11242-008-9325-6.

[43] P. H. Nelson, Pore-throat Sizes in Sandstones, Tight Sandstones, and Shales, AAPG Bulletin 93 (3) (2009) 329–340. doi:10.1306/10240808059.

[44] F. P. Wang, R. M. Reed, Pore Networks and Fluid Flow in Gas Shales, in: SPE Annual Technical Conference and Exhibition, Society of Petroleum Engineers, New Orleans, Louisiana, USA, 2009. doi:10.2118/124253-MS.

[45] K. Bjørlykke, Petroleum Geoscience: From Sedimentary Environments to Rock Physics, Springer, Berlin, 2015.

[46] J. Hunt, Distribution of Hydrocarbons in Sedimentary Rocks, Geochimica et Cosmochimica Acta 22 (1) (1961) 37–49. doi:10.1016/0016-7037(61)90071-0.

[47] J. M. Hunt, G. W. Jamieson, Oil and Organic Matter in Source Rocks of Petroleum, AAPG Bulletin 40 (3) (1956) 477–488.

[48] M. Wang, J. Yang, Z. Wang, S. Lu, Nanometer-Scale Pore Characteristics of Lacustrine Shale, Songliao Basin, NE China., PloS one 10 (8). doi:10.1371/journal.pone.0135252.

[49] T. Zhang, X. Sun, S. C. Ruppel, Hydrocarbon Geochemistry and Pore Characterization of Bakken Formation and Implication to Oil Migration and Oil Saturation, in: AAPG Annual Convention and Exhibition, Pittsburgh, Pennsylvania, 2013.

[50] T. Zhang, Xun Sun, Kitty L. Milliken, Stephen C. Ruppel, Pore Characterization of Eagle Ford Shales by N2 Adsorption and Desorption Isotherms and Pore Evolution in Organic Matter During Thermal Maturation, in: AAPG Annual Convention and Exhibition, Houston, TX, 2014.

[51] C. Zou, X. Jin, R. Zhu, G. Gong, L. Sun, J. Dai, D. Meng, X. Wang, J. Li, S. Wu, X. Liu, J. Wu, L. Jiang, Do Shale Pore Throats Have a Threshold Diam-

eter for Oil Storage?, Scientific Reports 5 (2015) 13619. doi:10.1038/srep13619.

[52] F. Geren, T. Firincioglu, C. Karacaer, E. Ozkan, C. Ozgen, Modeling Flow in Nanoporous, Membrane Reservoirs and Interpretation of Coupled Fluxes, in: SPE Annual Technical Conference and Exhibition, Society of Petroleum Engineers, Amsterdam, The Netherlands, 2014. doi:10.2118/170976-MS.

[53] M. Firouzi, E. C. Rupp, C. W. Liu, J. Wilcox, Molecular Simulation and Experimental Characterization of the Nanoporous Structures of Coal and Gas Shale, International Journal of Coal Geology 121 (2014) 123–128. doi:10.1016/j.coal.2013.11.003.

[54] S. Farhadi Nia, D. Dasani, T. Tsotsis, K. Jessen, Pore-Scale Characterization of Oil-Rich Monterey Shale: A Preliminary Study, in: Unconventional Resources Technology Conference, Society of Exploration Geophysicists, American Association of Petroleum Geologists, Society of Petroleum Engineers, Denver, Colorado, USA, 2013, pp. 1750–1760. doi:10.1190/urtec2013-178.

[55] G. R. Chalmers, R. M. Bustin, I. M. Power, Characterization of Gas Shale Pore Systems by Porosimetry, Pycnometry, Surface Area, and Field Emission Scanning Electron Microscopy/Transmission Electron Microscopy Image Analyses: Examples from the Barnett, Woodford, Haynesville, Marcellus, and Doig units, AAPG Bulletin 96 (6) (2012) 1099–1119.

[56] G. Chalmers, R. M. Bustin, I. Power, The Importance of Meso-and Microporosity in Shale Gas Capacity, in: AAPG Annual Convention and Exhibition, Denver, Colorado, 2009.

[57] C. R. Clarkson, J. L. Jensen, T. Blasingame, Reservoir Engineering for Unconventional Reservoirs: What Do We Have to Consider?, in: North American

Unconventional Gas Conference and Exhibition, Society of Petroleum Engineers, The Woodlands, Texas, USA, 2011. doi:10.2118/145080-MS.

[58] R. M. Bustin, A. M. Bustin, A. Cui, D. Ross, V. M. Pathi, Impact of Shale Properties on Pore Structure and Storage Characteristics, in: SPE Shale Gas Production Conference, Society of Petroleum Engineers, Fort Worth, Texas, USA, 2008. doi:10.2118/119892-MS.

[59] Q. Hu, S. Dultz, S. Hamamoto, R. P. Ewing, Multiple Approaches to Characterizing Pore Structure in Natural Rock, in: American Geophysical Union, Fall Meeting 2012, abstract #H41L-04, 2012.

[60] U. Kuila, M. Prasad, Specific Surface Area and Pore-size Distribution in Clays and Shales, Geophysical Prospecting 61 (2) (2013) 341–362. doi:10.1111/1365-2478.12028.

[61] M. Alfi, C. An, Y. Cao, B. Yan, M. A. Barrufet, J. E. Killough, Pore Size Variability and Sieving Effect in Liquid Shale-A Multiple Permeability Approach and Eagle Ford Case Study, in: SPE Reservoir Simulation Conference, Society of Petroleum Engineers, Montgomery, Texas, USA, 2017. doi:10.2118/182643-MS.

[62] R. M. Bustin, A. Bustin, D. Ross, G. Chalmers, V. Murthy, C. Laxmi, X. Cui, Shale Gas Opportunities and Challenges, in: Search and Discovery Articles #40382, San Antonio, 2008.

[63] G. R. L. Chalmers, R. M. Bustin, Light Volatile Liquid and Gas Shale Reservoir Potential of the Cretaceous Shaftesbury Formation in Northeastern British Columbia, Canada, AAPG Bulletin 96 (7) (2012) 1333–1367. doi:10.1306/10041111041.

[64] J. Schieber, Common Themes in the Formation and Preservation of Intrinsic Porosity in Shales and Mudstones - Illustrated with Examples Across the Phanerozoic, in: SPE Unconventional Gas Conference, Society of Petroleum Engineers, Pittsburgh, Pennsylvania, USA, 2010. doi:10.2118/132370-MS.

[65] X. Tang, Z. Jiang, Z. Li, Z. Gao, Y. Bai, S. Zhao, J. Feng, The Effect of the Variation in Material Composition on the Heterogeneous Pore Structure of High-maturity Shale of the Silurian Longmaxi Formation in the Southeastern Sichuan Basin, China, Journal of Natural Gas Science and Engineering 23 (2015) 464–473. doi:10.1016/j.jngse.2015.02.031.

[66] H. Tian, L. Pan, X. Xiao, R. W. Wilkins, Z. Meng, B. Huang, A Preliminary Study on the Pore Characterization of Lower Silurian Black Shales in the Chuandong Thrust Fold Belt, Southwestern China Using Low Pressure N2 Adsorption and FE-SEM Methods, Marine and Petroleum Geology 48 (2013) 8–19. doi:10.1016/j.marpetgeo.2013.07.008.

[67] D. J. Ross, R. M. Bustin, The Importance of Shale Composition and Pore Structure upon Gas Storage Potential of Shale Gas Reservoirs, Marine and Petroleum Geology 26 (6) (2009) 916–927. doi:10.1016/j.marpetgeo.2008.06.004.

[68] S. Badre, C. Carla Goncalves, K. Norinaga, G. Gustavson, O. C. Mullins, Molecular Size and Weight of Asphaltene and Asphaltene Solubility Fractions from Coals, Crude Oils and Bitumen, Fuel 85 (1) (2006) 1–11. doi:10.1016/j.fuel.2005.05.021.

[69] H. Groenzin, O. C. Mullins, Molecular Size and Structure of Asphaltenes from Various Sources, Energy Fuels 14 (3) (2000) 677–684. doi:10.1021/EF990225Z.

[70] D. W. Sundstrom, F. G. Krautz, Equilibrium Adsorption of Liquid Phase Normal Paraffins on Type 5A Molecular Sieves, Journal of Chemical & Engineering Data 13 (2) (1968) 223–226. doi:10.1021/je60037a026.

[71] J. A. M. Alkandary, R. Al-Ammeri, A. B. S. H. Salem, Adsorption Equilibria of Normal Paraffins on 5A Molecular Sieve, Separation Science and Technology 30 (16) (1995) 3195–3209. doi:10.1080/01496399508013138.

[72] Á. Berenguer-Murcia, A. J. Fletcher, J. García-Martínez, D. Cazorla-Amorós, Á. Linares-Solano, K. M. Thomas, Probe Molecule Kinetic Studies of Adsorption on MCM-41, The Journal of Physical Chemistry B 107 (4) (2003) 1012–1020. doi:10.1021/JP026764D.

[73] D. W. Breck, Crystalline Molecular Sieves, Journal of Chemical Education 41 (12) (1964) 678. doi:10.1021/ed041p678.

[74] L. J. Dunne, G. Manos (Eds.), Adsorption and Phase Behaviour in Nanochannels and Nanotubes, Springer Netherlands, Dordrecht, 2010. doi:10.1007/978-90-481-2481-7.

[75] M. Alfi, H. Nasrabadi, D. Banerjee, Experimental Investigation of Confinement Effect on Phase Behavior of Hexane, Heptane and Octane Using Lab-on-a-chip Technology, Fluid Phase Equilibria 423 (2016) 25–33. doi:10.1016/j.fluid.2016.04.017.

[76] M. Alfi, D. Banerjee, H. Nasrabadi, Effect of Confinement on the Dynamic Contact Angle of Hydrocarbons, Energy & Fuels 30 (11) (2016) 8962–8967. doi:10.1021/acs.energyfuels.6b01450.

[77] M. Alfi, H. Nasrabadi, D. Banerjee, Confinement Effects on Phase Behavior of Hydrocarbon in Nanochannels, in: ASME 2015 International Mechanical

Engineering Congress and Exposition, ASME, Houston, Texas, USA, 2015, p. V07BT09A010. doi:10.1115/IMECE2015-52845.

[78] S. Luo, H. Nasrabadi, J. L. Lutkenhaus, Effect of Confinement on the Bubble Points of Hydrocarbons in Nanoporous Media, AIChE Journal 62 (5) (2016) 1772–1780. doi:10.1002/aic.15154.

[79] M. Alfi, H. Nasrabadi, D. Banerjee, Effect of Confinement on Bubble Point Temperature Shift of Hydrocarbon Mixtures: Experimental Investigation Using Nanofluidic Devices, in: SPE Annual Technical Conference and Exhibition, Society of Petroleum Engineers, San Antonio, Texas, USA, 2017. doi:10.2118/187057-MS.

[80] B. Nojabaei, R. T. Johns, L. Chu, Effect of Capillary Pressure on Fluid Density and Phase Behavior in Tight Rocks and Shales, in: SPE Annual Technical Conference and Exhibition, Society of Petroleum Engineers, San Antonio, Texas, USA, 2012. doi:10.2118/159258-MS.

[81] A. Sanaei, A. Jamili, J. Callard, Effect of Pore Size Distribution and Connectivity on Phase Behavior and Gas Condensate Production From Unconventional Resources, in: SPE Unconventional Resources Conference, Society of Petroleum Engineers, The Woodlands, Texas, USA, 2014. doi:10.2118/168970-MS.

[82] A. Sanaei, A. Jamili, J. Callard, A. Mathur, Production Modeling in the Eagle Ford Gas Condensate Window: Integrating New Relationships between Core Permeability, Pore Size, and Confined PVT Properties, in: SPE Western North American and Rocky Mountain Joint Meeting, Society of Petroleum Engineers, Denver, Colorado, 2014. doi:10.2118/169493-MS.

[83] A. A. Shapiro, E. H. Stenby, Thermodynamics of the Multicomponent Vaporliquid Equilibrium under Capillary Pressure Difference, Fluid Phase Equilibria 178 (1) (2001) 17–32. doi:10.1016/S0378-3812(00)00403-9.

[84] B. C. Stimpson, M. A. Barrufet, Thermodynamic Modeling of Pure Components Including the Effects of Capillarity, Journal of Chemical & Engineering Data 61 (8) (2016) 2844–2850. doi:10.1021/acs.jced.6b00188.

[85] B. C. Stimpson, M. A. Barrufet, Effects of Confined Space on Production from Tight Reservoirs, in: SPE Annual Technical Conference and Exhibition, Society of Petroleum Engineers, Dubai, UAE, 2016. doi:10.2118/181686-MS.

[86] T. W. Teklu, N. Alharthy, H. Kazemi, X. Yin, R. M. Graves, A. M. AlSumaiti, Phase Behavior and Minimum Miscibility Pressure in Nanopores, SPE Reservoir Evaluation & Engineering 17 (03) (2014) 396–403. doi:10.2118/168865-PA.

[87] T. Pitakbunkate, P. B. Balbuena, G. J. Moridis, T. A. Blasingame, Effect of Confinement on Pressure/Volume/Temperature Properties of Hydrocarbons in Shale Reservoirs, SPE Journal 21 (02) (2016) 621–634. doi:10.2118/170685-PA.

[88] T. W. Rosch, J. R. Errington, Phase Behavior of Model Confined Fluids. Influence of SubstrateFluid Interaction Strength, The Journal of Physical Chemistry B 112 (47) (2008) 14911–14919. doi:10.1021/jp804419b.

[89] L. Travalloni, M. Castier, F. W. Tavares, S. I. Sandler, Thermodynamic Modeling of Confined Fluids Using an Extension of the Generalized van der Waals Theory, Chemical Engineering Science 65 (10) (2010) 3088–3099. doi:10.1016/j.ces.2010.01.032.

[90] L. Travalloni, M. Castier, F. W. Tavares, Phase Equilibrium of Fluids Confined in Porous Media from an Extended Peng Robinson Equation of State, Fluid

Phase Equilibria 362 (2014) 335–341. doi:10.1016/j.fluid.2013.10.049.

[91] C. G. V. Burgess, R. H. E. Duffett, G. J. Minkoff, R. G. Taylor, Sorption of Long Chain Normal Paraffins in Molecular Sieves, Journal of Applied Chemistry 14 (8) (2007) 350–360. doi:10.1002/jctb.5010140807.

[92] A. J. Fletcher, K. M. Thomas, Adsorption and Desorption Kinetics of n-Octane and n-Nonane Vapors on Activated Carbon, Langmuir 15 (20) (1999) 6908–6914. doi:10.1021/LA9814992.

[93] F. Miano, Adsorption of Hydrocarbon Vapour Mixtures onto Zeolite 5A, Colloids and Surfaces A: Physicochemical and Engineering Aspects 110 (1) (1996) 95–104. doi:10.1016/0927-7757(95)03439-0.

[94] T. Nakahara, M. Hirata, T. Omori, Adsorption of Hydrocarbons on a Carbon Molecular Sieve, Journal of Chemical & Engineering Data 19 (4) (1974) 310–313. doi:10.1021/je60063a018.

[95] A. D. Soule, C. A. Smith, X. Yang, C. T. Lira, Adsorption Modeling with the ESD Equation of State, Langmuir 17 (2001) 2950–2957. doi:10.1021/la000311n.

[96] R. K. Gupta, D. Kunzru, D. N. Saraf, Liquid-phase Adsorption of n-Paraffins on Molecular Sieve, Journal of Chemical & Engineering Data 25 (1) (1980) 14–16. doi:10.1021/je60084a009.

[97] M. M. Dubinin, M. M. Vishnyakova, E. D. Zaverina, E. G. Zhukovskaya, E. A. Leont'ev, V. M. Luk'yanovich, A. I. Sarakhov, Adsorption Properties and Secondary Porous Structure of Adsorbents with a Molecular Sieve Action, Bulletin of the Academy of Sciences of the USSR Division of Chemical Science 10 (3) (1961) 368–375. doi:10.1007/BF01131050.

[98] M. Alfi, B. Yan, Y. Cao, C. An, Y. Wang, J. He, J. E. Killough, How to Improve our Understanding of Gas and Oil Production Mechanisms in Liquid-rich Shale, in: SPE Annual Technical Conference and Exhibition, Society of Petroleum Engineers, Amsterdam, The Netherlands, Amsterdam, The Netherlands, 2014. doi:10.2118/170959-MS.

[99] M. Alfi, B. Yan, Y. Cao, C. An, J. E. Killough, M. A. Barrufet, Microscale Porosity Models as Powerful Tools to Analyze Hydrocarbon Production Mechanisms in Liquid Shale, Journal of Natural Gas Science and Engineering 26 (2015) 1495–1505. doi:10.1016/j.jngse.2015.08.002.

[100] B. Yan, M. Alfi, Y. Cao, C. An, Y. Wang, J. E. Killough, Advanced Multiple Porosity Model for Fractured Reservoirs, in: IPTC, International Petroleum Technology Conference, Doha, Qatar, 2015. doi:10.2523/IPTC-18308-MS.

[101] B. Yan, M. Alfi, C. An, Y. Cao, Y. Wang, J. E. Killough, General Multi-Porosity Simulation for Fractured Reservoir Modeling, Journal of Natural Gas Science and Engineering 33 (2016) 777–791. doi:10.1016/j.jngse.2016.06.016.

[102] B. Yan, M. Alfi, Y. Wang, J. E. Killough, A New Approach for the Simulation of Fluid Flow in Unconventional Reservoirs Through Multiple Permeability Modeling, in: SPE Annual Technical Conference and Exhibition, Society of Petroleum Engineers, New Orleans, Louisiana, USA, 2013. doi:10.2118/166173-MS.

[103] M. Alfi, Z. Chai, B. Yan, B. Stimpson, M. Barrufet, J. Killough, Advances in Simulation of Hydrocarbon Production from Shale Reservoirs, in: Unconventional Resources Technology Conference, Austin, Texas, USA, 2017. doi:10.15530/URTEC-2017-2669950.

[104] R. Hinkley, Z. Gu, T. Wong, D. Camilleri, Multi-Porosity Simulation of Unconventional Reservoirs, in: SPE Unconventional Resources Conference Canada, Society of Petroleum Engineers, Calgary, Alberta, Canada, 2013. doi:10.2118/167146-MS.

[105] A. F. Ismail, K. Chandra Khulbe, T. Matsuura, Gas Separation Membranes, Springer International Publishing, Cham, 2015. doi:10.1007/978-3-319-01095-3.

[106] F. Dreisbach, R. Staudt, J. Keller, High Pressure Adsorption Data of Methane, Nitrogen, Carbon Dioxide and Their Binary and Ternary Mixtures on Activated Carbon, Adsorption 5 (3) (1999) 215–227. doi:10.1023/A:1008914703884.

[107] H. Jüntgen, New Applications for Carbonaceous Adsorbents, Carbon 15 (5) (1977) 273–283. doi:10.1016/0008-6223(77)90030-6.

[108] M. de la Casa-Lillo, J. Alcañiz-Monge, E. Raymundo-Piñero, D. Cazorla-Amorós, A. Linares-Solano, Molecular Sieve Properties of General-purpose Carbon Fibers, Carbon 36 (9) (1998) 1353–1360. doi:10.1016/S0008-6223(98)00120-1.

[109] S. Himeno, T. Komatsu, S. Fujita, High-Pressure Adsorption Equilibria of Methane and Carbon Dioxide on Several Activated Carbons, Journal of Chemical & Engineering Data 50 (2). doi:10.1021/JE049786X.

[110] A. Hooshanginejad, S. Lee, Droplet Depinning in a Wake, Physical Review Fluids 2 (3) (2017) 031601. doi:10.1103/PhysRevFluids.2.031601.

[111] A. J. Clark, Determination of Recovery Factor in the Bakken Formation, Mountrail County, ND, in: SPE Annual Technical Conference and Exhibi-

tion, Society of Petroleum Engineers, New Orleans, Louisiana, USA, 2009. doi:10.2118/133719-STU.

[112] G. Liu, J. Sorensen, J. Braunberger, R. Klenner, J. Ge, C. Gorecki, E. Steadman, J. Harju, CO2-Based Enhanced Oil Recovery from Unconventional Reservoirs: A Case Study of the Bakken Formation, in: SPE Unconventional Resources Conference, Society of Petroleum Engineers, The Woodlands, Texas, USA, 2014. doi:10.2118/168979-MS.

[113] S. B. Hawthorne, C. D. Gorecki, J. A. Sorensen, E. N. Steadman, J. A. Harju, S. Melzer, Hydrocarbon Mobilization Mechanisms from Upper, Middle, and Lower Bakken Reservoir Rocks Exposed to CO, in: SPE Unconventional Resources Conference Canada, Society of Petroleum Engineers, Calgary, Alberta, Canada, 2013. doi:10.2118/167200-MS.

[114] T. Gamadi, J. Sheng, M. Soliman, An Experimental Study of Cyclic Gas Injection to Improve Shale Oil Recovery, in: SPE Annual Technical Conference and Exhibition, Society of Petroleum Engineers, New Orleans, Louisiana, USA, 2013. doi:10.2118/166334-MS.

[115] T. Gamadi, J. Sheng, M. Soliman, H. Menouar, M. Watson, H. Emadibaladehi, An Experimental Study of Cyclic CO2 Injection to Improve Shale Oil Recovery, in: SPE Improved Oil Recovery Symposium, Society of Petroleum Engineers, Tulsa, Oklahoma, USA, 2014. doi:10.2118/169142-MS.

[116] F. D. Tovar, O. Eide, A. Graue, D. S. Schechter, Experimental Investigation of Enhanced Recovery in Unconventional Liquid Reservoirs using CO2: A Look Ahead to the Future of Unconventional EOR, in: SPE Unconventional Resources Conference, Society of Petroleum Engineers, The Woodlands, Texas, USA, 2014. doi:10.2118/169022-MS.

[117] W. Yu, H. Lashgari, K. Sepehrnoori, Simulation Study of CO2 Huff-n-Puff Process in Bakken Tight Oil Reservoirs, in: SPE Western North American and Rocky Mountain Joint Meeting, Society of Petroleum Engineers, Denver, Colorado, USA, 2014. doi:10.2118/169575-MS.

[118] V. A. Fai-Yengo, H. Rahnema, M. Alfi, Impact of Light Component Stripping During CO2 Injection in Bakken Formation, Unconventional Resources Technology Conference (URTEC), Tulsa, OK, USA, 2014. doi:10.15530/urtec-2014-1922932.

APPENDIX A

APPARENT PERMEABILITY CALCULATION

This appendix includes the FORTRAN code (F90) to calculate the apparent permeability of the gas phase. Spacing and newlines are modified to fit the dissertation format.

```
!
      LOGICAL FUNCTION Apparent_permeability (MedNum, ElemNum,
  pressure, temperature, viscosity, density, GasC_mole_Gas,
  apparent_perm)
!
! ...... Modules to be used
!
         USE General_External_File_Units
!
         USE Basic_Parameters, N1 => ElemArraySize
         USE EOS_Default_Parameters
!
         USE General_External_File_Units
         USE General_Control_Parameters
!
         USE Grid_Geometry
!
         USE Element_Attributes
!
         USE Geologic_Media_Parameters
!
         USE Universal_Parameters
!
         USE Gas_Parameters
         USE Gas_Thermophysical_Properties
         USE Oil_Parameters
!
!*************************************************************
!*************************************************************
!*
```

```
!*    Compute the apparent permeability of the gas phase flow
!*
!*                        Version 1.0 - May, 2014
!*
!*************************************************************
!*************************************************************
!
      IMPLICIT NONE
!
! -------
! ... Integer variables
! -------
!
!
      INTEGER(KIND = 2), INTENT(IN)     :: MedNum
      INTEGER , INTENT(IN)              :: ElemNum
!
! -------
! ... Real variables
! -------
!
      REAL(KIND = 8), INTENT(IN)                    ::
  pressure,
      temperature, viscosity, density, GasC_mole_Gas
      REAL(KIND = 8), INTENT(OUT), DIMENSION (3)    ::
  apparent_perm                    ! in m^2
!
      REAL(KIND = 8)                                ::
  t_k, gasphase_MW, z_factor
      REAL(KIND = 8)                                ::
  lambda                        ! mean free path, m
      REAL(KIND = 8), DIMENSION (3)                 ::
  hydraulic_radius          ! hydraulic radius, m
      REAL(KIND = 8), DIMENSION (3)                 ::
  Kn                           ! Knudsen number
      REAL(KIND = 8), DIMENSION (3)                 ::
  alpha, fn

!
! -------
! ... Logical variables
! -------
```

```
!
      LOGICAL :: First_call = .TRUE.
!
! -------
! ... Saving variables
! -------
!
      SAVE First_call
!
!
!  =>=>=>=>=>=>=>=>=>=>=>=>=>=>=>=>=>=>   Apparent_permeability
!
!
      IF(First_call) THEN
!
         First_call = .FALSE.
         WRITE(VERS_Unit,6000)
!
      END IF
!
!
!
!>>>>>>>>>>>>>>>>>>>>>>>>>>>>>>>>>>>>>>>>>>>>>>>>>>>>>>>>>>>>>>>>>>>>>>>>>>>>>>
!>>>>>>>>>>>>>>>>>>>>>>>>>>>>>>>>>>>>>>>>>>>>>>>>>>>>>>>>>>>>>>>>>>>>>>>>>>>>>>
!>>>>>>>>>>>>>>>>>>>>>>>>>>>>>>>>>>>>>>>>>>>>>>>>>>>>>>>>>>>>>>>>>>>>>>>>>>>>>>
!>
!>          Computes the apparent permeability of the gas phase
!>
!>          'Effective correlation of apparent gas permeability'
!>                              (Civan_10_1)
!>      BY: Faruk Civan- Transp Porous Med (2010) 82:375-384
!>
!>  'A review of approaches for sescribing gas transfer through
!>   extremely tigh porous media'
!>                                (Civan_10_2)
!>      BY: Faruk Civan- Pourous media and its application in
!>
!>>>>>>>>>>>>>>>>>>>>>>>>>>>>>>>>>>>>>>>>>>>>>>>>>>>>>>>>>>>>>>>>>>>>>>>>>>>>>>
!>>>>>>>>>>>>>>>>>>>>>>>>>>>>>>>>>>>>>>>>>>>>>>>>>>>>>>>>>>>>>>>>>>>>>>>>>>>>>>
!>>>>>>>>>>>>>>>>>>>>>>>>>>>>>>>>>>>>>>>>>>>>>>>>>>>>>>>>>>>>>>>>>>>>>>>>>>>>>>
!
!
```

```
        Apparent_permeability   = .TRUE.
        t_k                     = temperature + 273.15d0
        gasphase_MW             =
gas%MoleculeMass * GasC_mole_Gas
        + oil%MoleculeMass * (1.0d0 -GasC_mole_Gas)
!
! ... Calculate mean free path
!       Use Civan_10_2, eq. 13
!
        CALL Peng_Robinson_EOS( pressure, t_k, GasC_mole_Gas,
z_factor)
        lambda = 16.0d0 * viscosity * z_factor / (5.0d0
* pressure)
        * SQRT(R_gas*t_k/(2.0d0 * pi * gasphase_MW))
!
! ... Calculate hydraulic radius using toruasity,
! permeability and porosity
!       Use Civan_10_1, eq. 20
!
        hydraulic_radius = 2.0d0 * SQRT(2.0d0 *
media(MedNum)%Tortu) *              &
 &      SQRT(ElemMedia(ElemNum,current)%perm
 / ElemMedia(ElemNum,current)%porosity)
!
! ... Knudsen number, Civan_10_1, eq. 4
!
        Kn = lambda / (hydraulic_radius+noise)
!
! ... Alpha, Civan_10_1, eq. 9-Loyalka and Hamoodi data
!
        alpha = 1.358d0/((0.178d0 / Kn**0.4348d0) +1.0d0)
!
! ... Apparent permeability, based on Civan_10_1, eq.3, and 18
!
        fn            = (1.0d0 + alpha * Kn) *
(1.0d0 + 4.0d0 * Kn / (1.0d0 + Kn))
        apparent_perm = ElemMedia(ElemNum,current)%perm * fn
!
!************************************************
!*
!*                    Unrealistic conditions flag
!*
```

```
!***********************************************
!
         IF (ANY(apparent_perm < 0.0d0) .OR.
 ANY(apparent_perm > 1.0d0) .OR.
         (apparent_perm(1) /= apparent_perm(1)) &
    &         .OR. (apparent_perm(2) /= apparent_perm(2)).OR.
    (apparent_perm(3) /= apparent_perm(3))) THEN
!
            WRITE (*,*) 'Apparent permeability is wrong numbers!'
            STOP
            Apparent_permeability = .FALSE.

         END IF
!
!
!*********************************************
!*
!*                        F  O  R  M  A  T  S
!*
!*********************************************
!
!
 6000 FORMAT(/,'Apparent_permeability',T50,'[v1.0   June
 2014]',/,
             ':::::     Transient permeability as a function
 of porosity changes')
!
!
!  =>=>=>=>=>=>=>=>=>=>=>=>=>=>=>=>=>=>=>=>=>=>=>=>=>=>   End of
Apparent_permeability
!
!
      RETURN
!
      END FUNCTION Apparent_permeability
!
!
%\end{singlespacing}
```

APPENDIX B

MULTI-COMPONENT OIL AND GAS DESORPTION CALCULATION

This appendix includes the FORTRAN code (F90) to calculate multi component oil and gas desorption. Spacing and newlines are modified to fit the dissertation format.

```
!
         LOGICAL FUNCTION Compute_Gas_Desorption(MedNum, pressure,
         gasC_mole_frac_Gas, gasC_desorption, oilC_desorption)
!
! ......... Modules to be used
!
            USE Gas_Parameters
!
            USE General_External_File_Units
!
            USE Geologic_Media_Parameters
!
            USE Universal_Parameters
!
            USE Gas_Parameters
            USE Oil_Parameters
!
!*****************************************************************
!*****************************************************************
!*
!*              Compute gas desorption standard volume
!*             assuming an isothermal Langmuir desorption
!* Gas desoprtion will happen to oilC and gasC in the gaseous phase
!*
!*      "Modeling gas production from shales and coal-beds"
!*               Waqas Ali-MS Thesis-Stanford U-2012
!*
!*****************************************************************
!*****************************************************************
!
```

```
!
        IMPLICIT NONE
!
! ----------
! ..... Double precision variables   ! <Bicheng == gas> 11
! ----------
!
        REAL(KIND = 8), INTENT(IN)     :: pressure
 ! Pressure in Pa
!
        REAL(KIND = 8), INTENT(IN)     :: gasC_mole_frac_Gas
 ! mole fraction of gasC in the gaseous phase
!
        REAL(KIND = 8), INTENT(OUT)    :: gasC_desorption,
        oilC_desorption     ! Gas desorption standard volume
 in unit mass of media, unit: std m^3/kg
!
        INTEGER(KIND = 2), INTENT(IN)  :: MedNum
 ! Medium NO. to pick up the desorption parameters
!
        REAL(KIND = 8)                 :: sum
!
! ----------
! ..... LOGICAL variables
! ----------
!
        LOGICAL :: First_call = .TRUE.
        LOGICAL :: unrealistic_conditions
!
! ----------
! ..... Saving variables
! ----------
!
        SAVE First_call
!
!
!  =>=>=>=>=>=>=>=>=>=>=>=>=>=>=>=>=>=>=>=>=>=>=>=>=>=>=>  Main body of
<Compute_Gas_Desorption>
!
!
        IF(First_call) THEN
           First_call = .FALSE.
```

```
            WRITE(UNIT = VERS_Unit, FMT = 6000)
         END IF
!
! -------------
! ...... Initialization
! -------------
!
         Compute_Gas_Desorption = .TRUE.
!
! -------------
! ... Gas desorption is considered to occur in the gaseous
phase-both  oilC and gasC (components) will be evolved
! -------------
!
         IF (media(MedNum)%LangmuirPressureO == 0.0D0 .OR.
         media(MedNum)%LangmuirPressureG == 0.0D0) THEN
             gasC_desorption = 0.0d0
             oilC_desorption = 0.0d0
         ELSE
             sum                 = pressure * (gasC_mole_frac_Gas
             / media(MedNum)%LangmuirPressureG + (1.0d0
             - gasC_mole_frac_Gas)
 / media(MedNum)%LangmuirPressureO)
!
! ... gasC desorption is calculated for the unit volume of rock
!
             gasC_desorption    = pressure * gasC_mole_frac_Gas
             / media(MedNum)%LangmuirPressureG
             * media(MedNum)%LangmuirVolumeG / (1.0d0 + sum)
             gasC_desorption    = gasC_desorption
             * media(MedNum)%DensG * CH4_density_std
 ! unit: kg / m^3
!
! ... for the oilC, the density at standar condition is
considered to be oilC MW / gasC MW * CH4_density@SC
!
             oilC_desorption    = pressure
 * (1.0d0 - gasC_mole_frac_Gas)
             / media(MedNum)%LangmuirPressureO
             * media(MedNum)%LangmuirVolumeO / (1.0d0 + sum)
             oilC_desorption    = oilC_desorption
 * media(MedNum)%DensG
```

```
            * CH4_density_std * oil%MoleculeMass
 /gas%MoleculeMass   ! unit: kg / m^3
!
! ... GasC or OilC adsorption is zero if any of the
Langmuir parameters are equal to zero
!
            IF (media(MedNum)%LangmuirVolumeG == 0.0D0 .OR.
            media(MedNum)%LangmuirPressureG == 0.0D0)
 gasC_desorption = 0.0d0
            IF (media(MedNum)%LangmuirVolumeO == 0.0D0 .OR.
            media(MedNum)%LangmuirPressureO == 0.0D0)
 oilC_desorption = 0.0d0
!
         END IF

!
! -------------
! ...... Check results
! -------------
!
         IF(ISNAN(gasC_desorption) .OR. ISNAN(oilC_desorption)
 .OR.
         gasC_desorption < 0D0 .OR. gasC_desorption > 1.0D9
 .OR.
          oilC_desorption < 0D0 .OR. oilC_desorption > 1.0D9)
  THEN
            Compute_Gas_Desorption = .FALSE.
            WRITE(*,FMT = 6100)
            STOP
         END IF
!
!*******************************************
!*
!*                       F  O  R  M  A  T  S
!*
!*******************************************
!
!
 6000 FORMAT(/,'Compute_Gas_Desorption',T50,'[v1.0,
 10 June 2012]',6X,/,
             ':::::   Calculate the gas desorption pressure
  dependent as isothermal Langmuir desorption')
```

```
!
 6100 FORMAT('The result of gas desorption is not a number,
 negative or impossible! Please correct the input and try again!')
!
!
!  =>=>=>=>=>=>=>=>=>=>=>=>=>=>=>=>=>=>=>=>=>=>=>=>=>  End of
<Compute_Gas_Desorption>
!
!
         RETURN
!
         END FUNCTION Compute_Gas_Desorption
!
!
```

APPENDIX C

EAGLE FORD MULTIPLE POROSITY MODEL

This appendix includes an example of the Nexus input files for the Eagle Ford triple-porosity history matching case. Spacing and newlines are modified to fit the dissertation format.

- The .fcs file includes:

```
RUN_UNITS ENGLISH
DEFAULT_UNITS ENGLISH
DATE_FORMAT MM/DD/YYYY

POROSITY_TYPES
       NAME          KEYWORD      LABEL    WELL_COMP
       MATRIX_LRG    MATRIX       L        N
       MATRIX_SML    MATRIXS      S        N
       FRACTURE      FRAC   F     Y


ENDPOROSITY_TYPES

GRID_FILES
 STRUCTURED_GRID nexus_data/TRPPORO_GW-grid.dat
 OPTIONS nexus_data/TRPPORO_GW-prop_options.dat

ROCK_FILES
 ROCK Method 1 nexus_data/TRPPORO_GW-rock_rock.dat
 RELPM Method 1 nexus_data/TRPPORO_GW-rock_relpm_1.dat
 RELPM Method 2 nexus_data/TRPPORO_GW-rock_relpm_2.dat
 RELPM Method 3 nexus_data/TRPPORO_GW-rock_relpm_3.dat

PVT_FILES
 PVT Method 1 nexus_data/TRPPORO_GW-pvt_pvt_1.dat
 PVT Method 2 nexus_data/TRPPORO_GW-pvt_pvt_2.dat
```

```
 PVT Method 3 nexus_data/TRPPORO_GW-pvt_pvt_3.dat
 WATER Method 1 nexus_data/TRPPORO_GW-pvt_water.dat
 SEPARATOR Method 1 nexus_data/TRPPORO_GW_pvt_separator.dat

INITIALIZATION_FILES
 EQUIL Method 1 nexus_data/TRPPORO_GW-init_equil_1.dat
 EQUIL Method 2 nexus_data/TRPPORO_GW-init_equil_2.dat
 EQUIL Method 3 nexus_data/TRPPORO_GW-init_equil_3.dat

RECURRENT_FILES
 RUNCONTROL nexus_data/TRPPORO_GW_runcontrol.dat
 WELLS Set 1 nexus_data/TRPPORO_GW_wells.dat
 SURFACE Network 1 nexus_data/TRPPORO_GW_surface.dat
```

- An example of the grid geometry file

```
!
!
!     Arrays written to map or VDB file
MAPOUT ALL
! ---------------------------
!     GRID DEFINITION
! ---------------------------
NX       NY        NZ
90      36        5

!INCLUDE LGRAdrs.dat
! Manual grid decomposition
!DECOMP
!ROOT 2 2 1

!ENDDEC

! ---------------------------
!     GRID DATA ARRAYS
! ---------------------------
ARRAYS

DX XVAR
```

```
90*50
DY YVAR
36*50
!5*10
DZ ZVAR
5*34
!5*50

LX MATRIX MATRIXS MULT
1 DX

LY MATRIX MATRIXS MULT
1 DY

LZ MATRIX MATRIXS MULT
1 DZ



LX MATRIXS FRAC MULT
0.7 DX

LY MATRIXS FRAC MULT
0.7 DY

LZ MATRIXS FRAC MULT
0.7 DZ



LX MATRIX FRAC MULT
0.7 DX

LY MATRIX FRAC MULT
0.7 DY

LZ MATRIX FRAC MULT
0.7 DZ



DEPTH DIP
```

```
10600 0 0

POROSITY MATRIX CON
0.03

POROSITY MATRIXS CON
0.01

POROSITY FRAC CON
0.000 ! Modified from the original of 0.0016
INCLUDE Quad_nfrac_phi.dat

POROSITY HFRAC CON
0.000 ! Modified from the original of 0.0016
INCLUDE Quad_hfrac_phi.dat


! 5 nD for larger pores
KX MATRIX CON
0.000007
KY MATRIX CON
0.000007
KZ MATRIX CON
0.000007

! 5 nD for smaller pores
KX MATRIXS CON
0.000003
KY MATRIXS CON
0.000003
KZ MATRIXS CON
0.000003

! Natural fracture
KX FRAC CON
0.000005
INCLUDE Quad_nfrac_perm.dat
KY FRAC CON
0.000005
INCLUDE Quad_nfrac_perm.dat
KZ FRAC CON
0.000005
```

```
INCLUDE Quad_nfrac_perm.dat


IEQUIL MATRIX CON
1
IRELPM MATRIX CON
1
IPVT MATRIX CON
1
IEQUIL MATRIXS CON
2
IRELPM MATRIXS CON
2
IPVT MATRIXS CON
2
IEQUIL FRAC CON
3
IRELPM FRAC CON
3
IPVT FRAC CON
3
!INCLUDE LGRProp.dat
```

- Rock properties file

```
!     Rock compressibility
CR 1.e-6 PREF 3004
```

- Relative permeability file

```
!     Water-oil table
WOTABLE
  SW     KRW    KROW  PCWO
0.25 0 1 0
0.2675 2.34E-10 0.793882491 0
0.285 3.00E-08 0.622431112 0
0.3025 5.13E-07 0.481265983 0
0.32 3.84E-06 0.366357377 0
```

```
0.3375 1.83E-05 0.27401585 0
0.355 6.56E-05 0.200882072 0
0.3725 0.000193018 0.14391634 0
0.39 0.00049152 0.100387728 0
0.4075 0.001121008 0.067862851 0
0.425 0.00234375 0.044194174 0
0.4425 0.004567306 0.027507829 0
0.46 0.00839808 0.016190862 0
0.4775 0.014706684 0.008877817 0
0.495 0.02470629 0.004436553 0
0.5125 0.040045166 0.001953125 0
0.53 0.06291456 0.000715542 0
0.5475 0.096173126 0.00019607 0
0.565 0.14348907 3.16E-05 0
0.5825 0.209501189 1.40E-06 0
0.6 0.3 0 0


!     Gas-oil table
GOTABLE
  SG     KRG    KROG PCGO
0 0 1 0
0.05 0 1 0
0.06 2.35E-12 0.870687226 0
0.07 3E-10 0.754770457 0
0.08 5.13E-09 0.651227778 0
0.09 3.84E-08 0.559085541 0
0.1 0.000000183 0.477417585 0
0.11 0.000000657 0.40534443 0
0.12 0.00000193 0.34203247 0
0.13 0.00000492 0.286693145 0
0.14 0.0000112 0.238582101 0
0.15 0.0000235 0.196998325 0
0.16 0.0000457 0.161283275 0
0.17 0.0000841 0.130819986 0
0.18 0.000147233 0.105032149 0
0.19 0.000247342 8.34E-02 0
0.2 0.000400905 6.54E-02 0
0.21 0.000629857 0.0505484 0
0.22 0.000962819 0.038479303 0
0.23 0.001436514 0.028780474 0
0.24 0.002097382 0.021099076 0
```

```
0.25 0.003003395 0.015115842 0
0.26 0.004226078 0.010543939 0
0.27 0.005852766 0.007127781 0
0.28 0.007989089 0.004641809 0
0.29 0.010761706 0.002889206 0
0.3 0.014321301 0.001700561 0
0.31 0.018845855 0.000932456 0
0.32 2.45E-02 0.000465981 0
0.33 3.17E-02 0.000205141 0
0.34 4.05E-02 0.0000752 0
0.35 5.13E-02 0.0000206 0
0.36 6.46E-02 0.00000332 0
0.37 8.06E-02 0.000000147 0
0.38 0.1 0 0

!     3 phases Kro calculation method
STONE2
!     End point scaling method
SCALING THREEPOINT
```

- PVT properties file

```
! Data from the validate WInprop-Eagle Ford fluid data
EOS NHC 7
    COMPONENTS C1-N2 C2-CO2 C3 FC4 FC5 HYP1 HYP2
TEMP 270
ENGLISH FAHR
EOSOPTIONS PR

PROPS
COMPONENT MOLWT OMEGAA OMEGAB
C1-N2 16.043 0.45723553 0.077796074
C2-CO2 30.07 0.45723553 0.077796074
C3 44.097 0.45723553 0.077796074
FC4 58.124 0.45723553 0.077796074
FC5 72.151 0.45723553 0.077796074
HYP1 168.39755 0.45723553 0.077796074
HYP2 548.48675 0.45723553 0.077796074
TC PC ZC ACENTR
```

```
-117.22 666.926 0.287500078 0.008
89.42 708.058 0.284686375 0.098
205.34 615.511 0.280303694 0.152
305.06 550.875 0.274055389 0.193
384.98 489.177 0.262684097 0.251
674.10266 297.0508529 0.273170986 0.52807882
1275.66608 96.59192823 0.158784905 1.2829352
BP VSHIFT PARACHOR
-258.61 -0.1538605 77
-127.57 -0.12401104 108
-43.69 -0.0863 150.3
31.19 -0.064312128 189.9
96.89 -0.034462672 231.5
421.82165 0.12778906 470.13707
1016.9607 0.26097116 1098.3692

ENDPROPS

BINA
COMPONENT C1-N2 C2-CO2 C3 FC4 FC5 HYP1
C2-CO2 2.63E-03
C3 8.34E-03 1.62E-03
FC4 1.44E-02 4.80E-03 8.46E-04
FC5 2.02E-02 8.38E-03 2.65E-03 5.02E-04
HYP1 5.92E-02 3.80E-02 2.44E-02 1.63E-02 1.12E-02
HYP2 1.28E-01 9.83E-02 7.69E-02 6.28E-02 5.27E-02 1.63E-02
ENDBINA
```

- Initialization file

```
! very important information about the pin and GOC-in GOC is below
the DINT, it takes the PSAT to do
! the initialization (PSAT is from flash not the provided PSAT).
so provide DINT below the GOC to use
! the PINT to initialize your model.


PINIT 8250  ! Initial reservoir pressure at the specified depth
```

```
(PSIA)
DINIT 10600  ! Datum depth (feet)
!WOC 10900  ! Depth of the water-oil contact (feet)
WOC 11500  ! Depth of the water-oil contact (feet)
PCWOC 0.  ! Water-oil contact capillary pressure at gas-water
contact (PSIA)

GOC 9400  ! Depth of the gas-oil contact
PCGOC 0  ! Gas-oil capillary pressure at gas-oil contact
PSAT 8105  ! Initial saturation pressure at given depth-Pressure at
GOC

! To overread the data, look at the -grid and -options files

!     VIP equilibrium initialization emulation
VIP_INIT 3
!     3 : Minimum and maximum cell depth

OILMF  ! Mole fraction in liquid hydrocarbon phase
! composition from the Eagle Ford-Ranch 74-PVT report
C1-N2 C2-CO2 C3 FC4 FC5 HYP1 HYP2
0.35959924 0.09865132 0.049834912 0.043537 0.053397528
0.33137694 0.063603064
MATCHVIPPRES  ! Uses vip method for phase compositions
```

- Run control file

```
START 09/16/2011

!     Timestepping method
METHOD IMPLICIT

!     Current optimized default for facilities
SOLVER FACILITIES EXTENDED
  GRIDSOLVER IMPLICIT_COUPLING NONE
  !GRIDSOLVER IMPLICIT_PRECON ILU 1
  !GRIDSOLVER IMPLICIT_PRECON GAUSS_SEIDEL
  GRIDSOLVER IMPLICIT_PRECON HALF_FAST
```

```
!             IMPES_COUPLING NONE

SOLVER ALL GLOBALTOL 0.00001

SOLVER DUAL_SOLVER OFF

GRIDSOLVER CPR_PRESSURE_EQUATION IMPES

!     Use vip units for output to vdb
VIPUNITS

!     Arrays written to map or VDB file
MAPOUT
P
SAT GAS WATER
PSAT
GOR
ENDMAPOUT
! Use ARRAYOUT to output the data into an ASCII file
!ARRAYOUT
!ENDARRAYOUT


!     Frequency at which output is written
OUTPUT WELLPLOT MONTHLY !TIMES
       FIELDPLOT MONTHLY !TIMES
   REGIONPLOT MONTHLY !TIMES
       MAPS MONTHLY  ! this will specify
   the frequency of output map file-this is the
   ditribution map-vdb file
!    ARRAYS TIMES ! This will specify the
frequency of write on the .out file
ENDOUTPUT


OUTSTART
!CONNECT
ENDOUTSTART

DT MIN 0.000001
DT AUTO 0.10  MAX 1000
TIME 0.05
```

```
TIME 0.10
TIME 0.5
TIME 6/1/2014

STOP
```

- Well location file

```
WELLSPEC P1
IW JW L PORTYPE KH RADW SKIN WI
11 19 3 FRAC NA 0.4 0 1
12 19 3 FRAC NA 0.4 0 1
13 19 3 FRAC NA 0.4 0 1
14 19 3 FRAC NA 0.4 0 1
15 19 3 FRAC NA 0.4 0 1
16 19 3 FRAC NA 0.4 0 1
17 19 3 FRAC NA 0.4 0 1
18 19 3 FRAC NA 0.4 0 1
19 19 3 FRAC NA 0.4 0 1
20 19 3 FRAC NA 0.4 0 1
21 19 3 FRAC NA 0.4 0 1
22 19 3 FRAC NA 0.4 0 1
23 19 3 FRAC NA 0.4 0 1
24 19 3 FRAC NA 0.4 0 1
25 19 3 FRAC NA 0.4 0 1
26 19 3 FRAC NA 0.4 0 1
27 19 3 FRAC NA 0.4 0 1
28 19 3 FRAC NA 0.4 0 1
29 19 3 FRAC NA 0.4 0 1
30 19 3 FRAC NA 0.4 0 1
31 19 3 FRAC NA 0.4 0 1
32 19 3 FRAC NA 0.4 0 1
33 19 3 FRAC NA 0.4 0 1
34 19 3 FRAC NA 0.4 0 1
35 19 3 FRAC NA 0.4 0 1
36 19 3 FRAC NA 0.4 0 1
37 19 3 FRAC NA 0.4 0 1
38 19 3 FRAC NA 0.4 0 1
```

```
39 19 3 FRAC NA 0.4 0 1
40 19 3 FRAC NA 0.4 0 1
41 19 3 FRAC NA 0.4 0 1
42 19 3 FRAC NA 0.4 0 1
43 19 3 FRAC NA 0.4 0 1
44 19 3 FRAC NA 0.4 0 1
45 19 3 FRAC NA 0.4 0 1
46 19 3 FRAC NA 0.4 0 1
47 19 3 FRAC NA 0.4 0 1
48 19 3 FRAC NA 0.4 0 1
49 19 3 FRAC NA 0.4 0 1
50 19 3 FRAC NA 0.4 0 1
51 19 3 FRAC NA 0.4 0 1
52 19 3 FRAC NA 0.4 0 1
53 19 3 FRAC NA 0.4 0 1
54 19 3 FRAC NA 0.4 0 1
55 19 3 FRAC NA 0.4 0 1
56 19 3 FRAC NA 0.4 0 1
57 19 3 FRAC NA 0.4 0 1
58 19 3 FRAC NA 0.4 0 1
59 19 3 FRAC NA 0.4 0 1
60 19 3 FRAC NA 0.4 0 1
61 19 3 FRAC NA 0.4 0 1
62 19 3 FRAC NA 0.4 0 1
63 19 3 FRAC NA 0.4 0 1
64 19 3 FRAC NA 0.4 0 1
65 19 3 FRAC NA 0.4 0 1
66 19 3 FRAC NA 0.4 0 1
67 19 3 FRAC NA 0.4 0 1
```

- Well constraints file

```
!     Fluid model for network
EOS NHC 7
    COMPONENTS C1-N2 C2-CO2 C3 FC4 FC5 HYP1 HYP2

!     Connection defaults
CONDEFAULTS
```

```
 CONTYPE   TYPE  METHOD
 ! wellbore is data for the connections and nodes in
 the perforated section of the wellbore
WELLBORE LUMPED CELLAVG
ENDCONDEFAULTS

!     Shift bottom-hole node if connection length is
less than depth change
ALLOW_BHMOVE

!     Control of constraints on well connections
WELLCONTROL WELLHEAD

!     Hydraulics options
HYDRAULICS FLOW_UNSTABLE

!     Constraints will be added
DONTCLEAR

!     Network default temperature
NETTEMP 180.

!     Gas injector mobility computation method
!     Water injector mobility computation method
INJMOB ENDPT

!     Wells definition
! This is from the bottom hole to first node inside
the well
WELLS
NAME   STREAM NUMBER DATUM CROSSFLOW CROSS_SHUT
  P1 PRODUCER      1  10600        ON        OFF
ENDWELLS

! this is from bottom hole to the surface
! this is the actual well
! deactivated for BHP constraints
WELLHEAD
WELL  NAME IPVT DIAM DEPTH ROUGHNESS
LENGTH
P1 P1_WELL 1 3 0.0 0.0006
11232.0  ! this MD is achieved from the well data
```

```
ENDWELLHEAD


! this files provides the well data and constraints
INCLUDE Well_constraints_corrected1.dat
!INCLUDE Well_constraints_simple_1.dat
!CONSTRAINTS
!P1 BHP 500 QOSMIN 1.0e-05 QOSMAX 2000
!ENDCONSTRAINTS


!TIME 106
!TIME 1230
!CONSTRAINTS
!P1 QOSMAX 0
!ENDCONSTRAINTS
```